

**DEVELOPMENT OF FIELD DEPLOYABLE FIBER BRAGG GRATING  
INTERROGATOR**

**ABDUL HALIM POH YUEN WU**

**DISSERTATION SUBMITTED IN FULFILMENT OF THE  
REQUIREMENTS FOR THE DEGREE OF MASTER OF  
ENGINEERING SCIENCE**

**FACULTY OF ENGINEERING  
UNIVERSITY OF MALAYA  
KUALA LUMPUR**

**2013**

**UNIVERSITI MALAYA**

**ORIGINAL LITERARY WORK DECLARATION**

Name of Candidate: **ABDUL HALIM POH YUEN WU** (I.C/Passport No:

Registration/Matric No: **KGA110030**

Name of Degree: **MASTER OF ENGINEERING SCIENCE**

Title of Project Paper/Research Report/Dissertation/Thesis ("this Work"):

**DEVELOPMENT OF FIELD DEPLOYABLE FIBER BRAGG GRATING INTERROGATOR**

Field of Study: **OPTICAL SENSORS**

I do solemnly and sincerely declare that:

- (1) I am the sole author/writer of this Work;
- (2) This Work is original;
- (3) Any use of any work in which copyright exists was done by way of fair dealing and for permitted purposes and any excerpt or extract from, or reference to or reproduction of any copyright work has been disclosed expressly and sufficiently and the title of the Work and its authorship have been acknowledged in this Work;
- (4) I do not have any actual knowledge nor do I ought reasonably to know that the making of this work constitutes an infringement of any copyright work;
- (5) I hereby assign all and every rights in the copyright to this Work to the University of Malaya ("UM"), who henceforth shall be owner of the copyright in this Work and that any reproduction or use in any form or by any means whatsoever is prohibited without the written consent of UM having been first had and obtained;
- (6) I am fully aware that if in the course of making this Work I have infringed any copyright whether intentionally or otherwise, I may be subject to legal action or any other action as may be determined by UM.

Candidate's Signature

Date

Subscribed and solemnly declared before,

Witness's Signature

Date

Name:

Designation:

## ABSTRACT

This study aims to address the main problems of analyzing fiber Bragg grating (FBG) sensors in field, which consists of two main issues. First is the usage of optical spectrum analyzers (OSAs) and broadband light sources. Both are bulky instruments, and especially the OSA being heavy and costly (ranges between RM100-200k for the OSA and RM20k for the light source). These equipments exhibit a very large wavelength range (1.1  $\mu\text{m}$  for the OSA, 35nm for the light source), which is unnecessary for the otherwise much less feature-demanding FBG. Second, the applications considered for the development of this optical sensor interrogation prototype is for applications which demands data to be logged from every few hours to days. Therefore, a study is conducted to design and construct a fully portable, low-cost and low-powered interrogator which is specifically designed to read FBGs within the C-band (1530-1565nm). This resulted in the construction of an Erbium-doped fiber amplifier (EDFA) ring laser, but the actual strength of this work lies within the integration with the electronic circuitry, which makes it portable and readily deployable. This work resulted in four milestones. The first is the successful construction of an optimized EDFA ring laser, the robust and low-power driving circuitry design and construction of the 980nm laser pump, the actuation and digitization of a tunable bandpass Filter (TBF) to render the laser's tunability tangible in the electronics realm, and finally the success in interrogating an FBG itself, which finalizes the work. A spectral profile similar to the one obtained via an OSA can be reverse-mapped using this interrogation scheme. The central wavelength of the reflected signal can be obtained via this method with minimum error of  $\pm 0.09\text{nm}$ .

## ABSTRAK

Penyelidikan ini bertujuan untuk membincangkan isu-isu yang dihadapi dalam memperoleh bacaan dari *Fiber Bragg Grating (FBG)* dalam penggunaan di medan ujikaji di luar makmal, dimana terdapat dua isu utama yang dihadapi, iaitu penggunaan alat *Optical Spectrum Analyzer (OSA)* atau Penganalisa Spektrum Optik, dan sumber cahaya *Amplified Spontaneous Emission (ASE)* atau Pancaran Amplifikasi Spontan. Kedua-dua peralatan ini sukar digunakan di kawasan yang terbuka, berat dan kosnya amat tinggi. Walaupun kedua-dua alat ini membolehkan penyelidik untuk membuat bacaan spektrum optik pada semua skala, FBG tidak memerlukan skala yang begitu luas untuk dianalisa, memandangkan julat spektrumnya hanya 2 hingga 3 nm sahaja, jika dibandingkan dengan OSA dan ASE yang beroperasi dalam julat yang jauh lebih besar.

Oleh itu, penyelidikan ini dijalankan untuk menyimpulkan satu rangka penganalisa FBG yang boleh dibawa dimana-mana sahaja, dengan julat pembacaan di sekitar julat C-band (1530-1565nm). Ada dua aspek yang perlu dipertimbangkan, yakni aspek optikal, dimana kita memerlukan komponen optik yang bergentian, dan litar elektronik yang melengkapkan sistem tersebut, menjadikannya mudahalih, dan boleh digunakan secara langsung.

Ada empat pencapaian yang signifikan yang telah diraih, yakni pertama, litar lingkaran laser optik dengan gentian *Erbium Doped Fiber Amplifier, (EDFA)* berjaya dibina, rangka litar untuk memacu pam laser 980nm telah berjaya dibina, pemutar bijak *Tunable Bandpass Filter* telah berjaya dibina, dan yang terakhir, pengukuran panjang gelombang FBG telah berjaya dijalankan menggunakan litar optik/elektronik ini, dengan kejituan  $\pm 0.09\text{nm}$ .

## ACKNOWLEDGEMENTS

All praise is only for Allah SWT, for he is the Creator of true knowledge. Peace and blessings be upon the Chosen One, who showed us the way towards the Truth, the best of examples, the last prophet for humankind, Muhammad SAW.

A million thanks to my supervisors Prof. Dr. Faisal Rafiq Mahamd Adikan and Prof. Dr. Mahmoud Moghavvemi, who took me under their wing. I have attained a much more fulfilling academic life in one year being a research student under them compared to any length of time spent in any institution all these years. The next key person in this work is Dr Hafiz b. Abu Bakar (UPM), within his short duration in our lab, guided me through fiber lasers (pun intended), which provided the breakthrough that I needed in my work. Completing the three giants of whom their shoulders I have stood upon would be Reza Sandoghchi (currently in ORC, Univ. of Southampton) the leading theoretician and experimentalist in the lab, who helped me countless times in my project.

I'd like to thank Rosdi (doing PhD in Bath) especially for his aid in fundamental handling of optical fibers, Desmond Chow for the reminder of the conference, our assistant admin, Ms Fathin who handled the oft-frustrating purchases, Dr Nizam Tamchek of UPM for helping me familiarize with the lab, Yeo Kwok Shien, who helped out occasionally, and programming whiz Imran (PhD, Cambridge). And to the rest of Photonics Research Group members- Fatimah, Peyman, Din Chai, Dr Ghafur, and Sarahah. You guys are awesome!

And putting this at the final paragraph does not undermine the appreciation I have to my family, -for Papa, Mummy, Kakak, Kakngah, Bancik, Kacik, Mintat and my beloved wife, Rafidah- pervades within whatever and whoever I am. To whomsoever reading this, you are reading a family's work.

## TABLE OF CONTENTS

<b>ABSTRACT</b>	<b>ii</b>
<b>ABSTRAK</b>	<b>iii</b>
<b>ACKNOWLEDGMENTS</b>	<b>iv</b>
<b>TABLE OF CONTENTS</b>	<b>v</b>
<b>LIST OF FIGURES</b>	<b>vii</b>
<b>LIST OF TABLES</b>	<b>x</b>
<b>LIST OF ABBREVIATIONS</b>	<b>xi</b>
<b>EQUATIONS</b>	<b>xii</b>
<b>1. Introduction</b>	<b>1</b>
1.1 Objectives	4
1.2 Scope of Dissertation	5
1.3 Outlines of this Study	5
<b>2. FIBER-BASED SENSORS AND DETECTION SCHEMES</b>	<b>7</b>
2.2 Overview of Fiber-based Sensors	8
2.3 Fiber Bragg Gratings	9
2.4 FBGs as sensors	13
2.5 Interrogation techniques of FBGs	15
2.5.1 Wavelength-Amplitude Conversion	15
2.5.2 Wavelength-Position Conversion	16
2.5.3 FBG Matching	17
2.5.4 Tunable Filters	18
2.5.5 Interferometers	19
2.5.6 Spectrometry	20
2.5.7 Tunable Lasers	21
2.6 Chapter Summary	23
<b>3 INTERROGATION OF FIBER BRAGG GRATINGS VIA TUNABLE RING LASERS</b>	<b>24</b>
3.1 Introduction	24
3.2 Tunable Lasers	24
3.2.1 Role of Tunable Laser in FBG Interrogation	25
3.2.2 Utilized Tunable Laser Design	30
3.3 Control of a 980 nm pump laser	33
3.3.1 Justifications for opting a 980nm pump laser	33
3.3.2 980nm Pump Laser Driver	35
3.4 Controlling a Tunable Bandpass Filter (TBF)	37
3.4.1 Electromechanical Aspect	37
3.4.2 Wavelength-Voltage Relation of the TBF Mount	38
3.5 Current-Voltage Conversion for Photodiode's Response Detection	39
3.6 Conclusion of the Tunable Ring Laser Interrogation of FBGs	41
3.7 Chapter Summary	42

<b>4</b>	<b>CONSTRUCTION AND ANALYSIS OF TUNABLE RING LASER FBG INTERROGATOR</b>	<b>44</b>
4.1	Tunable Ring Laser Setup	44
4.1.1	Ring Laser EDFA optical circuit construction	44
4.2	Control Electronics	47
4.2.1	Pump Laser Driver	47
4.2.2	980nm pump laser control driver construction	49
4.3	Spectral Characteristics of the Laser	52
4.3.1	Tuning Range	52
4.3.2	Laser Wavelength Accuracy and Stability	53
4.4	TBF Actuator Mount Construction	56
4.4.1	Assembly of the TBF Actuator	57
4.4.2	Modeling of the TBF Mount	61
4.5	Test Interrogation of FBGs	65
4.5.1	Null Test	67
4.5.2	Testing FBGs	69
4.5.2.1	FBG1 Tests	71
4.5.2.1	FBG2 Test	73
4.5.2.1	FBG3 Test	75
4.6	Chapter Summary	76
<b>5</b>	<b>CONCLUSIONS</b>	<b>77</b>
5.1	Laser Driver	77
5.2	Tunable laser profile	78
5.3	TBF Mounting Scheme	79
5.4	FBG Interrogation	79
5.5	Chapter Summary and Future Work Suggestion	82
	<b>REFERENCES</b>	<b>83</b>
	<b>PUBLICATIONS</b>	<b>90</b>
	<b>APPENDICES</b>	<b>91</b>
A:	An FBG's reflection response via EXFO's IQ-2600 Tunable Laser Source, and a photodiode	91
B:	Appendix B: TBF's positioning sensor output versus the central wavelength of the tunable laser formed, monitored using OSA	92
C:	Source Code	93
D:	Current advancements in project	97

## LIST OF FIGURES

### Chapter 1: Introduction

1.1	Applications of FBGs	2
1.2	A field test of an FBG embedded in a beam for a bridge	3

### Chapter 2: Fiber-Based Sensors and Detection Schemes

2.1	Schematic Diagram of a Basic Setup to Monitor an FBG	10
2.2	Figure 2.2 (a): A broadband source input for the FBG; (b) transmission spectrum of the FBG, showing the filtered region with $\lambda_B$ as the central wavelength.	10
2.3	FBG fabrication techniques: (a) free-space two-beam holographic interference and (b) diffractive phase masking technique (L. Zhang et al., 2008)	12
2.4	Schematic configuration of the FBG fabrication system with two phase masks. (Gao, Chen, Xiong, Liu, & Pu, 2012)	12
2.5	Wavelength shift response of the FBG towards a) Strain, and b) temperature (L. Zhang et al., 2008).	14
2.6	(a) Edge filter interrogation setup (b) WDM setup for coupling fiber (L. Zhang et al., 2008).	16
2.7	Wavelength positioning using bulk gratings (Zhang et al. 2008).	16
2.8	Matched FBG interrogation setup (L. Zhang et al., 2008)	17
2.9	A tunable filter interrogation setup (L. Zhang et al., 2008)	18
2.10	Interferometric interrogation (L. Zhang et al., 2008)	19
2.11	Spectrometer setup (L. Zhang et al., 2008)	21
2.12	Tunable Laser FBG Interrogation	21

### Chapter 3: Interrogation of Fiber Bragg Gratings via Tunable Ring Lasers

3.1	Schematic diagram of a basic setup to monitor an FBG	25
3.2	Spectral profile of a) a single laser. b) laser tuned along a defined bandwidth with periodic positions.	25
3.3	Setup to observe the role of a TLS in FBG interrogation	26
3.4	Sweep of the TLS along an FBG's spectrum, on the left is the spectral profile of the laser and the FBG; the left shows the spectrum via an OSA.	27
3.5	A plot of the peak power of each section versus the laser's central wavelength	28
3.6	FBG interrogation via TLS Setup	29
3.7	Figure 3.7: Output profile of an FBG interrogation (refer setup in Fig. 3.4)	30
3.8	EDFA tunable ring laser setup	31
3.9	Spectral profile of several stages in ring lasing	32

3.10	A 980 nm pump laser module from Agere, with an enlarged view on the Butterfly casing, with an FC-APC connector b) Pinout diagram (as stated in datasheet)	35
3.11	Control Circuit for SL980S31C 980 nm Pump Laser	36
3.12	A tunable bandpass filter (TBF) from Alnair Photonics; inset is for reference with the whole design	37
3.13	(a) A TBF mount design, (b) Connections made for setup	38
3.14	Photodiode response circuit	40
3.15	FBG interrogator with tunable EDFA ring laser setup	41
3.16	$V_{\text{photodiode}}$ versus $V_{\text{laser}}$	42

#### **Chapter 4: Construction and Analysis of Tunable Ring Laser FBG Interrogator**

4.1	Erbium-doped fiber amplifier (EDFA) ring laser setup	44
4.2	Flow of construction process of the EDFA ring laser circuitry	45
4.3	Testing Laser's Output	47
4.4	a) Pump laser testing using a variable DC supply and b) pinouts of the pump laser for testing	48
4.5	Control Circuit for SL980S31C 980 nm pump laser	49
4.6	980nm pump laser control circuit construction	50
4.7	Typical laser formation at 1565.15nm	52
4.8	Spectral output from the initial formation until the bandwidth limit of the laser.	53
4.9	Initial laser formation at 1517.688nm	54
4.10	Wavelength stability along the spectrum (1518-1589nm)	55
4.11	Power stability along the spectrum (1518-1589nm)	56
4.12	a) A manually tunable bandpass filter b) A TBF mount design	57
4.13	Tunable bandpass filter (TBF) digitization mount for ring laser tunability	59
4.14	Setup to model the TBF mount	61
4.15	Laser's central wavelength, $\lambda_{\text{TBF}}$ vs $V_{\text{TBF}}:V_{\text{ref}}$ plot	62
4.16	Laser's central wavelength, $\lambda_{\text{TBF}}$ vs $V_{\text{TBF}}:V_{\text{ref}}$ curve-fitting plot	63
4.17	Test interrogation setup	65
4.18	FBG interrogation setup scene	66
4.19	A typical null test.	67
4.20	Pie chart shows the frequency of the appearance a base voltage makes.	67
4.21	Current–optical power curve. (Photonics n/a)	68
4.22	Testing FBGs for two different conditions; (a) and (b) is FBG1, (c) and (d) is FBG2, (e) and (f) is FBG3	70
4.23	FBG1 reflection spectrum via OSA	71
4.24	FBG1 interrogation spectrum in terms of Volts (V)	72
4.25	FBG2 reflection spectrum via OSA	73
4.26	FBG2 interrogation spectrum in terms of Volts (V)	74
4.27	FBG3 reflection spectrum via OSA	75

4.28	FBG3 interrogation spectrum in terms of Volts (V)	75
------	---	----

### **Chapter 5: Conclusions**

5.1	Laser driver symbol/diagram	77
5.2	(a) TBF mount diagram, (b) constructed mount and (c) mathematical modeling of the mount	79

### **Appendix**

A.1	Central wavelength vs photodiode output voltage	91
B.1	Vsensor vs $\lambda$ (nm)	92
D.1	Complete overview of the FBG interrogator circuitry	97
D.2	An EDFL with an external cavity setup	98
D.3	Figure D3 (a) A compiled optical circuitry for the EDFL without the tuning filter; (b) FBG mounted on stacked piezo actuators; (c) laser formation via the external cavity of the EDFL; (d) the whole setup for the current research	99

## LIST OF TABLES

### **Chapter 4: Construction and Analysis of Tunable Ring Laser FBG Interrogator**

4.1	Error Calculation of the wavelength between the TBF actuation model and the laser's central wavelength read from the OSA	64
-----	--	----

### **Chapter 5: Conclusions**

5.1	Comparison of the spectral profile versus the interrogation profile	80
5.2	Central wavelength of FBG's reflection spectrum analysis	81
5.3	Comparison of wavelength shift between OSA and proposed system.	81
5.4	Comparison of features of FBG reading equipments	82

### **Appendix**

A.1	Central wavelength vs photodiode output voltage	91
B.1	V <sub>sensor</sub> vs $\lambda$ (nm)	92

## LIST OF ABBREVIATIONS

ABS	Acrylonitrile butadiene styrene
ASE	Amplified Spontaneous Emission
CAD	Computer-Aided Design
CCD	Charge-Coupled Device
DC	Direct Current
DMM	Digital Multimeter
EDF	Erbium-Doped Fiber
EDFA	Erbium-Doped Fiber Amplifier
EMI	Electromagnetic Interference
EN	Enable
FBG	Fiber Bragg Grating
FBGA	Fiber Bragg Grating Analyzer
FC/APC	Fiber Connector/ Angled Physical Contact
GND	Ground
LPFG	Long-Period Fiber Gratings
OSA	Optical Spectral Analyzer
REC	Reconstruction-Equivalent-Chirp
SHM	Structural Health Monitoring
SMF	Single-Mode Fiber
SPR	Surface Plasmon Resonance
TBF	Tunable Bandpass Filter
TLS	Tunable Laser Source
UMPRG	University of Malaya's Photonics Research Group
UV	Ultra-Violet
WDM	Wavelength Division Multiplexing
WSC	Wavelength Selection Coupler

## EQUATIONS

Eq. 2.1  $\lambda_B = 2n_{eff}A$

Eq. 2.2  $n(z) = n_{co} + \delta n [1 + \cos(2\pi z/A)]$

Eq. 2.3  $\frac{\Delta\lambda_B}{\lambda_B} = P_e \mathcal{E} + [P_e(\alpha_s - \alpha_f) + \zeta] \Delta T$

Eq. 3.1  $V_{out} = V_2 = \frac{R_{1,2}}{R_{pot}} x V_{ref}$

Eq. 3.2  $\lambda(V_{out}) = mV_{out} + \lambda_y$

Eq. 4.1  $V_{out} = V_2 = \frac{R_{1,2}}{R_{pot}} x V_{ref}, [0.1V_{ref} \leq V_{out} \leq 0.9V_{ref}]$

Eq. 4.2  $f(x) = \frac{a}{1 + e^{-\left(\frac{x-x_0}{b}\right)}}$

Eq. 4.3  $\lambda_{laser} = \frac{1646.5526}{1 + e^{-\left(\frac{V_{out} + 4.7596}{\frac{V_{ref}}{1.8999}}\right)}} \text{ nm}$

Eq. 4.4  $\lambda_{laser} = \frac{1646.5526}{1 + e^{-\left(0.5263 \frac{V_{out}}{V_{ref}} + 2.505\right)}} \text{ nm}$

# CHAPTER 1

## INTRODUCTION

There are various types of electronic sensors used in the industry which have direct parametric correlation with the research our group is dealing with. They are employed for specific applications such as in biomedical studies, structural health monitoring (SHM), pollution detection, and so on. Parameters such as strain, stress and vibration are essential for SHM. Various types of sensors are employed in concrete structures such as in bridges (Ye, Ni, Wong, & Ko, 2012) where various parameters are monitored. Oil pipelines are monitored for leakage using acoustic sensors (Xu, Zhang, & Liang, 2012), and so on.

There are classic problems which arise in all these applications, where most of the sensors used are susceptible to electromagnetic interference (EMI). This gives rise to the use of fiber-based sensors. A classic example is transformer oils, where its fluidic property degrades after some time. They are continually monitored by extracting samples, and running on a battery of tests in labs. In-situ chemical sensors cannot be employed for continual monitoring, but rather using optical fiber sensors (Ma, Li, Luo, Mu, & Wang, 2012). In this study, we focus mainly on fiber Bragg grating (FBG) sensors.

There are various fiber-based sensors which have caught our attention for its features, being immune towards EMI, resistance towards corrosion, capable of being adapted into other transducers, sensitive towards minuscule amounts of mechanical stress, and so on. There are various applications currently investigated by our own research group, as shown in Fig. 1.1.



Figure 1.1: Applications of FBGs

FBGs embedded in bridges for SHM was performed by our research group for an actual field test in Panglima Awang Bridge, Melaka, as shown in Fig. 1.1. Also, employing FBGs for leakage detection of submerged oil pipelines has a large potential, as investigated previously (Spirin, Shlyagin, Miridonov, Jiménez, & Gutiérrez, 1999). Other applications include corrosion sensing (Sun, Sun, Ren, & Zhang, 2012) and smart prosthetics, as shown in Fig. 1.1, all performed in within our research group as well.

An actual field test as mentioned before is as shown in Fig. 1.2, depicting the level of involvement and shortcomings we experience:

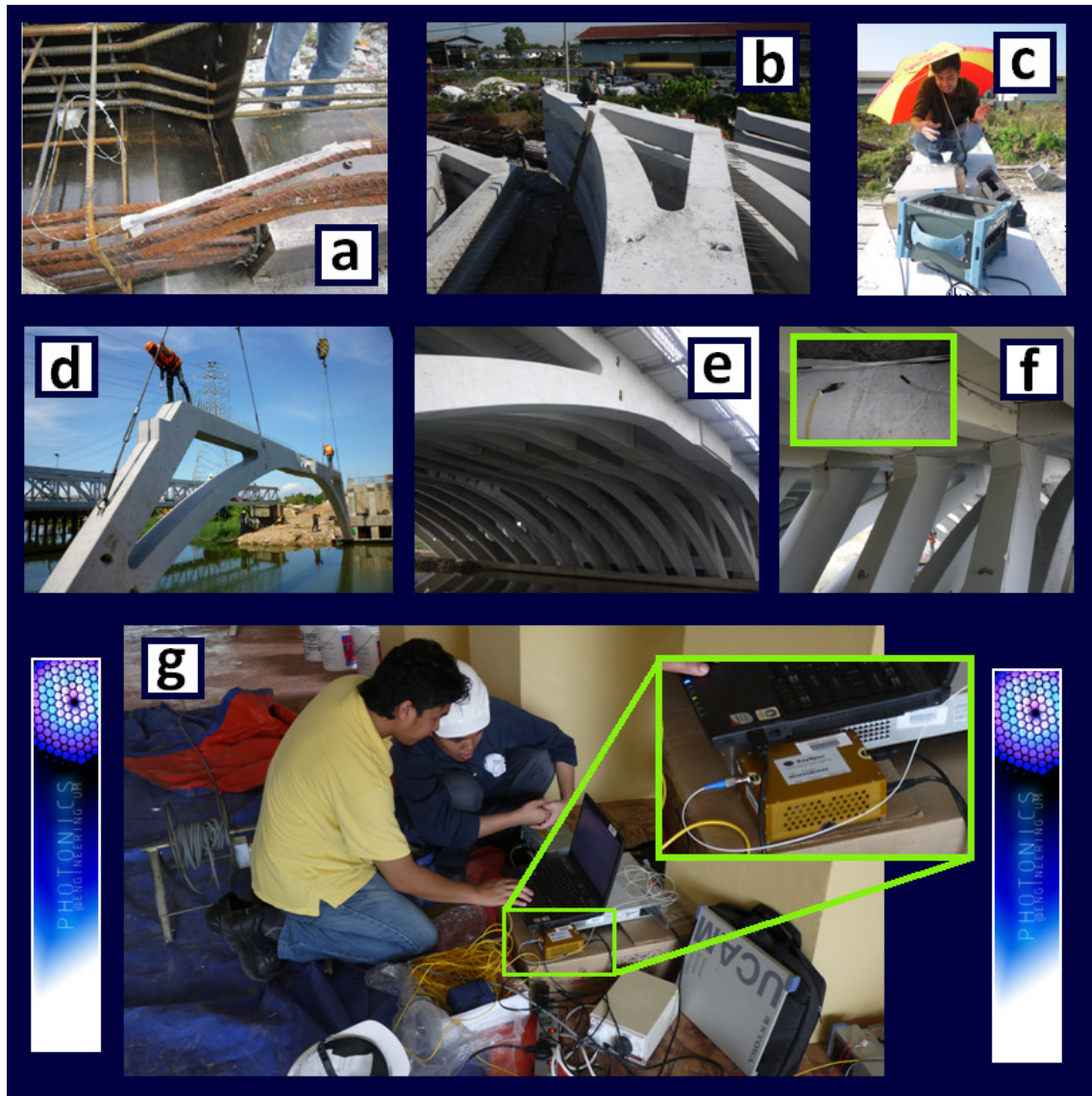


Figure 1.2: A field test of an FBG embedded in a beam for a bridge

Fig. 1.2 shows our presence during the construction of Panglima Awang Bridge, Melaka. Fig. 1.2a shows an FBG sensor was planted on the steel rebar of one of the bridge sections, using an epoxy cure. Fig. 1.2b shows the concrete beams of the bridge in Klang before they were transported to the site. Fig. 1.2c shows our first test of the FBG embedded in the

concrete beam using an optical spectral analyzer (OSA) and a broadband light source. One can see the difficulty experienced at such a condition to read the FBG. In Fig. 1.2d, the bridge was assembled using cranes, followed by the completion of laying out all the concrete beams in Fig. 1.2e. In Fig. 1.2f, we can observe the extension (yellow line) which reaches to the FBG so that it can be monitored from the side of the bridge, with the inset for a close-up view. Finally, Fig. 1.2g shows us performing a real-time FBG monitoring using Bayspec's FBG analyzer (FBGA, priced at RM20k, shown in the enlarged view). Although it is much smaller than a standard OSA, it still requires a broadband light source.

This project unveils a main problem to be addressed in our work; the need to have an FBG scanner which does not require an OSA and a broadband light source. Also, it needs to be battery-powered and much lower in cost compared to the equipments used previously.

## **1.1 Objectives**

Following the case presented in the previous section, the objectives are formed as follows:

- To develop an FBG interrogation system with portable and battery-operable features. This is done by selecting a suitable interrogation scheme, and studying its details.
- To design, construct and characterize the interrogation setup. The system should be within the budget of less than RM10k. Optical and electronics circuits design will be integrated with mechanical aspects of the system.
- To test the interrogator by scanning a few FBGs, and compare the readings with the one obtained via an OSA. The errors will be defined within the spectral domain as in wavelength and power of the FBG profile.

## **1.2 Scope of Dissertation**

In this study, we will be interrogating FBGs with reflection spectrum in the region of 1550nm. The interrogation will be in the form of computing the fundamental parameters i.e. the central wavelength of the reflection spectrum. Although one of the field tests highlighted in this work was directed towards the bridge project, it will not be our main objective to limit the interrogation for the project *per se*, but it will cover all types of application which does not demand a real time monitoring.

Therefore, a basic interrogation will be performed on unused or test FBGs, only to demonstrate the workability of the interrogation setup used.

## **1.3 Outlines of this Thesis**

Chapter 1 reveals our research philosophy, while presenting a real engineering problem which will be addressed by this work. A realistic approach is carried out, resonated by our involvement in real-life situations which may improve through our technical expertise.

Chapter 2 deals with the intricacies of fiber-based sensors, especially on FBGs, its fabrication methods and its interrogation schemes. A few popular methods will be outlined, and related recent literature will be elaborated while weighing between the techniques for balance in the chosen scheme. Ultimately, tunable lasers will be discussed, while presenting previous works pertaining to it.

Chapter 3 outlines the role of tunable lasers in FBG interrogation, the theoretical aspects revolving the setup, and the advantages of such a setup. Then, the details of the most significant components, namely the 980nm pump laser and the tunable bandpass filter (TBF) will be uncovered regarding the setup, mounting and so on.

Chapter 4 finalizes the objectives of our research by presenting the steps taken to construct each part of the interrogation setup. The spectral characteristics of the interrogation will be used as a comparison with the interrogation carried out by our own assemblage.

Chapter 5 summarizes the results we obtained, where a simplistic perspective can be concluded by our research. This includes the 980nm laser's technical issues, the spectral features of the laser, the TBF's mounting, and finally testing the interrogator on test FBGs. This marks the end line of our research.

## CHAPTER 2

### FIBER-BASED SENSORS AND DETECTION SCHEMES

In this chapter, we will give an overview on fiber-based sensors, followed by FBGs, and how it works as a sensor. This is followed by covering a few methods on FBG interrogation as performed in previous investigations, and finally settling down on the method of choice.

#### 2.1 Introduction

Fiber based sensors, as discussed previously, have great potential in many applications while retaining superiority over non-fiber based ones in some fields of sensing technologies. Currently, a few applications are being investigated, distributed among fellow co-researchers.

However, the applications may vary greatly; therefore the comparison will be done regarding general features only. The final part of the introduction will be about Fiber Grating sensors, including elaboration on its details. The theory behind FBGs will be presented accordingly, how it works as a sensor, followed by its uses as a sensor.

Consequently, we will be covering the FBG detection schemes, which consist of wavelength-amplitude conversion technique, wavelength-position conversion schemes, matched FBG pairs, tunable filters, interferometers such as Mach–Zehnder and Michelson filters. Also, there are charge-coupled device (CCD) spectrometers, resonated by our extensive use of optical spectrum analyzers (OSAs). The choice of interrogation scheme, which is using a tunable laser source (TLS), also covers a variety of configurations, will be covered in detail.

## **2.2 Overview of Fiber-based Sensors**

Fiber-based optical sensors come into play in our lives in a myriad of applications, especially concerning Fiber Bragg Gratings (FBGs). Utilizing the strain/pressure response of FBGs, various parameters can be detected other than the aforementioned ones, such as an optical voltage sensor (Bi & Li, 2012). Also, the usage extends to the monitoring of cardiac ablation, as demonstrated by (Ho, Razavi, Nazeri, & Song, 2012)

Additionally, changes in chemical composition of liquids can be detected due to the varying of the liquid's refraction index, such as detection of the presence of unwanted compositions in water for pollution monitoring, or petroleum hydrocarbon leakage detection (Frankel & Esman, 1995; Spirin et al., 1999).

Structural health monitoring techniques have also benefited from FBGs as demonstrated by University of Malaya's Photonics Research Group (PRG), where a fiber-based sensor was embedded in Panglima Awang bridge, Kampung Morten, Melaka in 2012, which also recently is adapted in Hubei Jing Yue Yangtze River Highway Bridge (Yue, Xiang, & Yang, 2012). Steel structures also benefit from this sensing technique, such as communication tower structures. (Antunes, Travanca, Varum, & André, 2012).

Configurations of interferometers, such as the ubiquitous Michelson, Mach-Zehnder, Sagnac and Fabry-Perot interferometers have been developed for various fiber sensing-based applications. The uses can be as similar as stated before, with a sensing arm from the fiber length.(L. Zhang, Zhang, Bennion, Lee, & Jeong, 2008).

Also, novel Flat Fibres, which are first produced and having UV-written channels by Optoelectronics Research Centre, University of Southampton (Holmes et al., 2008). This research recently has been adapted by our research group are also produced by our lab, are one of the fine innovation on fiber sensors. The Flat Fibers also has a prospect on integration with surface plasmon resonance (SPR) as a biosensor for detection of viruses (Kumbhat, Sharma, Gehlot, Solanki, & Joshi, 2010), also being worked out in our research group. This shows how versatile fiber sensors can be.

### **2.3 Fiber Bragg Gratings**

The first FBGs, which will be the main focus in this work, was produced in the year 1978 (Hill, Fujii, Johnson, & Kawasaki, 1978), hitherto spanning more than 30 years as of the year 2012. Further advancements were made and as of now, there are many applications, in which conventional sensors are rendered inapplicable which can be accomplished using FBGs.

An FBG is basically a glass fiber, single-mode, with gratings etched in segments in a small length. The segments vary in the refractive index coefficients with respect to the core of the fiber. When a broadband light source is guided through the FBG, it will reflect a narrow and certain range of wavelength and part of the power of the light. (L. Zhang et al., 2008).

A basic setup to monitor an FBG's spectral response is as shown in Fig. 2.1.

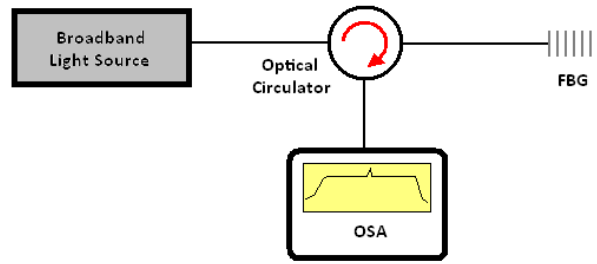


Figure 2.1: Schematic diagram of a basic setup to monitor an FBG

Due to the segmentation of the glass which makes it a periodic modulator for input signals, the response of the FBG is as shown below:

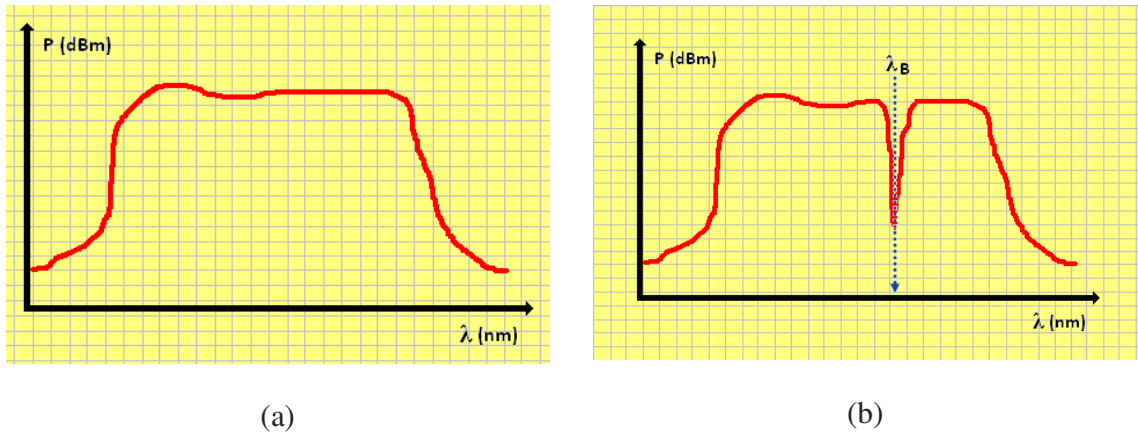


Figure 2.2 (a): A broadband source input for the FBG; (b) transmission spectrum of the FBG, showing the filtered region with  $\lambda_B$  as the central wavelength.

A broadband light, directed into an FBG grating produces such a response due to the nature of the phase matching condition, as stated in the equation below:

$$\lambda_B = 2n_{eff}A \quad (2.1)$$

where the parameters are  $\lambda_B$ = wavelength of the peak reflectivity,  $n_{eff}$ = effective refractive index of the guided mode in the fiber, and  $A$ = period of the refractive index modulation.

From the equation above, the period of the refractive index modulation,  $\Lambda$ , is further characterized with a form of the function in Eq. 2.2:

$$n(z)=n_{co}+\delta n[1+\cos(2\pi z/\Lambda)] \quad (2.2)$$

Where the parameters are detailed as  $n_{co}$  = unexposed core refractive index, and  $\delta n$  = amplitude of the photo-induced index excursion. This allows the light propagating in through the fiber while undergoing modulation, in which the periodic grating makes the forward propagating light to be coupled into the backward propagating light, producing a reflection response (L. Zhang et al., 2008).

The characteristics mentioned above are achieved when the fiber is fabricated with certain methods. The pioneers of FBG fabrication reported the method to direct an intense UV interference fringe pattern free-space two-beam holographic method, where a laser beam is split half and recombined to produce an interference pattern, which has a highly precise periodicity. This interference node is directed towards a photosensitive fiber and the grating will take form according to the interference pattern (Meltz, Morey, & Glenn, 1989).

Another method is by the diffractive phase mask technique towards the core of the fiber. This is achieved by directing laser on a transparent plate with a chirp pattern throughout the material, and thus produces the gratings when the diffraction penetrates through the fiber (Hill et al., 1978). Basically, the setups are as shown in Fig. 2.3.

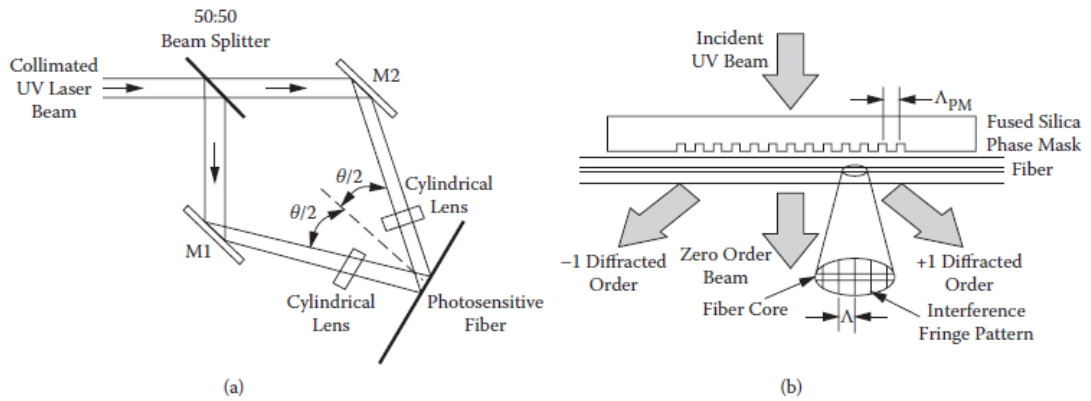


Figure 2.3: FBG fabrication techniques: (a) free-space two-beam holographic interference and (b) diffractive phase masking technique (L. Zhang et al., 2008)

Both methods were modified and improved over the years with different setups. One of the recent developments highlighted the need to produce longer FBG lengths and with more uniform structures arise, which suggested the use of multiple phase masks, and this produced complications. This is achieved by modifying the reconstruction-equivalent-chirp (REC) algorithm to control the laser profile and the translation stage, as shown in Fig. 2.4, to address the various issues regarding the reflection profiles of the FBG by using two phase masks (Dai, Chen, Xia, Zhang, & Xie, 2004).

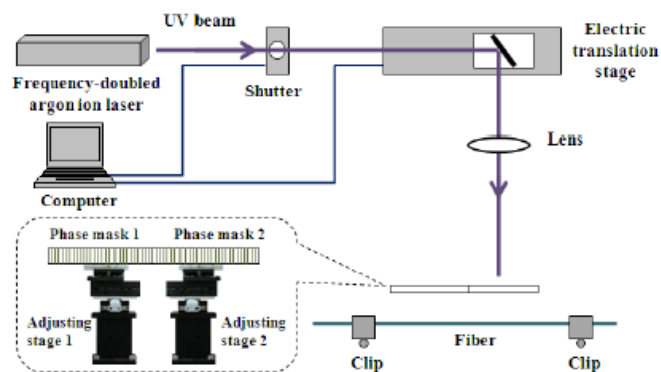


Figure 2.4: Schematic configuration of the FBG fabrication system with two phase masks (Gao, Chen, Xiong, Liu, & Pu, 2012).

As the light which goes through the chirped material, the original phase-shift (OPS) makes the reflection profile of the FBG to be relatively imperfect, caused by the phase mismatch of the two phase masks. As (Gao et al., 2012) has demonstrated, by fabricating it with two uniform phase masks and a translation stage with micrometer precision worked out the compensation of the OPS. This resulted in better profiled FBGs as long as 90mm, which shows great potential.

As summarized by (L. Zhang et al., 2008), there are several types of FBGs, namely the uniform period, phase shifted, chirped, array structures, and several other structures. However, in this work, the prime focus will be siphoned into the ubiquitous uniform-period FBG type, which is selected for its ubiquity in our applications.

## **2.4 FBGs as sensors**

As explored within our research group, we have applied FBGs in various applications, namely for sensing of temperature, corrosion, liquid refractive index changes for pollution, strain and so on. The way FBGs work for these applications will be covered in the following sections.

An FBG exhibits sensitivity towards temperature and strain, due to the mechanical variations to the grating structure. This is due to the nature of the grating itself; when strain is induced in the fiber, the gratings' structural periodicity will also vary. This is where relatively minuscule movements can be observed via certain setups, such as described in Section 2.3.

With respect to thermal response, the fiber will experience a physical change due to its thermal expansion coefficient. This defines the method which utilizes its thermal response. In short, the correlation between temperature, strain and wavelength shift with respect to the spectral behavior of an FBG is as shown in Eqn 2.3:

$$\frac{\Delta\lambda_B}{\lambda_B} = P_e \varepsilon + [P_e(\alpha_s - \alpha_f) + \zeta] \Delta T \quad (2.3)$$

where  $\lambda_B$  = reflected spectral wavelength of the FBG,  $\Delta\lambda_B$  = the shift of reflected spectral wavelength of the FBG,  $P_e$  = strain-optic coefficient,  $\alpha_s$  = thermal expansion coefficient of the material bonded to the fiber,  $\alpha_f$  = thermal expansion coefficient of the fiber (which bore gratings) itself,  $\zeta$  = thermo-optic coefficient, and  $\Delta T$  = the change in temperature (L. Zhang et al., 2008)

The spectral response of an FBG is graphically shown in Figure 2.5 below:

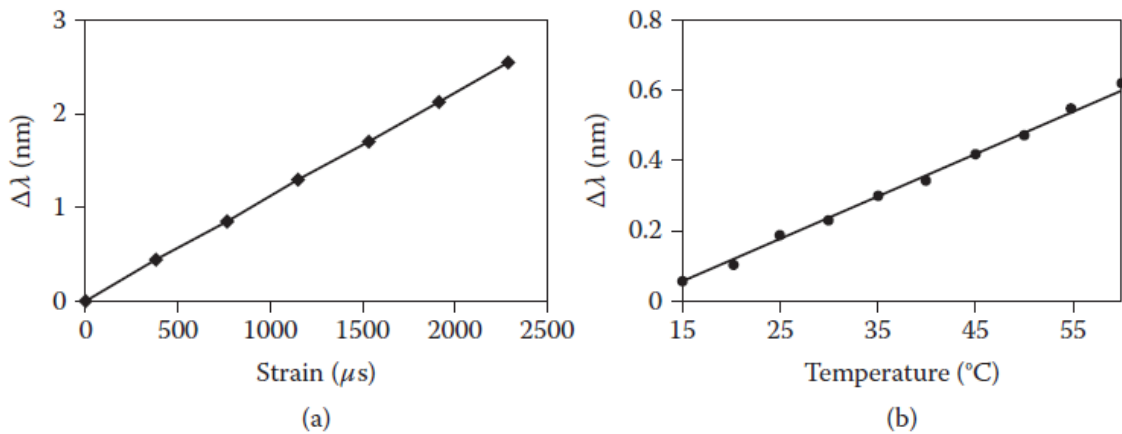


Figure 2.5: Wavelength shift response of the FBG towards a) Strain, and b) temperature (L. Zhang et al., 2008).

As shown in the figure above, the relation between temperature and wavelength shift shows linearity, as much it does for the strain as the variable. This feature allows us to utilize the FBG as a sensor. As shown in the figure above, the normalized strain response was found to be  $0.78 \times 10^{-6} \text{ microstrain}^{-1}$  and the normalized thermal responsivity at a constant strain was  $6.678 \times 10^{-6} \text{ microstrain}^{-1}$  (L. Zhang et al., 2008).

Applications of FBG sensors for temperature and strain are still explored in various conditions, such as detection of temperature using bimetallic strain sensors (Ismail et al., 2011), and strain or pressure (Bremer et al., 2012).

## **2.5 Interrogation techniques of FBGs**

In this section, various interrogation schemes will be discussed, and the selected design scheme will be highlighted in detail. There are several techniques to interrogate FBGs, and each technique differs in cost, precision, accuracy and efficacy.

### **2.5.1 Wavelength-Amplitude Conversion**

This method is fairly direct; the wavelength change is converted into amplitude by several types of setups. An edge filter, which varies its optical power output versus the wavelength of the light guided through it, as shown in the inset of Fig. 2.6(a), is quite common. However, its resolution is limited. Another variation of the setup, as per Fig. 2.6(b) is to guide the signal through a fuse-tapered wavelength demultiplexer (WDM), where the WDM exhibits a transfer function of 0.4dB/nm (as shown in the inset), and thus drift compensation of the wavelength shift can be achieved (L. Zhang et al., 2008).

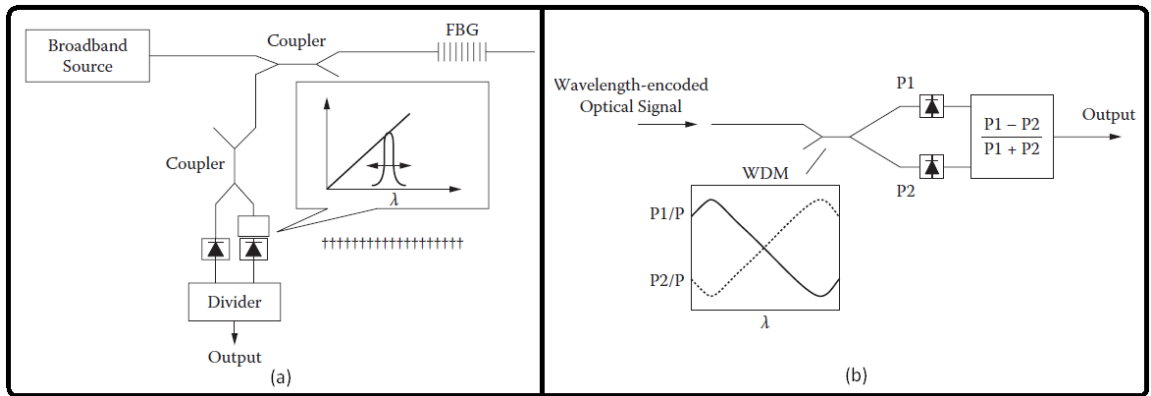


Figure 2.6 (a): Edge filter interrogation setup (b) WDM Setup for coupling fiber (L. Zhang et al., 2008).

### 2.5.2 Wavelength-Position Conversion

Wavelength-Positioning conversion is achieved in similarity with spectrometers, where spectrometers disperse the incoming light and a CCD sensor translates the intensities at different wavelengths, and outputs a spectral profile. The bulk gratings are employed in the setup with a fixed position, and disperse the light and reflect the light to a CCD image sensor (L. Zhang et al., 2008).

Wavelength positioning is achieved as depicted in Fig. 2.7:

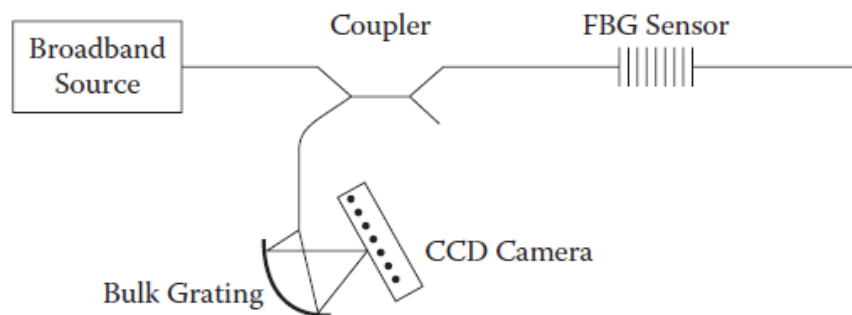


Figure 2.7 Wavelength positioning using bulk gratings (L. Zhang et al., 2008).

This setup has a disadvantage with the use of bulk optics, which will affect its mobility for its critical positioning, making it difficult to be used in harsher environments.

### 2.5.3 FBG Matching

Coupling gratings with the sensor grating is where two matched Bragg gratings can be cascaded together, where one acts as the sensor itself, and the other grating acts as a tuning mechanism by several methods. The setup is shown in Fig. 2.8:

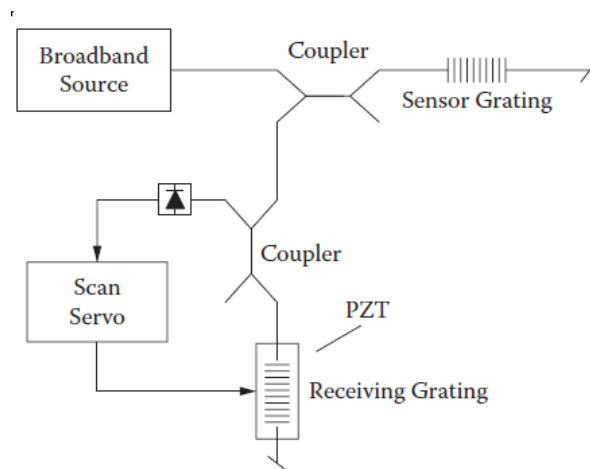


Figure 2.8: Matched FBG interrogation setup (L. Zhang et al., 2008)

The FBG, which is to be periodically tuned by mechanical methods, in this case being a piezoelectric transducer (PZT) will be matched with the wavelength which is varied. Several methods also have been developed under this theme, such as using chirped fiber gratings, and interferometers such as a Fabry-Perot filter and so on (L. Zhang et al., 2008). This method is very economical and the sweeping frequency for a continual reading can reach high frequencies; however it has a small range of bandwidth for detection. This method was recently employed for strain sensing in railway stations (Z. Zhang et al., 2012).

### 2.5.4 Tunable Filters

The use of optical tunable filters (OTFs) are also popular, where the filter can be varied using several mechanisms. The filter will sweep through the wavelengths and will return a reading when it detects a peak as shown in Fig. 2.9, which signifies the reflected wavelength of the FBG (L. Zhang et al., 2008). Optical Tunable Filters are essential for a myriad of optical circuit setups, allowing only a limited bandwidth to be undisturbed. Fiber sensor interrogation benefits from these components as well (Ming Gang, Geiger, & Dakin, 1996).

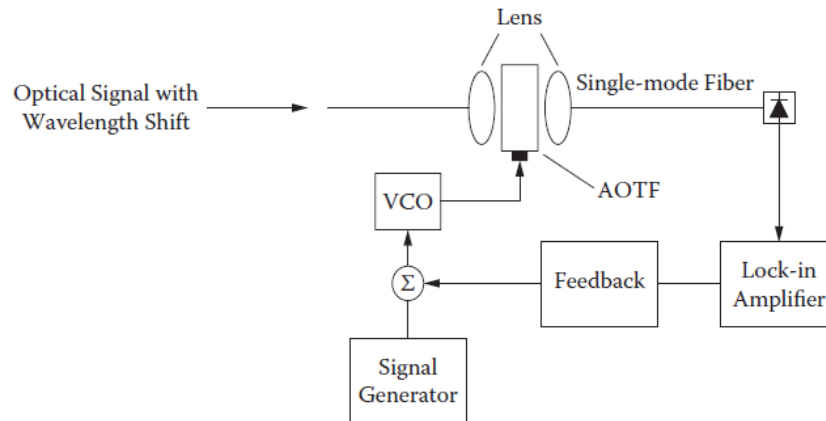


Figure 2.9: A tunable filter interrogation setup (L. Zhang et al., 2008)

There are various mechanisms which makes optical filters tunable. The most popular one is an acousto-optic tunable filter, with even more recent designs with increased accuracy (Zhu, Zhang, & Zhao, 2012). Also, there are designs employing elasto-optic effects (Prakash Dwivedi & Lee, 2012). Motorized ones are commercially available, such as the one produced by Dicon Fibreoptics Inc. (Fibreoptics Inc., 2001). This tunable filter boasts a 30nm range, an I<sup>2</sup>C communication protocol, a resolution of 0.05nm, powered up with ±12V DC, at 350 mA, a tuning speed of 50 -1400 milliseconds within the range.

However, these components are relatively costly compared to a normal mechanical tunable bandpass filter, such as the one produced by Alnair Photonics (Labs Co., n.a.) . Other mechanisms include a thermo-optical tunable filter for fiber interrogation was also reported (Passaro, Tsarev, & De Leonardis, 2012).

### 2.5.5 Interferometers

The use of interferometers to interrogate FBGs is as shown in Fig. 2.10:

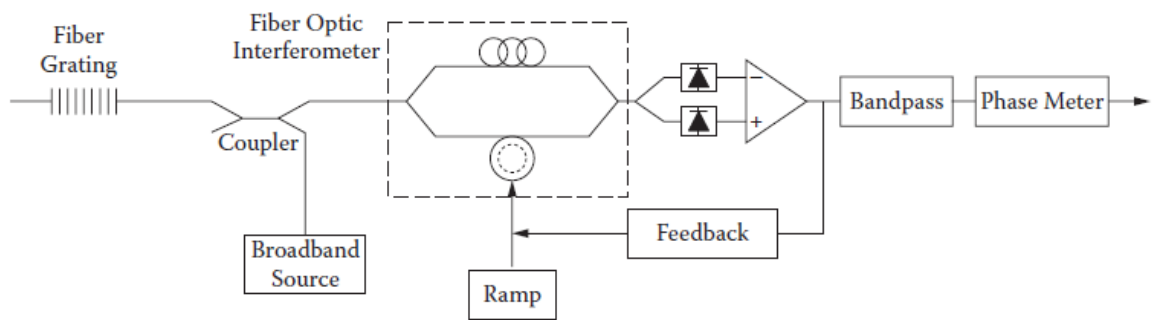


Figure 2.10: Interferometric interrogation (L. Zhang et al., 2008)

The interferometer, which acts as a filter is adjusted using similar methods as mentioned in section 2.3.4. Recent applications, other than the basic parameters such as temperature, strain, and so on, includes distance measurement with micrometer precision using a Michelson interferometer (Alzahrani et al., 2012), as a humidity sensor using a Fabry-Perot filter, detection of liquid refraction index using a Mach-Zehnder interferometer (Wo et al., 2012). A high precision displacement sensor via a Sagnac Loop (Bravo, Pinto, Lopez-Amo, Kobelke, & Schuster, 2012) and so on, are all applications of interferometers as sensors.

Interrogation of FBGs using interferometers was finely demonstrated by using a Fabry-Perot filter to single out the desired bandwidth combined with a Mach-Zehnder interferometer to allow the matched output using wavelength division multiplexing (WDM), detected using photodiodes (Koo & Kersey, 1995). Recent works include the employment of Fourier analysis for the piezoelectric tuning of a Fabry-Perot filter to interrogate FBGs. (Wada, Tanaka, & Takahashi, 2012).

### **2.5.6 Spectrometry**

Spectrometers have gained supremacy in investigating fibers' spectral profile, and it is evident in the usage of Optical Spectrum Analyzers (OSAs) in which no photonics lab cannot do without. UMPRG, as for the year 2012, has four OSAs (priced between RM95-195k) and a Bayspec's FBG Analyzer (FBGA, priced at RM20k), which is also a simpler form of a spectrometer. The OSA has limitations due to its bulkiness and immobility, while the FBGA, while being superior in terms of speed and robustness, still requires a light source for the FBGs.

Spectrometers consist of phase gratings, which reflects a collimated light and disperses the incoming light and a CCD sensor digitizes the power and wavelength in discrete ranges of selected bandwidths. This system has few key winning features- a large dynamic range, and the ability to detect very weak signals due to the collimation of the input light (L. Zhang et al., 2008). A simplified configuration is shown in Fig. 2.11.

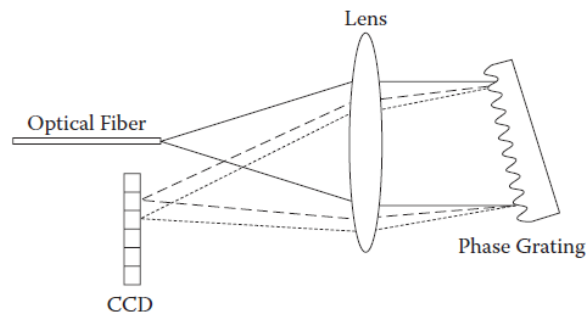


Figure 2.11: Spectrometer setup (L. Zhang et al., 2008)

However, the main disadvantages, which is the main drawback for most field tests conducted by the researchers in our lab, is due to its bulky appearance, large weight and high cost ranging between RM95k-RM200k.

### 2.5.7 Tunable Lasers

A basic setup to interrogate an FBG using a TLS would be as follows:

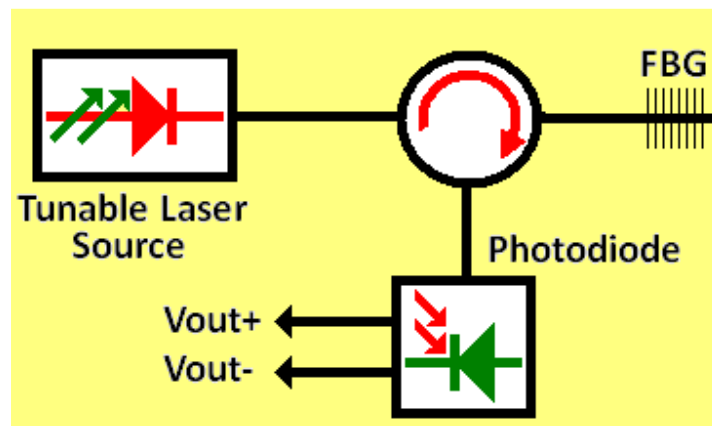


Figure 2.12 Tunable Laser FBG Interrogation

As the laser is tuned (while matched digital values give the current wavelength of the laser) the spectral profile is revealed via the voltage output of the photodiode, which converts optical power into electrical signals which can be read using various methods.

However, the main concern in our setup is the tuning mechanism, responsible for the tunability of the laser. Researchers have been using manually tunable filters (Bellemare et al., 2001; Yamashita, 2001). Various tuning mechanisms have been reported for different EDFA laser setups. Inducing physical strain on fiber filters have been a popular approach, being much lower in cost and robust. These include a mechanically strong Deuterium-loaded FBG as a tuning filter (Song et al., 2001). Long-period fiber gratings (LPFGs) were also used (Shi, Zhu, Chen, Deng, & Huang, 2012). Bending SMF arm for tuning was also recently reported (Gao et al., 2012). However, fiber bending/stretching schemes have been known to be difficult to calibrate, and may not be easily repeatable by other researchers. Also, it has a tendency to occasionally break due to mechanical stress (Paterno, Haramoni, Silva, & Kalinowski, 2007).

This makes reversion to standard tunable filters desirable. This method costs more than fiber filter strain-tuning methods, but the laser formation occurs with higher tunability compared to fiber filters (Song et al., 2001). There are various types of tunable filters. Although the aforementioned components are higher in precision and quality, they are also much more costly compared to a manually tunable filter, which performs equally well within the spectral domain.

## **2.6: Chapter Summary**

The basics of fiber-based sensors are covered, and the main sensor, namely the FBG, which is the central concern of our discussion, was briefed accordingly. Included in the discussion was on the structure of an FBG, how it works as a sensor, and its theoretical principles.

We proceeded to the interrogation schemes of an FBGs, namely methods such as wavelength-amplitude conversion, FBG matching, tunable filters, interferometers, spectrometry, wavelength-position conversion and finally on tunable lasers, in which the referred literature which bore the closest relation to our work was chosen for our elaboration.

The following chapter will deal with the details of the chosen scheme, which are tunable lasers.

## **CHAPTER 3**

### **INTERROGATION OF FIBER BRAGG GRATINGS VIA TUNABLE RING LASERS**

#### **3.1 Introduction**

In this chapter, we will be covering the details of interrogation via tunable laser setup, which includes theory, design, and how a tunable laser works as an interrogator with different approaches, and concluding the part with the chosen tunable laser design, an Erbium-doped fiber amplifier (EDFA) ring laser.

Next, two critical components will be elaborated, namely the 980nm pump laser, and the tunable bandpass filter (TBF) with regards to their circuitry, mounting and modeling. Finally, the complete design and how it works as a fiber Bragg grating (FBG) interrogator will be presented.

#### **3.2 Tunable Lasers**

In this section, we examine the details of a design of a tunable laser, and in the following sections, a tunable laser setup is chosen, which is a EDFA ring laser. One of the popular designs chosen was also constructed by (Sola, Martín, & Álvarez, 2002), and their setup will be the central reference.

### 3.2.1 Role of Tunable Laser in FBG Interrogation

The most direct method of interrogating an FBG shown in Fig 3.1:

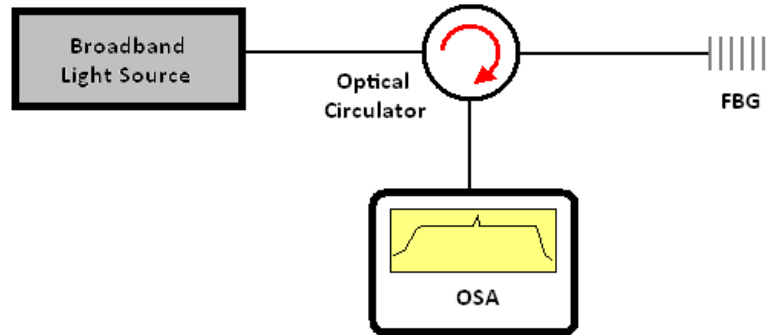


Figure 3.1: Schematic diagram of a basic setup to monitor an FBG

The broadband light source provides a wide bandwidth of output light source, where the FBG's reflected signal will appear via the optical spectral analyzer (OSA). The central wavelength of the reflection profile will shift according to the response of the FBG, when any parameter of the FBG changes. However, a tunable laser's part for interrogation will be slightly different.

The following shows the spectral profile of a typical laser profile as shown in Fig. 3.2:

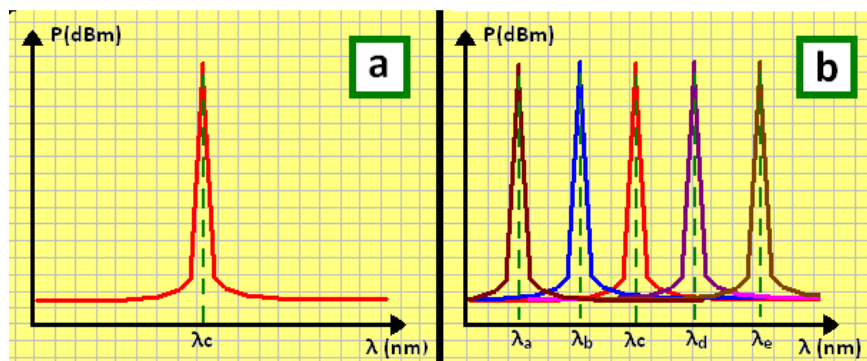


Figure 3.2: Spectral profile of a) a single laser. b) laser tuned along a defined bandwidth with periodic positions.

As shown in Fig. 3.2, a laser exhibits concentrated power at a very small bandwidth with a center wavelength of  $\lambda_c$ . A tunable laser, however, varies its profile with respect to its wavelength, while ideally maintaining its power throughout the spectrum. As shown in Fig. 3.2(b), the spectrum can be varied along a certain bandwidth, while the laser maintains its profile, with samples of wavelengths of  $\lambda_a$  to  $\lambda_e$ .

A tunable laser source's role in FBG interrogation can be demonstrated via the setup as shown in Fig. 3.3.

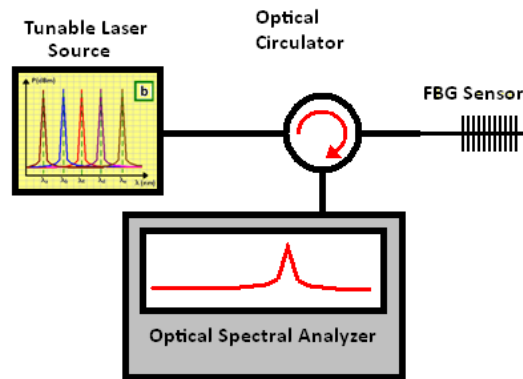


Figure 3.3: Setup to observe the role of a TLS in FBG interrogation

The output profile setup of an interrogation of an FBG using a tunable laser source (TLS) is shown in Fig. 3.4.

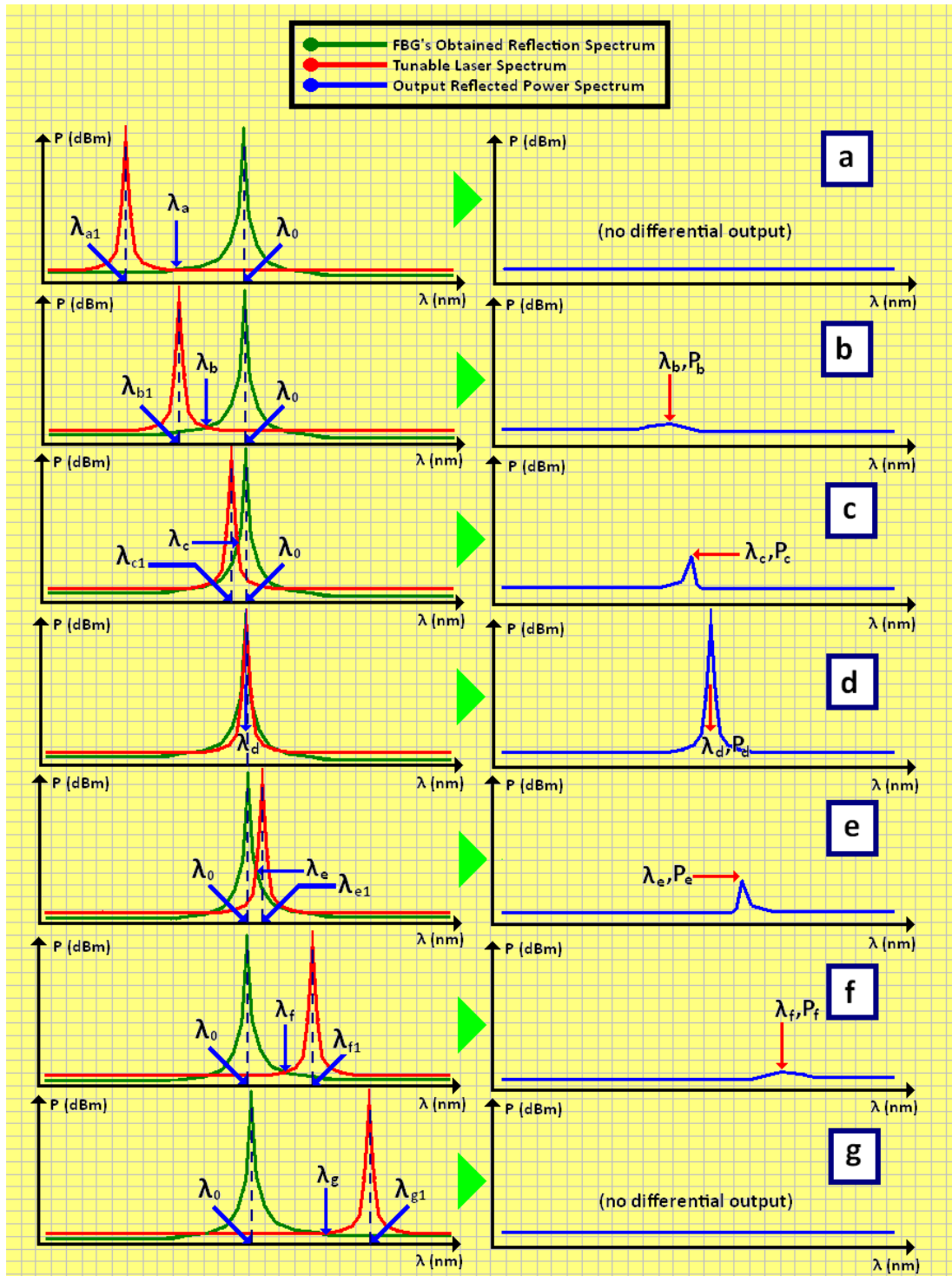


Figure 3.4 Sweep of the TLS along an FBG's spectrum, on the left is the spectral profile of the laser and the FBG; the right shows the spectrum via an OSA.

As shown in Figure 3.4, (a) the laser spectrum at position  $\lambda_{a1}$ , while the FBG's reflection spectrum is fixed at  $\lambda_0$  throughout the sweep. An FBG which allows a certain amount of power will result in a low power output along the spectrum, although it does not exhibit any peak.

As the laser is tuned and reaches  $\lambda_{b1}$  at (b), it starts to reach the edge of the FBG's reflection profile. Therefore the power output shows a slight elevation along the spectrum as shown at  $\lambda_b$ . This is followed by a sharper rise, at (c) as the tuning reaches  $\lambda_{c1}$ , and is shown at  $\lambda_c$ , with a peak power of  $P_c$ . At (d), the central wavelength of the reflection spectrum of the FBG is reached at  $\lambda_d$ , showing the maximum power,  $P_d$ . The sweeping process gradually recedes and shows the transition along  $\lambda_e/P_e$  at (e),  $\lambda_f/P_f$  at (f) and finally settles down at (g) without any peak profile.

Consequently, we can plot the peak power of each section against the central wavelength of the tunable laser, and the FBG's profile can be obtained as shown in Fig. 3.5.

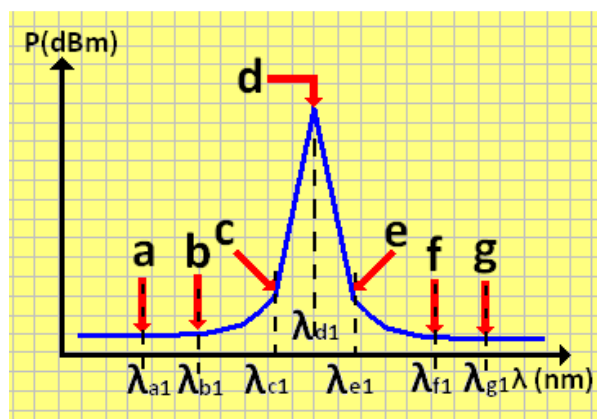


Figure 3.5: A plot of the peak power of each section versus the laser's central wavelength

With this, we have obtained the central wavelength of the FBG's reflection spectrum, as shown in Fig. 3.5e, where the peak power occurs at (d). Similarly, the previous setup can be modified for further simplification, which renders the interrogation portable, by replacing the OSA with a photodiode, as shown in Fig. 3.6.

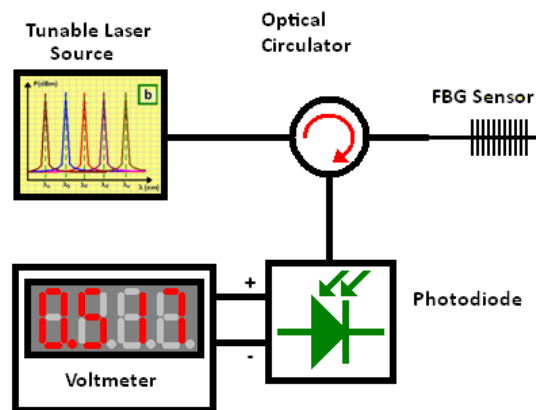


Figure 3.6: FBG interrogation via TLS Setup

In this setup, the TLS is coupled to an optical circulator, where the reflected signal from the FBG will be fed to a photodiode, converting the optical power into electrical. A test FBG is interrogated using the setup above, and the output shown by a voltmeter versus the laser's central wavelength (refer Appendix A) is as shown in Fig. 3.7.

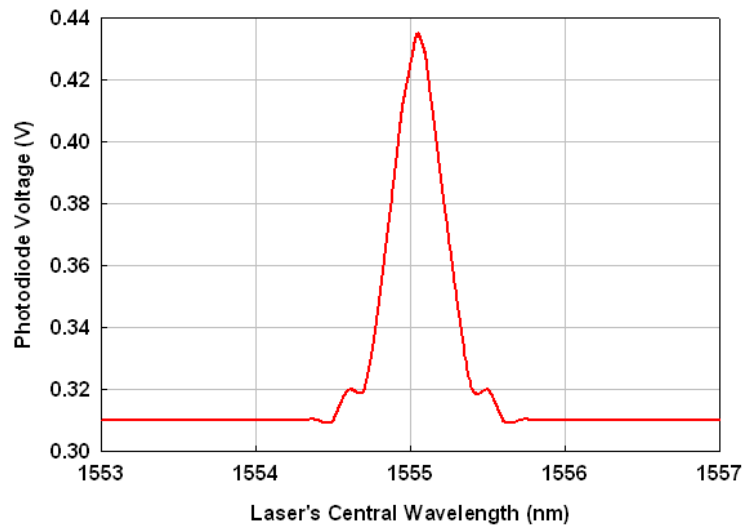


Figure 3.7: Output profile of an FBG interrogation (refer setup in Fig. 3.4 & Appendix A)

In this case, the TLS used is EXFO's IQ-2600 with test system IQ-203, which displays the laser's central wavelength via a graphical user interface (GUI). From the figure above, the central wavelength is 1555.05nm. The profile of the output voltage versus the wavelength of the laser shows the reflection spectrum of the FBG.

Note that the profile obtained above, which is a voltage-versus-wavelength relation is exactly similar to the characteristics of a power-versus-wavelength profile of an FBG. This shows the consistency of the interrogation exercise.

### 3.2.2 Utilized Tunable Laser Design

An EDFA tunable ring laser scheme is chosen as our tunable laser source, for several reasons. Being much lower in cost, the most pricey item is the TBF, which costs around RM3000. The total cost to construct a complete tunable laser circuit is around RM5000. This is considerably lower than a Yokogawa AQ6370C, priced at around RM100-200k, or BaySpec's FBGA, which costs around RM20k.

Also, a tunable ring laser is robust. The whole optical circuitry can be miniaturised in a single module, making it portable, which is a very important feature. Finally, there are only four key electronic issues which need to be dealt with. They are the laser pump driver, the tunable bandpass filter's actuation, the photodiode current-voltage conversion and the central control required to complete the interrogation.

A design of the EDFA ring laser is as shown below:

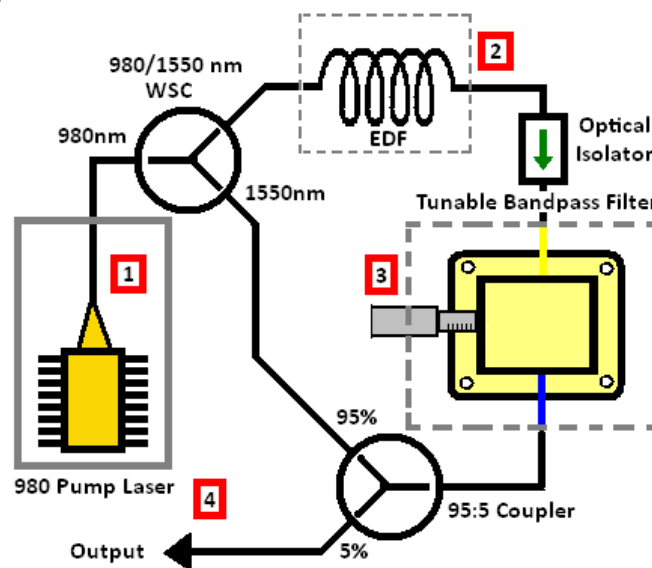


Figure 3.8 EDFA tunable ring laser setup

The systems starts with the 980 nm pump laser (Marked 1 in the figure), which is channeled to an Erbium-Doped Fiber (EDF) via a 980/1550nm Wavelength Selection Coupler (WSC). The EDF needs to be of a certain length (Mark 2), where the properties of the fiber allow a spectral emission within the C-band (1520-1580 nm). In other words, an

amplified spontaneous emission (ASE)<sup>1</sup> profile is produced. The optimal length of the EDF can be configured by simulation or manually splicing different fiber lengths.

An optical isolator is cascaded in the following to ensure the laser only takes a single direction. This ASE is further reshaped through the Tunable Bandpass Filter, or TBF (Marked 3, or it could be of any type of filter). 95% of this filtered light will be coupled into the 1550nm fiber end of the WSC, completing the ring cavity. This will produce a ring cavity resonance, where 5% of the laser, which finally forms, is channeled out at Mark 4. The tuning range is dependent on the cavity loss; a range of percentage allows the laser to be formed in the cavity, where feeding higher power of the generated ASE into the ring cavity allows wider tunability, and vice versa (Bellemare et al., 2001).

The spectral profiles of the formation of the laser are as shown in Fig. 3.9:

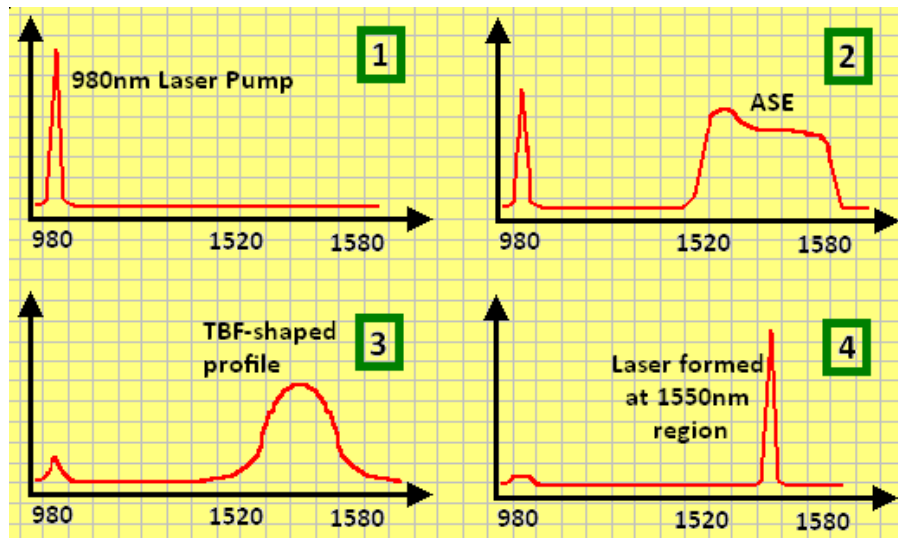


Figure 3.9: Spectral profile of several stages in ring lasing

<sup>1</sup> An *amplified spontaneous emission* (ASE) is formed due to the properties of an Erbium<sup>3+</sup> doped fiber (EDF). When a 980nm pump laser is guided through an EDF, the energy level of the Er<sup>3+</sup> ions will excite to higher energy levels. Due to obeying the law of conservation of energy, the ions will decay, especially between levels <sup>4</sup>I<sub>13/2</sub> and <sup>4</sup>I<sub>15/2</sub>, producing photons, which scatter around the C-band (1520-1560nm) region, which results with the ASE profile. (Miniscalco, 1991)

Fig. 3.9 is explained as follows (the designated “green marks” numbered 1-4 correspond to both Fig. 3.8 and 3.9):

At Mark 1, the laser shows a high power profile at the 980 nm region. Mark 2 shows the output at C-band light after being amplified. One can observe that the 980 nm laser’s power is lower; it is transferred to the power output of the ASE produced. Then, at Mark 3, the ASE is reshaped according to the profile of the TBF (this profile may vary according to types of filter used in this setup). Mark 4 depicts that after running through the ring cavity, a resonance is formed as the TBF-shaped profile runs through the ring cavity. In a very brief moment, the bandwidth formed starts to compress the power at its centre with successive cycles along the ring cavity, which results in a laser is formed at a higher power (Heebner, Vincent, Schweinsberg, Boyd, & Jackson, 2004). Residual power of the 980 nm laser can still be seen but barely significant.

### **3.3: Control of a 980 nm pump laser**

There are a few issues surrounding the usage of a 980nm pump laser, as to why is the module chosen for this work, its advantages, and the steps taken to control the laser. The following sections elaborate this matter.

#### **3.3.1: Justifications for opting a 980nm pump laser**

A 980nm pump laser is needed since the EDFA works mainly at two wavelength regions of a pump laser; the other one is a 1480 nm laser (other wavelengths also exist, but only both are mentioned due to insignificance of the other wavelengths). However, we opt for 980nm pump lasing for several reasons, which are:

- a) 980 nm lasing produces less noise in EDFA
- b) Being only 70nm apart from the C-band, which is in the region of 1550nm, A 1480 nm laser also has a significant spectral proximity with the C-band light, therefore it will influence the formed laser power in the cavity.
- c) For this reason stated above, a 1480 laser pump will require a step-type WDM. It is preferred to use a normal 980nm/1550nm WDM for reasons pertaining to familiarity.
- d) A 980nm has a spectral distance of 570nm from the C-band, which makes it perfect for our application, where the laser does not require special care due to the high spectral distance, since the aim is to use the least optical components for the laser construction.

All of the comparison displayed above was provided in earlier works, regarding a case study of ring lasers using 980nm and 1480 laser pumps (Sola et al., 2002).

### 3.3.2: 980nm Pump Laser Driver

A 980 nm pump laser module was purchased from Agere, (model number SL980S31C).

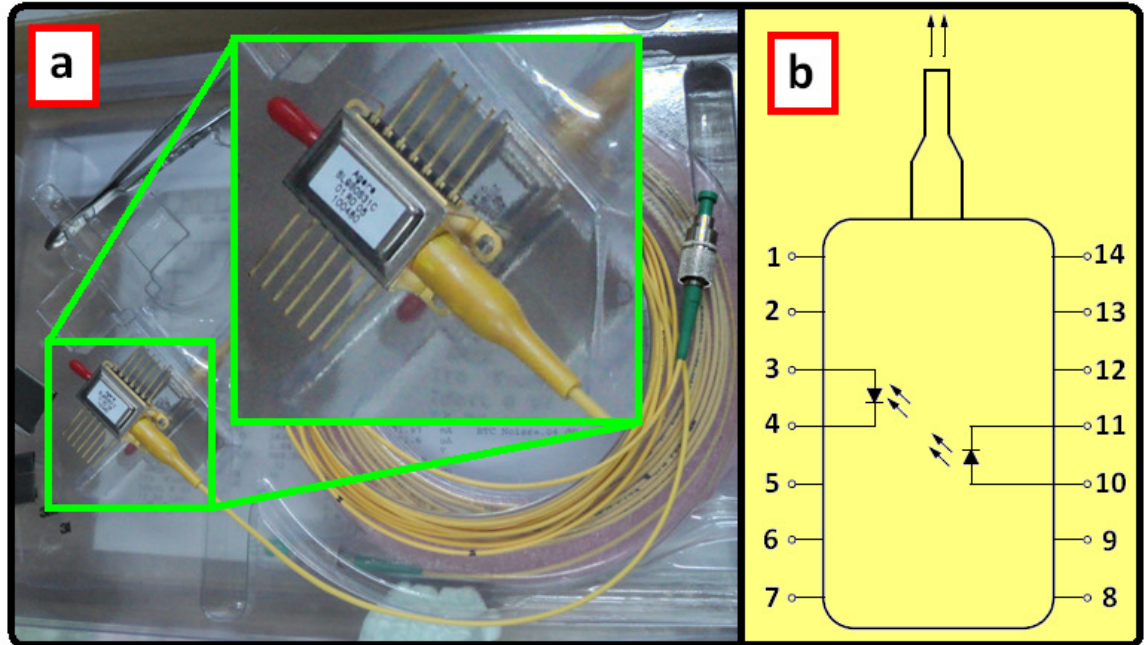


Figure 3.10: a) A 980 nm pump laser module from Agere, with an enlarged view on the Butterfly casing, with an FC-APC connector b) Pinout diagram (as stated in datasheet)

According to the pinouts of the laser module, the pins 11 and 10 are the terminals of the laser itself, and the photodetector has pins 3 and 4 for photodetection, in which the monitoring of the laser power can be done internally within the design.

The pump laser, as mentioned in section 3.3.1, functions with a maximum voltage 2.2V, at 200 mA. Therefore, we will need to have a regulator to manage the voltage and stabilize the current of the laser. A Texas Instruments' LM317L, which is a variable voltage regulator boasts adjustable voltage regulation, and delivers 100 mA of current, where a low-power solution is very desirable in our case.

Also, we will require a switching capability, therefore a low-cost switching transistor is ideal for this application, such as the 2N2222. In short, we will have a readily electronically switchable 980 nm pump laser, at a regulated voltage while delivering a low amount of current for power-saving, and battery-operable.

A simple circuit can be demonstrated via a circuit design software eg. Altium Designer as shown in Fig. 3.11:

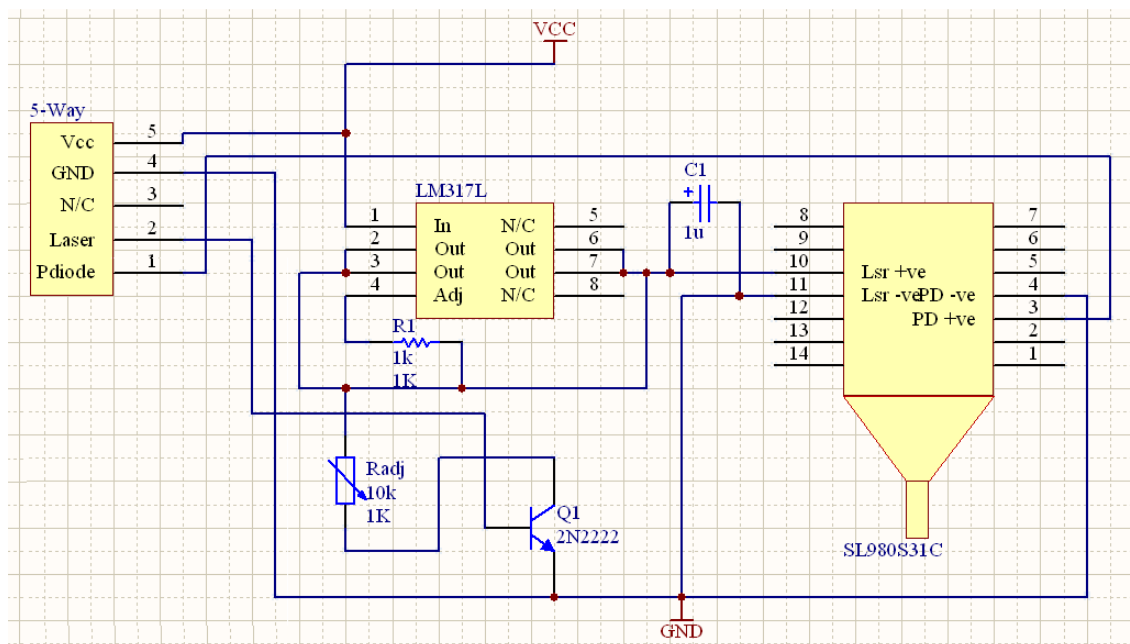


Figure 3.11: Control circuit for SL980S31C 980 nm pump laser

The circuit is robust, exhibits switching capability, and is low power. The LM317L's output voltage can be varied to the desired voltage by tuning the knob of a precise potentiometer, while monitoring the output of the laser using an OSA. All of the pinouts are reduced to only four pins, which can be controlled via external circuits, in which as shown in the leftmost side designated 5-way connector.

### 3.4 Controlling a Tunable Bandpass Filter (TBF)

There are key issues especially in the mechanical aspects of the filter setup which needs to be addressed. The filtering mechanism of tunable lasers has been an ongoing research, where this section deals with details which makes the tuning setup controllable.

#### 3.4.1: Electromechanical Aspect

A tunable bandpass filter (TBF) is the central component of the setup, since it fixes the central wavelength of the laser itself. Stability of the position of the laser is essential since interrogation requires the exact spectral parameters of FBGs at each section of the wavelengths. Therefore a TBF holds the utmost importance in the design. The TBF used in our setup is Alnair's, with a 3dB bandwidth of 1.2 nm.

The TBF purchased for the setup is shown below:

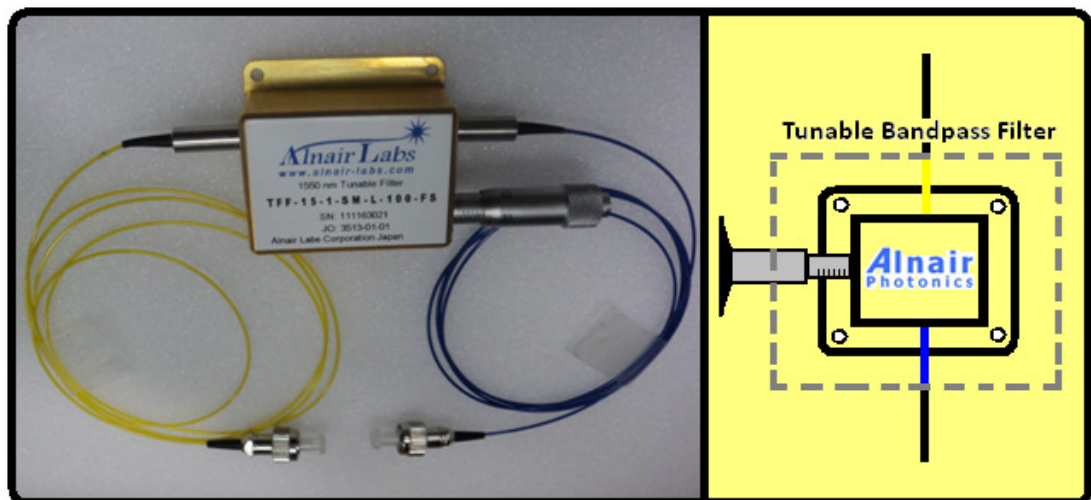


Figure 3.12: A tunable bandpass filter (TBF) from Alnair Photonics; inset is for reference with the whole design

As the filter is tuned radially, we opt for mechanical actuation, and incorporating rotational sensing to communicate the central wavelength of the laser with the control scheme. A simple actuation mount for this TBF is as shown in Fig. 3.13:

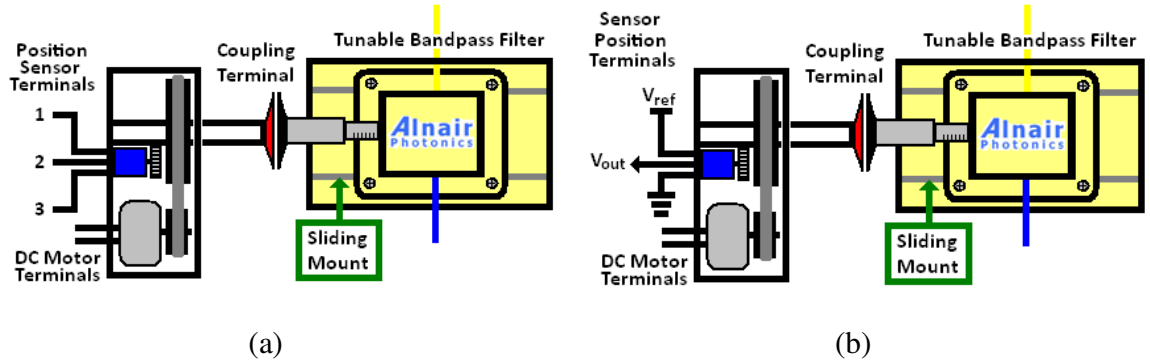


Figure 3.13(a): A TBF mount design, (b) Connections made for setup

Referring to the design above, a positioning sensor, namely a 3-pin potentiometer gives out the voltage, which can be matched to the laser's wavelength, and the TBF is actuated using a simple DC motor, which only needs to be driven using a low-power Push-Pull Driver. A sliding mount is needed, since when the TBF's knob is turned, the length of the tuning arm also changes with the dynamics of a screw. Therefore a sliding mount will compensate the change position of the whole TBF by relieving mechanical stress.

### 3.4.2: Wavelength-Voltage Relation of the TBF Mount

Ultimately, this setup addresses to a key issue on how to determine the laser's central wavelength without using an OSA. A mathematical model can be developed for the mount, which gives out the wavelength of the laser in terms of output voltage. Mathematically expressed (referring to Fig. 3.13):

$$V_{out} = V_2 = \frac{R_{1,2}}{R_{pot}} \times V_{ref} \quad (3.1)$$

where  $V_{out}$  is the output voltage of the sensor,  $R_{1,2}$  is the resistance between the variable resistance of the tuning of a potentiometer which acts as a position sensor,  $R_{pot}$  as the full resistance of the potentiometer, and  $V_{ref}$  is the reference voltage of the sensor, which preferably is between 2-5V.  $V_{out}$  changes linearly with the tuning of  $R_{1,2}$ .

Next, after the formation of the laser, the output voltage of the sensor is plotted versus the central wavelength of the laser. This expectedly gives the linear relation:

$$\lambda(V_{out}) = mV_{out} + \lambda_y \quad (3.2)$$

where  $\lambda(V_{out})$  is the calculated central wavelength of the laser,  $m$  as the gradient of the line, and  $\lambda_y$  as the intersection of the line with the y-axis, or the zeroth wavelength, which holds true for all reference voltages.

### **3.5: Current-Voltage Conversion for Photodiode's Response Detection**

A photodiode converts optical power into current. It is the final component to indicate the power of the FBG's reflection spectrum. The higher the optical power, more current will be produced. The circuit to configure a photodiode's response in terms of voltage is shown in Fig. 3.14:

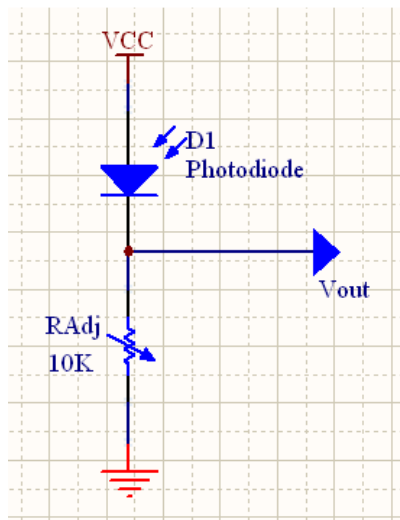


Figure 3.14: Photodiode response circuit

This circuit is essential for two reasons; first is that it converts the current into voltage effectively. A direct multimeter test onto the terminals of the photodiode, while may still show its voltage response, will eventually lead to irreversible damage to the photodiode due to spikes of voltage/current from the contacts of the multimeter. Consequently, the second reason is that it protects the photodiode from voltage spikes, due to the resistor which limits the current.

The current is converted into voltage by a potentiometer which is placed in series, where allows the voltage as an output, as stated by the relation  $V=IR$ . The output voltage is drawn from  $V_{out}$  as shown in Fig. 3.14. For a high-speed response, a low value of resistance is favored. However, a higher resistance is favored for higher voltage indication, and speed is not the issue in our case. An InGaAs Photodiode (PTD0075A1112) from AC Photonics, which operates within a region of 1000-1650nm is used for our setup.

### 3.6 Conclusion of the Tunable Ring Laser Interrogation of FBGs

A final design is as shown in Fig. 3.15 below:

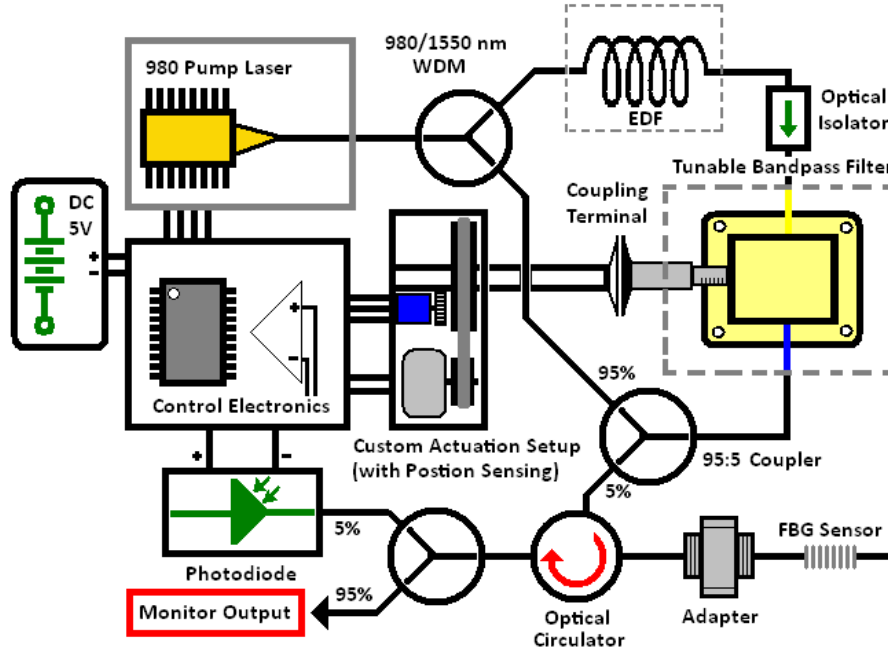


Figure 3.15: FBG interrogator with tunable EDFA ring laser setup

Fig. 3.15 shows the complete interrogation scheme for an FBG. The ring cavity allows 5% of the power to be guided into the FBG. The reflected signal is further divided into two; one goes into the photodiode for further processing and the other allows external monitoring for calibration with OSAs or spectrometers.

As the laser is powered up with the driver as discussed in section 3.3, the ring cavity forms the laser immediately. As we tune the laser by driving the actuation of the TBF, two voltage values will be observed. First, the output of the TBF mount sensor, which configure the wavelength-voltage relation will increase or decrease with the wavelength.

Second, the value of the output voltage of the photodiode will change with respect to the reflection spectrum profile. By plotting the output voltage of the photodiode versus the TBF position sensor's output voltage, the relation should take the form as shown in the following figure:

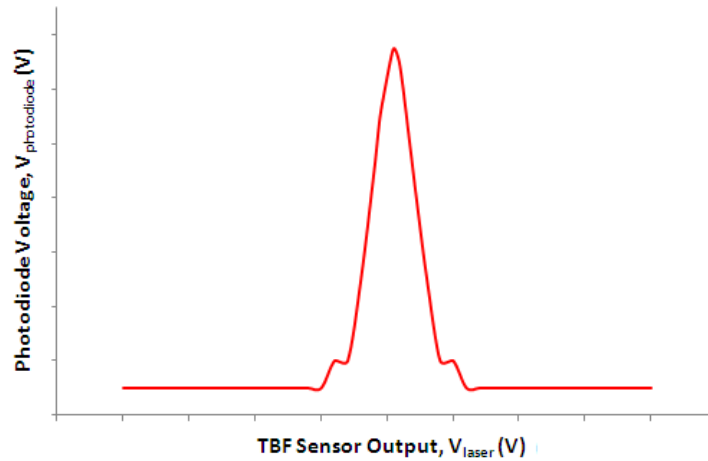


Figure 3.16:  $V_{\text{photodiode}}$  versus  $V_{\text{laser}}$

By using the model obtained from the TBF mount with relation to its central wavelength as defined by equation (3.2), we obtain the central wavelength of the FBG's reflection spectrum. This marks the success of a fully portable interrogation of an FBG.

### 3.7 Chapter Summary

The role of tunable lasers are presented accordingly as a key component for FBG interrogation, where the TLS sweep depicts the interrogation exercise using an OSA. This concept is extended further by using a photodiode to replace the OSA.

The Erbium-doped fiber tunable ring laser is chosen and elaborated. Two key components are briefed for its important details. One is the 980nm laser pump, for justification of the option, and the driver circuitry.

Next is the tunable bandpass filter (TBF) control, where crucial issues are being discussed regarding its mechanical setup and establishing a link to identify the laser's central wavelength. We arrive at a wavelength-voltage relation as the key component in interrogation.

Finally, the optic-electronic-mechanical setup is presented as per Fig. 3.14. The theoretical aspect of the interrogation of an FBG in terms of pure voltage output is shown via Fig. 3.16.

**CHAPTER 4**  
**CONSTRUCTION AND ANALYSIS OF TUNABLE RING LASER FBG**  
**INTERROGATOR**

In this chapter, we will be presenting the outcomes in terms of construction of optical circuitry, the laser pump driver construction, tunable bandpass filter (TBF) mounting methods, the spectral characteristics of the laser and finally testing the interrogator setup by scanning three test fibre Bragg gratings (FBGs).

**4.1: Tunable Ring Laser Setup**

In this section, the ring laser cavity setup, the construction of the setup itself, the spectral output produced, and its characteristics all will be discussed.

**4.1.1: Ring Laser EDFA optical circuit construction**

The next part is the construction of the ring laser cavity itself, according to the design below (recapitulated from Chapter 3 for convenience):

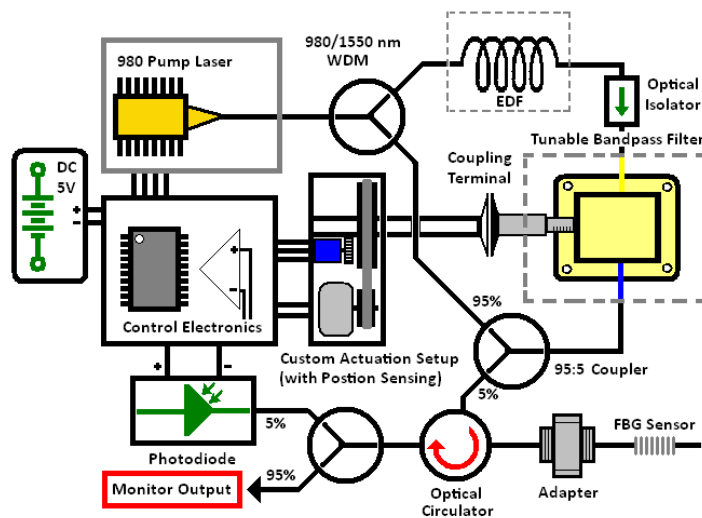


Figure 4.1: Erbium-doped fiber amplifier (EDFA) ring laser setup

The following figure shows how the design above was constructed:

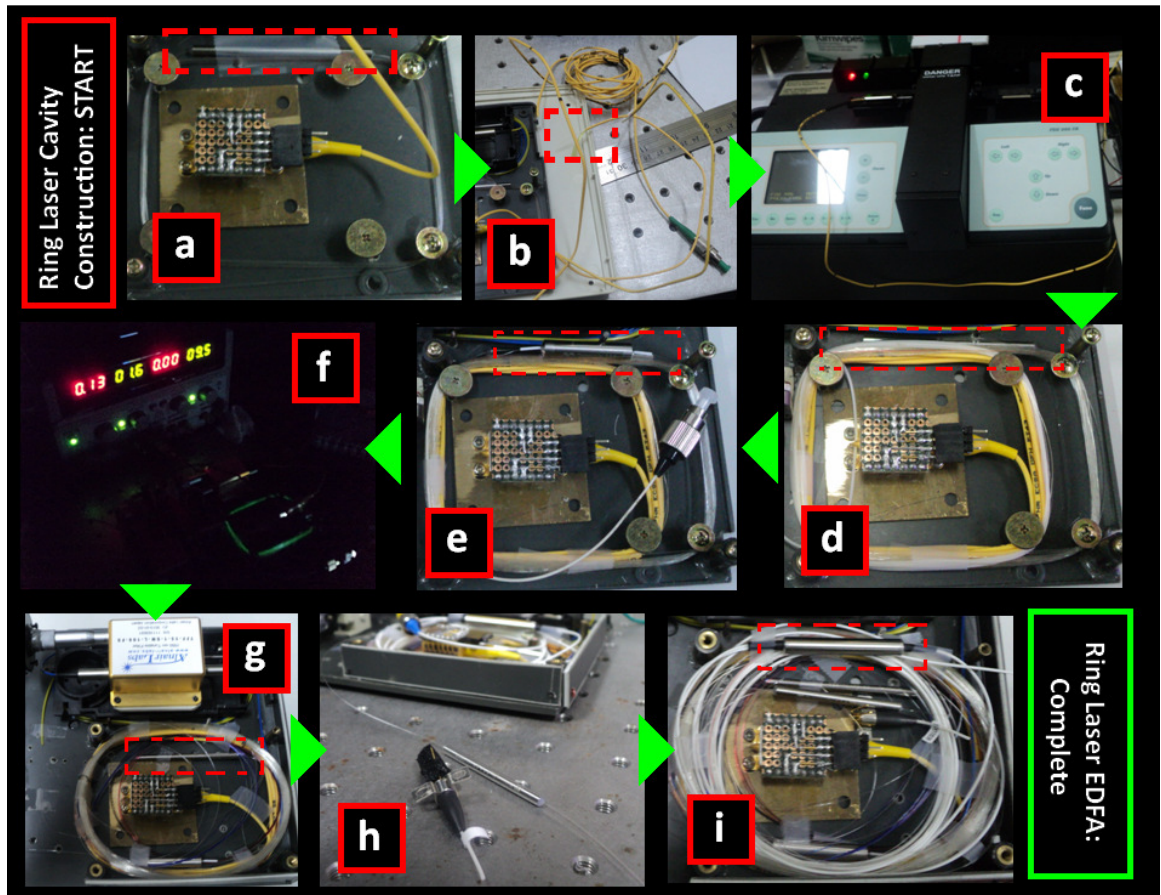


Figure 4.2: Flow of construction process of the EDFA ring laser circuitry

Fig. 4.2 is elaborated as follows (each designated box in the figure corresponds to the designated points listed below):

- a) A 980/1550 WSC is wound around the flat-top screws first, to fix the position of the casing in the center.
- b) The fiber of the 980nm laser is cut off, for splicing. Red box shows the fiber end to be stripped, cleaved and spliced.
- c) Splicing process shown, the machine used is an Ericsson's *FSU 995 FA* Fusion Splicer Machine.

- d) 20m of EDFA fiber is wound around the circuitry. Boxed component shows the 980/1550nm WSC component. 20m is chosen after various tests, which will be covered in the next result discussion.
- e) An optical isolator is incorporated later, as shown in the red box. At this stage, various EDFA lengths are used until the highest power gain is achieved via the ASE profile formed. Details of the test will be covered in the next section.
- f) A simple test to see if the laser is working without the need to use any probes; green light emanates from the cavity, which is very noticeable in the dark.
- g) A 95:5 optical coupler (boxed in red) was spliced in the cavity, and the TBF's extended fiber, which is already mounted, was spliced as well. The screws are lifted, relieving the circuit's cavity loss. The mount construction of the TBF will be presented and discussed in the following sections.
- h) An optical circulator is spliced in the circuit (not shown) and finally, the output of the circulator or the reflected end is spliced with a 50:50 coupler (component on the right). One end is spliced with a photodiode (shown in the figure, the left side), and the other is used for reference and calibration with an external probe, i.e. OSA.
- i) Figure shows the completed ring laser cavity, with the optical isolator highlighted. The spectral results will be discussed in the following sections.

The length of the EDF was configured at approximately 20m, which produced the maximum output power achievable. The discretion of configuring the optimal length of the EDF was to inspect the ASE profile formed via an OSA. The highest-powered ASE profile settles the length. However details of the formed profiles will not be discussed as optimizing the laser quality is not part of the objective.

The following results in the final view of the ring laser module:

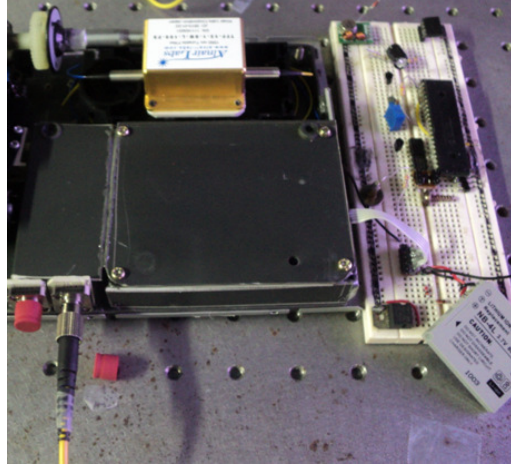


Figure 4.3: Testing Laser's Output

The casing is mounted to cover the exposed fiber, since external forces may cause the fiber to break, since spliced nodes of the fiber can easily break up. At the bottom left of the figure, the right fiber (connected to a patchcord) is the terminal for FBG connection, whereas the left adapter is for reference and calibration purposes, where the reflected spectral response of an FBG can be monitored from this terminal.

## 4.2 Control Electronics

This section discusses the electronics part which renders the FBG interrogator functional, regarding the pump laser drive, the TBF digitization and the control circuit design realization.

### 4.2.1 Pump Laser Driver

According to Fig. 4.1, a tunable laser setup starts with controlling the 980nm pump laser module. To test the functionality of the laser, a simple test was carried out without the need

for it to be mounted to a Butterfly LaserMount™, which drives the laser. The mount is generally used by researchers in the photonics field, while offering stability and simplicity, it is costly and bulky. Instead, an alternative method is by applying a voltage on the terminals (as designated in Figure 4.1) of the laser by applying the cathode (GND) terminal to pin 11 and the Anode (Vcc) to pin 10. Care is observed by setting the current at 0.11A and the voltage at 0V first (as per the datasheet's specification regarding the maximum current), and then the tuning of the voltage starts slowly until the current rises accordingly. The output of the laser can be observed by connecting the FC/APC connector end to a photodiode, which can be read using a Voltmeter or a Digital Multimeter, or an OSA, which will show the laser's high-powered spectrum in the 980nm region. The setup is shown below:

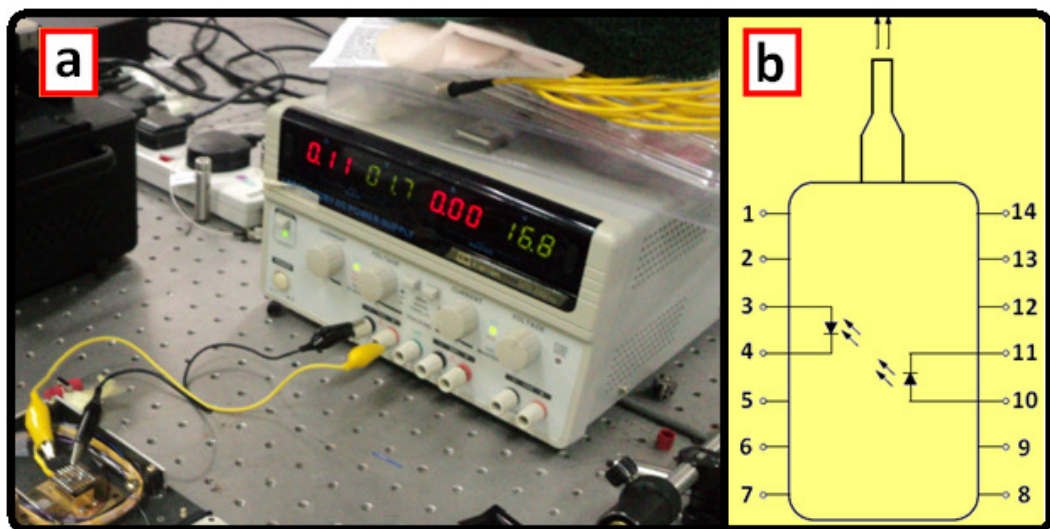


Figure 4.4: a) Pump laser testing using a variable DC supply and b) pinouts of the pump laser for testing

From the figure above, it can be seen that the laser operates at 1.7V, with current of 110mA, which is the maximum value. However, it also operates satisfactorily at 70mA. Coupling the fiber connector to a photodiode shows a maximum output of 0.514V, which is considerably high.

#### 4.2.2: 980nm pump laser control driver construction

The circuit design used for the 980nm pump laser is as discussed in Chapter 3 (Fig. 3.11), recapitulated for convenience as shown in Fig. 4.5:

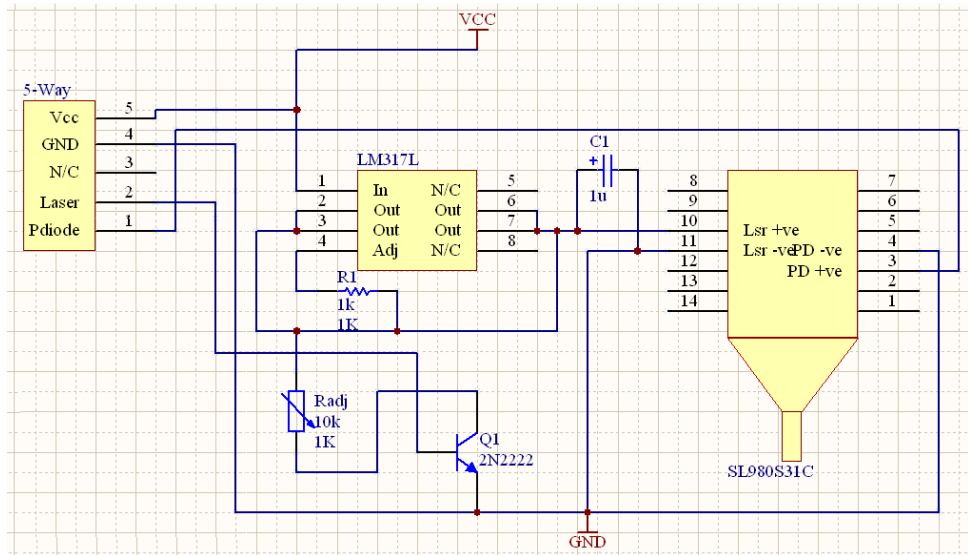


Figure 4.5: Control Circuit for SL980S31C 980 nm Pump Laser

From this step, the next phase of constructing flow process is shown in the series of pictures below:

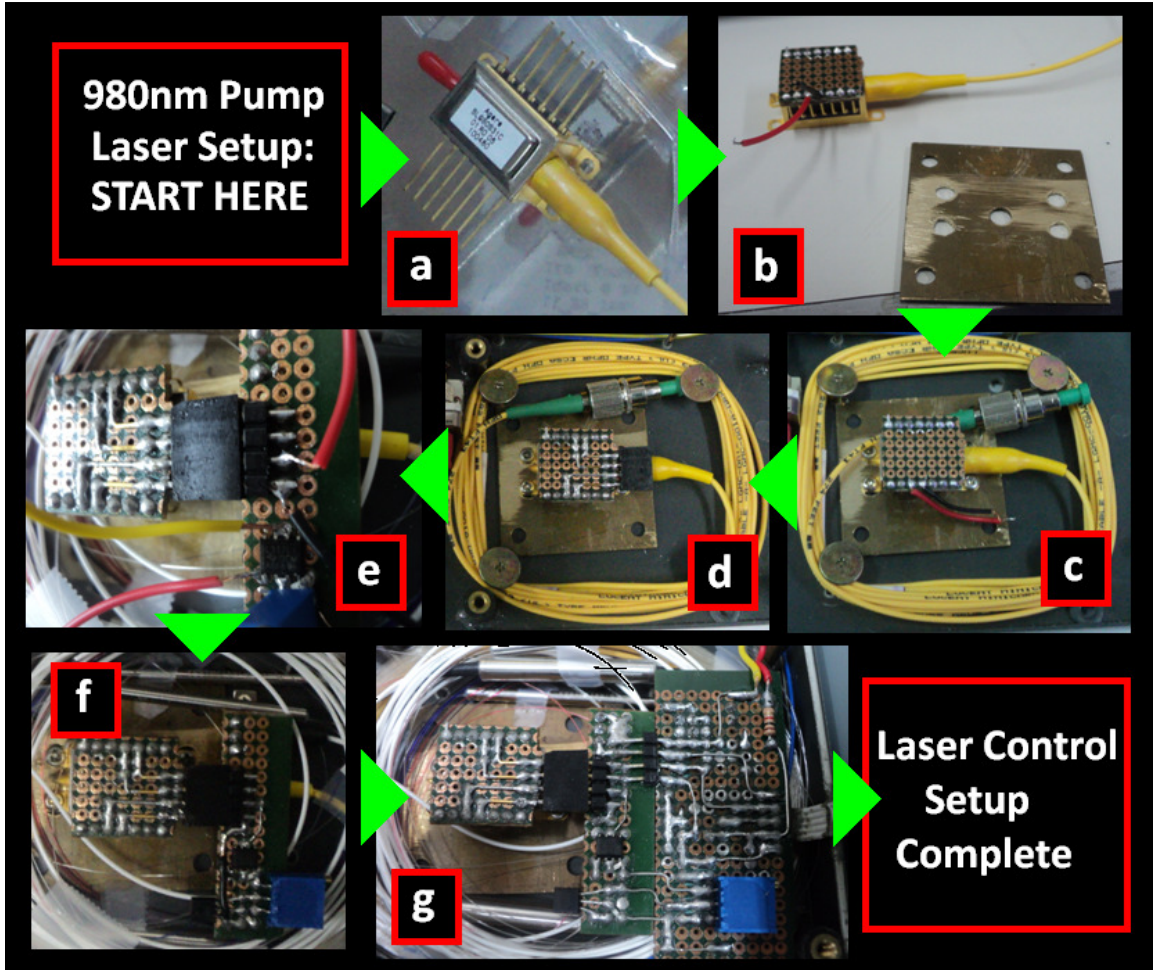


Figure 4.6: 980nm pump laser control circuit construction

Referring to the figure above, the flow is described as follows (each designated box in the figure corresponds to the designated points listed below):

- a) An unsheathed pump laser, with terminals jutting out. The terminals are 2.54mm type, therefore standard 2.54mm-spaced perfboards are suitable as a platform for soldering.

- b) The terminals are bent to face upwards; a small piece of perfboard is fitted and soldered, while a copper heat sink plate is prepared for mounting, as prescribed by the distributor of the pump laser, Agere. The heat sink aids the dissipation of the heat produced by the laser, which has a flat metal casing on either side. However, this step is only an extra precaution, since the laser operates at a very low voltage i.e. 1.3-1.7V, and heat dissipation is negligible in most cases.
- c) An ABS plastic platter is chosen as the platform to fix the position of the pump laser module. The laser fiber is wound around flat top screws to aid the compaction process. The screws are to be unscrewed later, since the right-angled fiber bending at the corners contributes to considerable cavity loss. A minimum radius of winding of 2.5cm is maintained for optimal light transmission. The heat sink mount is placed under the pump.
- d) A receptacle is added, and the connections for the four essential terminals are routed.
- e) Testing a basic regulation circuit via an LM317L IC, which was soldered on another perfboard.
- f) Completed routing the variable voltage regulation circuit via Texas Instruments' LM317L with adjusting the resistor to fix the laser at 1.7V.
- g) Completed routing all the electronics to drive the pump and to channel the output voltage from both photodiodes. Epoxy finish is cemented on the joints which may render the mechanical aspect of the cavity unstable.

This part results in a compact pump laser circuitry, which is switchable and low in power. This laser can be powered up using a single 3.7V general purpose battery, and can last a long time, since the power can be saved by switching off the power via the 2N2222 transistor.

### 4.3 Spectral Characteristics of the Laser

This section focuses on the characteristics of the laser produced from the setup discussed previously. The first part covers the tuning range and the issues covering it. This is followed by the accuracy, repeatability and the stability of the laser. A typical profile of the laser formed with an average 3dB bandwidth of 0.02nm is formed (5% output of the ring laser cavity) is shown in Fig. 4.7:

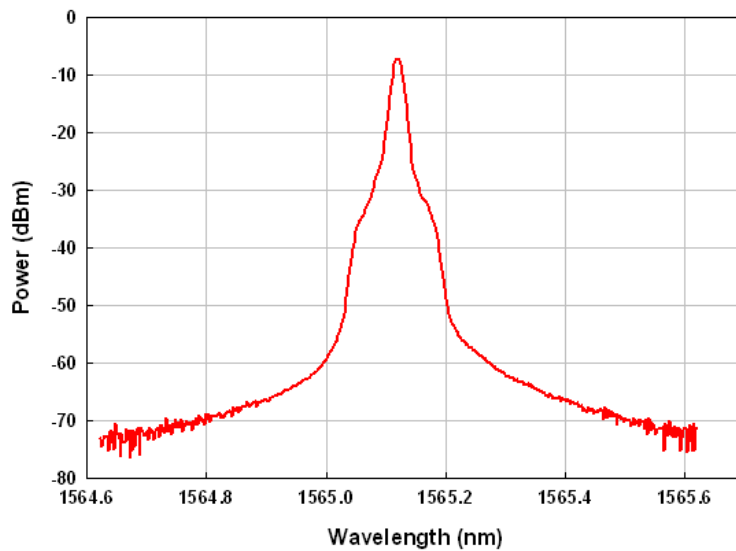


Figure 4.7: Typical laser formation at 1565.15nm

#### 4.3.1 Tuning Range

Optimization of the laser was not the primary concern; therefore presenting the profile of the laser for different EDF lengths is not presented for different tuning ranges. The following figure shows the laser's profile from the starting of the formation until the sweep is stops at the end of the spectrum.

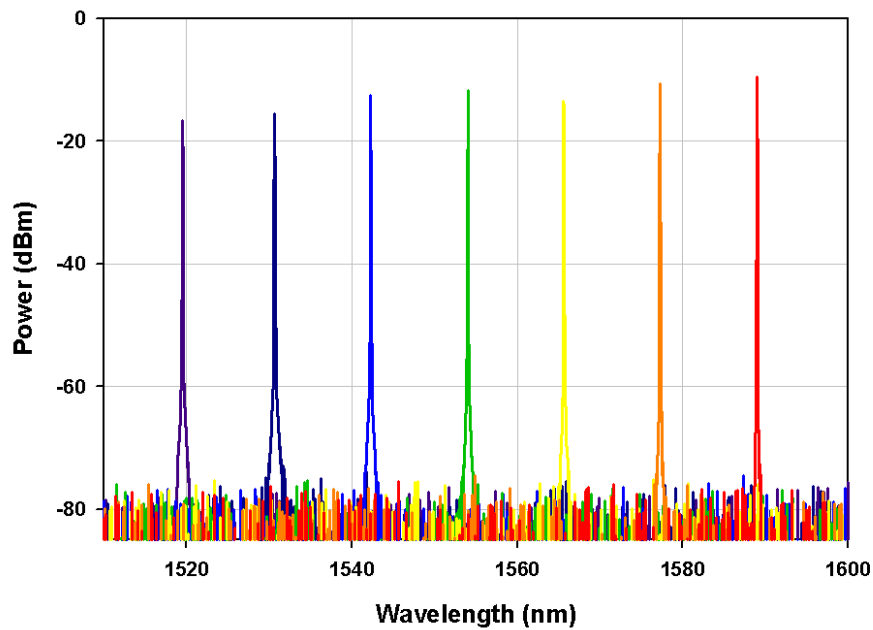


Figure 4.8: Spectral output from the initial formation until the bandwidth limit of the laser.

For this setup, an EDF length of 20m is used. The method of determining the length was to observe the ASE profile from the output of the EDFA by varying the length until the best ASE profile is produced, which exhibits the highest power profile at C-band (1530-1565). The ring cavity is completed only after this is achieved. Compared to studies by (Bellemare et al., 2001), the optimal EDF length is reported to be in the region of 15-20m, which is in agreement with the length used in our setup. The laser starts to form at around 1519nm, and stops at 1589nm, giving a tuning range of 70nm.

#### 4.3.2 Laser Wavelength Accuracy and Stability

The accuracy and stability of the laser formed are important for interrogation. This section demonstrates the reliability of the laser to be used for interrogation purposes.

**Laser Formation:** The laser starts to form at 1517.688nm, occasionally with a profile slightly different from a typical profile such as shown in Fig. 4.7:

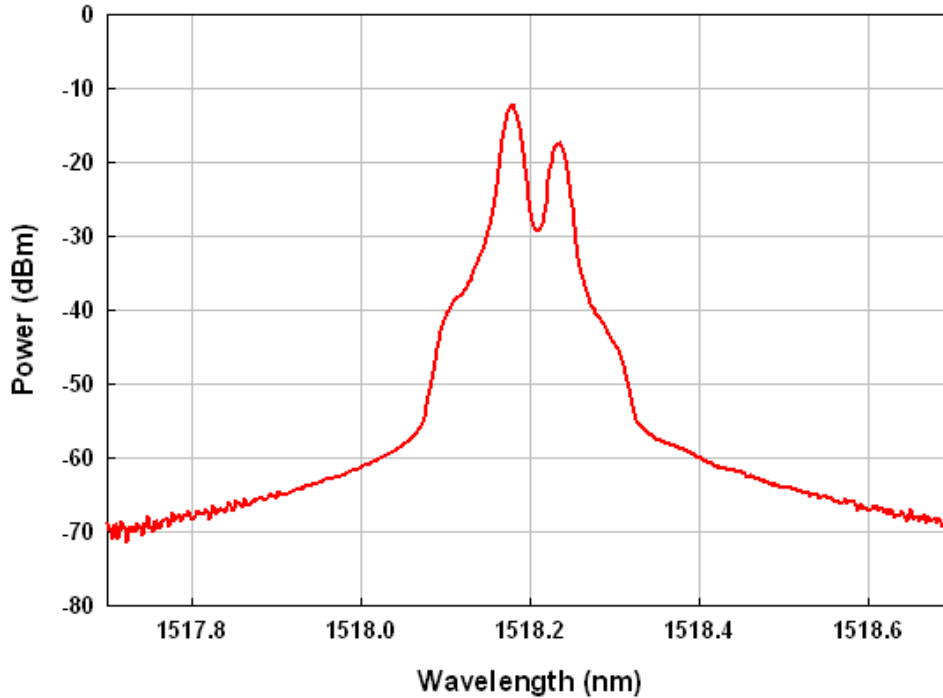


Figure 4.9: Initial laser formation at 1517.688nm

Occasionally, the laser exhibits two peaks, one at 1517.688nm at the highest power, and 1518.234nm at the other peak. This is due to the resolution of the filter, which changes with periodicity for each consecutive wavelength. At the wavelength shown above, the formation of a dual peak laser takes place due to this instability. However, this is negligible for interrogation purposes due to its rarity.

However, once the laser starts to form, it can be tuned back towards 1514nm before collapsing. This gives an extra 3nm, which is insignificant for our application. At other times, its form will be normally as shown in Fig. 4.6.

**Accuracy and stability:** The formation of a laser gives in to the tendency to drift in terms of the central wavelength and its peak power. The bandwidth is divided into sixteen sections, and the stability of each sample section laser is examined within one hour, with 5-minute intervals. The following sections discuss the formation of the laser, stability of two parameters within the period, which are the wavelength and the peak power. (Refer to Appendix C). All fine measurements of the wavelength and optical power are computed using the OSA, with a maximum resolution of 0.05nm.

The chosen bandwidth's stability can best be represented by the figure below:

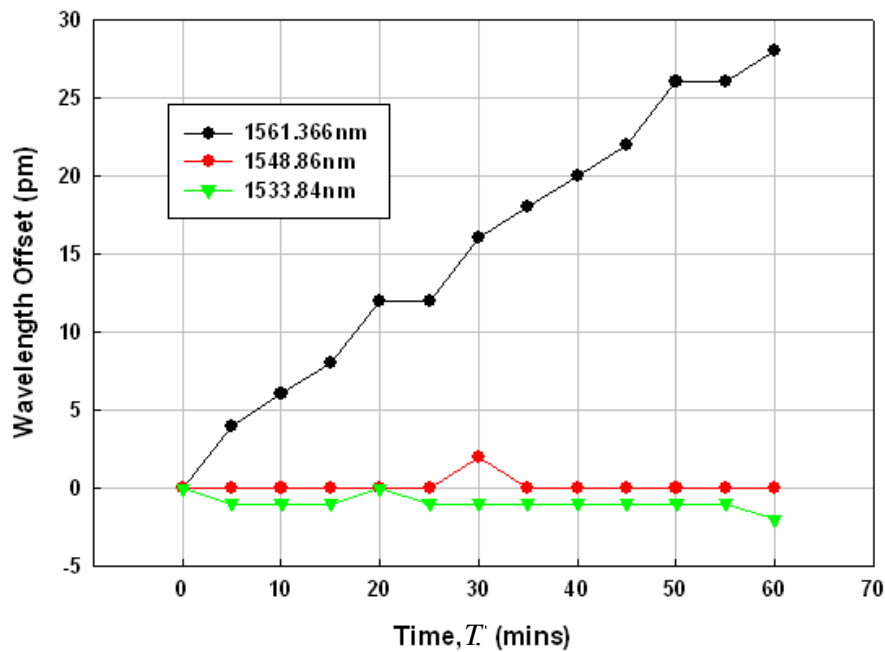


Figure 4.10: Wavelength stability along the spectrum (1518-1589nm)

Only three sample wavelengths are shown in Fig. 4.10, where the best, typical and worst drift occurred at 1524.024, 1518.178 and 1528.296nm respectively. As shown above, the drift of the laser's central wavelength varies at different wavelengths. A maximum of 28pm drift was observed at 1558.336nm, and the most stable one was at 1544.13nm with zero

drift. However, for our interrogation purposes, the drift of the wavelength within one hour is not significant; therefore the laser can still function as a component for FBG interrogation.

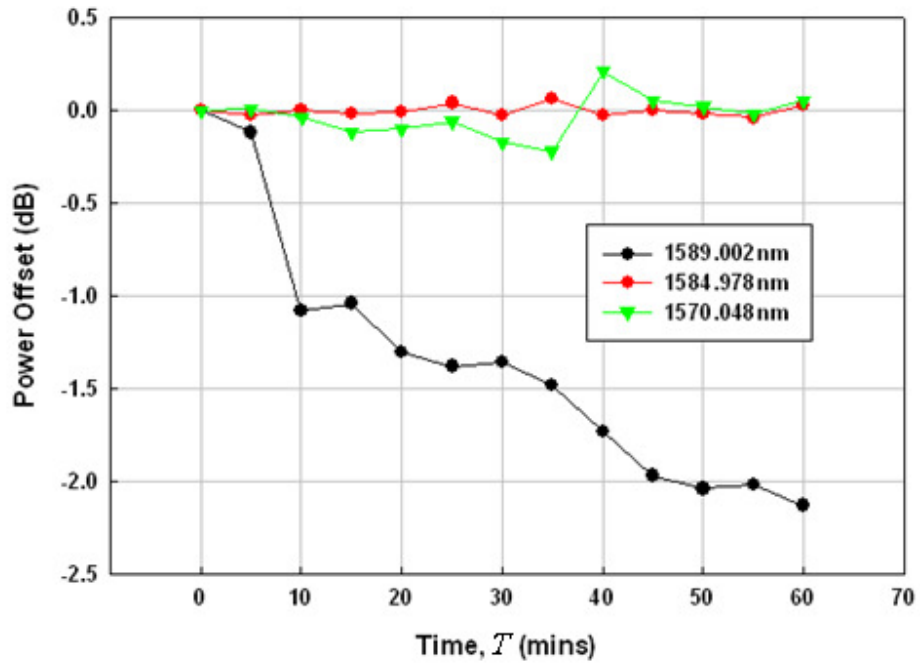


Figure 4.11: Power stability along the spectrum (1518-1589nm)

Only three curves are shown in Fig. 4.11, where the best, typical and worst drift occurred at 1584.978, 1579.048 and 1589.002nm respectively. The power drift at most wavelengths are relatively stable, where the majority drifts at  $\pm 0.5$  dB, except around 1524nm and 1589nm, where a maximum drift of -1.3 and -2.2dB can be observed, respectively. However, these regions also will not affect the interrogation, as will be shown in the following sections.

#### 4.4: TBF Actuator Mount Construction

In this section, the design is constructed as discussed in Chapter 3, Fig. 3.8. A Computer-Aided Design (CAD) fabrication of the actuation drive is not considered for the sake of simplicity, where in this section, the construction commenced by using recyclable DVD

drives, which is low in cost, and can be constructed effectively, efficiently and demonstrates the concept sufficiently.

#### 4.4.1: Assembly of the TBF Actuator

The following elaborates the optical/electrical characteristics of the mount:

An Alnair Photonics' tunable bandpass filter, and the corresponding design (recapitulated for convenience) are as shown below:

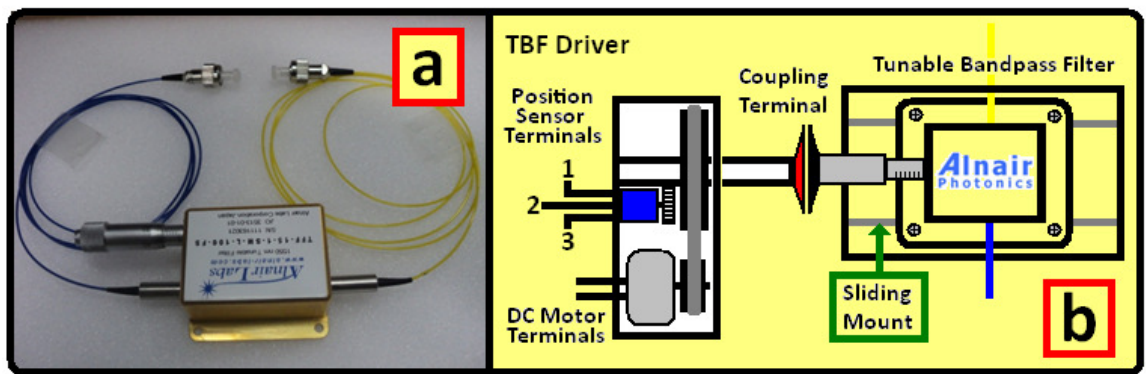


Figure 4.12: a) A manually tunable bandpass filter b) A TBF mount design

From the design above, a 10kΩ potentiometer acts as a position sensor and a voltage divider. With reference to Fig. 4.12(b), when the sensor is turned with the tuning of the TBF, while assigning 5V to terminal 1 and 0V to terminal 3, the resistance across terminals 1 and 2, or 2 and 3 changes. It obeys the voltage division rule as shown by Eq. 4.1:

$$V_{out} = V_2 = \frac{R_{1,2}}{R_{pot}} \times V_{ref}, [0.1V_{ref} \leq V_{out} \leq 0.9V_{ref}] \quad (4.1)$$

While  $R_{1,2}$  is the resistance between terminals 1 and 2,  $V_{ref}$  as the reference voltage, is set at 5V, and  $R_{pot}$  as the potentiometer's full resistance is 10k $\Omega$  for this case. The change of the output voltage is linear with the tuning degree.  $V_{out}$  is limited to a minimum of 10% of the  $V_{ref}$ , and maximum at 90%  $V_{ref}$ . The setup included the rail voltage of the sensor into consideration, since tuning the positioning can only take place in a limited number of revolutions. Therefore, when this limit is transgressed, the position of the bandwidth will shift according to the excess tuning beyond the range. Therefore the starting output voltage was preset at 0.5V and ends at 4.5V, with a reference to 5V-0V rail.

The following figure shows the flow of construction of the mount itself:

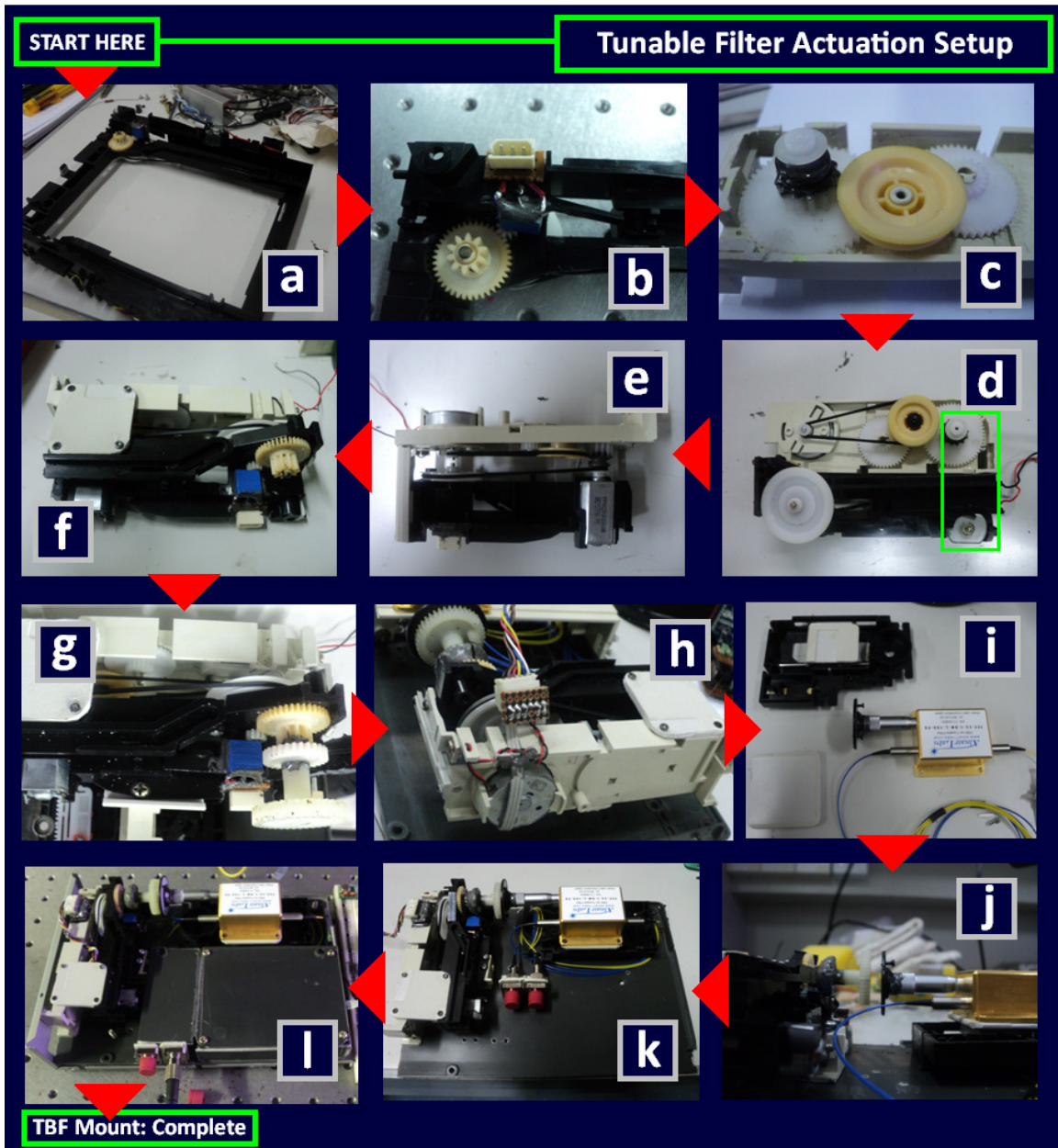


Figure 4.13: Tunable bandpass filter (TBF) digitization mount for ring laser tunability

The figure above is elaborated as follows (each designated box in the figure corresponds to the designated points listed below):

- a) A DC motor with a geared output (Drive A) is prepared before assembly which acts as the main actuation drive.

- b) A highly precise potentiometer (Model: **Baoter 3296**) is placed to fit the tuning knob into one of the open-ended gears which couples the resistance of the potentiometer matched to the position of the TBF tuning. The potentiometer is cemented into its position using epoxy finish.
- c) Another DC motor drive (Drive B) is prepared to be cascaded with Drive A; an epoxy finish is used to fixate the plastic coupler of Drive A and the output shaft of Drive B.
- d) Moments before cascading both the drives, the green box shows the fitting to be made between the shaft and the plastic shaft coupler.
- e) Coupled together, which results in a relatively high torque actuator
- f) Plastic joints added to the actuation drive for stability
- g) The output shaft is extended by adding another plastic coupler to be matched with the TBF's shaft,
- h) Combining all the terminals of the TBF driver (three terminals for the positioning sensor, and two terminals of the DC motor) into one common receptacle for ease in plugging and unplugging the socket.
- i) Preparing to fix the TBF on a sliding mount. The tuning knob of the TBF is fixed with a plastic plate for ease in coupling with the actuation shaft of the TBF driver.
- j) Matching the height between the TBF and the output shaft of the TBF driver; this was achieved by precisely tweaking the minute changes of position using screws on the sides of the TBF driver.
- k) Successful coupling of the TBF and the TBF driver
- l) Finally, combining this section and the process obtained in Fig. 4.4, we arrive at the nearly-complete optical-mechanical setup of the tunable laser.

#### 4.4.2: Modeling of the TBF Mount

In this section, the conversion of the wavelength of the laser into voltage is demonstrated, which renders the interrogator controllable via electronic drives.

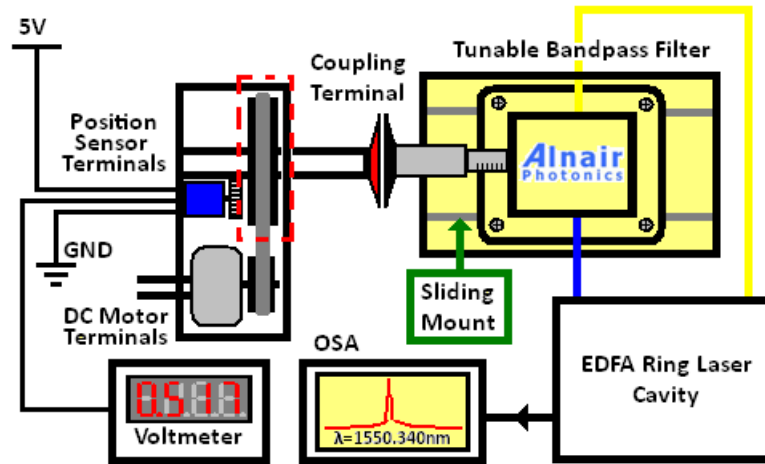


Figure 4.14: Setup to model the TBF mount

The setup in Fig. 4.14 shows two values are monitored; the voltage output of the position sensor and the central wavelength of the laser via OSA. The TBF is manually tuned via the exposed gear (highlighted in the red box). The center wavelength of the laser tuned via the TBF,  $\lambda_{\text{laser}}$  is plotted against the ratio of the output voltage of the positioning sensor,  $V_{\text{out}}$  as shown in Fig. 4.15 (refer Appendix B):

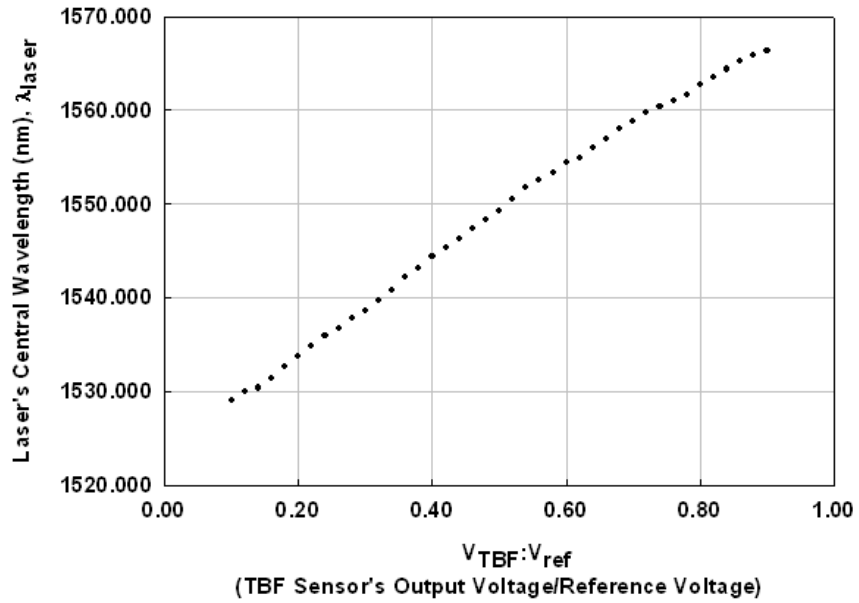


Figure 4.15: Laser's central wavelength,  $\lambda_{TBF}$  vs  $V_{TBF}:V_{ref}$  plot

For convenience, the wavelength versus the ratio of the sensor's output and the reference voltage is plotted. This will result in a model which can be used for any value of the reference voltage,  $V_{ref}$ . In this case, the output voltage ranges from 0.5 to 4.5V, with normalization by dividing the all the values with 5V.

From the figure, although the linearity of the system is evident, a linear function gives rise to errors up 2.0nm, since it's not perfectly linear. This error is unacceptable for interrogation purposes. By sampling a few available functions, it is found that a sigmoidal function fits the curve optimally, as stated in Eqn. 4.2:

$$f(x) = \frac{a}{1 + e^{-\left(\frac{x-x_0}{b}\right)}} \quad (4.2)$$

By utilizing this function, a curve fitting exercise shows the best approximation as shown below:

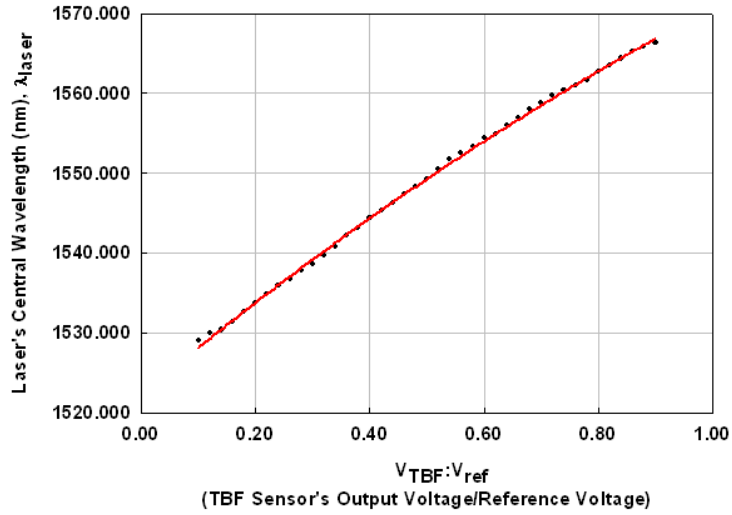


Figure 4.16: Laser's central wavelength,  $\lambda_{TBF}$  vs  $V_{TBF}:V_{ref}$  curve-fitting plot

And by utilizing Sigmaplot's iterations, we arrive to the values as shown below:

$$\lambda_{laser} = \frac{1646.5526}{1 + e^{-\left(\frac{V_{out} + 4.7596}{1.8999}\right)}} \text{ nm} \quad (4.3)$$

Finally, we simplify the model above as:

$$\lambda_{laser} = \frac{1646.5526}{1 + e^{-\left(0.5263 \frac{V_{out}}{V_{ref}} + 2.505\right)}} \text{ nm} \quad (4.4)$$

A quick test can be carried out to determine the model's accuracy. Taking nine samples across the bandwidth from the actual test results (Refer Appendix A), we can estimate the accuracy of the model by testing each value as shown in Table 4.1:

Table 4.1: Error Calculation of the wavelength between the TBF actuation model and the laser's central wavelength read from the OSA

$V_{out}(V)$	$\lambda_{actual}(nm)$	$\lambda_{laser} = \frac{1646.5526}{1 + e^{-\left(0.5263 \frac{V_{out}}{V_{ref}} + 2.505\right)}} \text{ nm}$	$E = \left  \frac{\lambda_{actual} - \lambda_{model}}{\lambda_{actual}} \right  \times 100\%$
0.5	1529.044	1528.131	0.05971
1.0	1533.718	1533.787	0.00449
1.5	1538.648	1539.191	0.03529
2.0	1544.426	1544.354	0.00466
2.5	1549.270	1549.284	0.00090
3.0	1554.374	1553.990	0.02470
3.5	1558.818	1558.482	0.02155
4.0	1562.678	1562.767	0.00570
4.5	1566.386	1566.855	0.02994

The average error,  $E$  is  $(0.18694/9) = 0.0207\%$ , in which the amount has a moderate level in accuracy. The system also achieved a tunable range of 38 nm (in this setup the range was 1529-1566nm, but this range can be shifted within desired bandwidths within 1520-1580nm), which is comparably high for a lot of applications.

However, the tuning speed across the bandwidth (from the actuation of the motor drive) is more than 5 seconds driven at 3V. This is not a problem for a single-sweep, or slow-interval scanning, but it will not be applicable for real-time scanning. The nonlinearity in some regions of the graph is due to the resolution (maximum only up to 0.001V within the range of 0-5V) and accuracy of the instrument used to read the voltage, which is an off the shelf digital multimeter (Model: Lutron DM-9960); a high resolution voltmeter is not available at our disposal. This gives rise to the inaccuracy as depicted in Table 4.1.

#### 4.5: Test Interrogation of FBGs

This section finalizes the objective of this work, which is to demonstrate interrogation of FBGs in different conditions, and compare the computations with a standard interrogation exercise as per Figure 3.1, where an ASE light source, an optical circulator and an OSA is used to interrogate an FBG. The setup for test interrogation is as shown in Fig. 4.17:

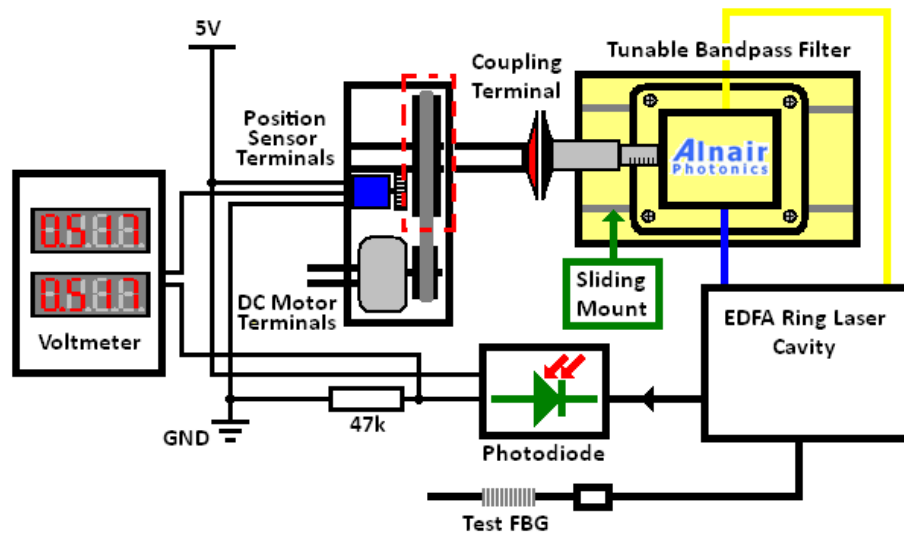


Figure 4.17: Test interrogation setup

The interrogation takes place by observing two parameters. The first is the TBF position value, which is the output voltage of the positioning sensor. The sweep along the bandwidth is performed by manually tuning the exposed side of the gear (indicated in the red box in Fig. 4.16) which in turn finely rotates the TBF's knob and the TBF sensor as well i.e. the potentiometer. This will vary the voltage output for identifying the central laser wavelength, denoted as  $V_{\text{laser}}$ , or the TBF sensor output.

The second will be the photodiode's response, in terms of voltage, as discussed in Section 3.5. A common reference supply of 5V is used for the photodiode circuit, and the potentiometer is adjusted to a value of around 5k $\Omega$ . The change of the output power of the reflection spectrum is denoted in terms of voltage,  $V_{photodiode}$ , or the photodiode response output.

The interrogation setup is shown in Fig. 4.18:

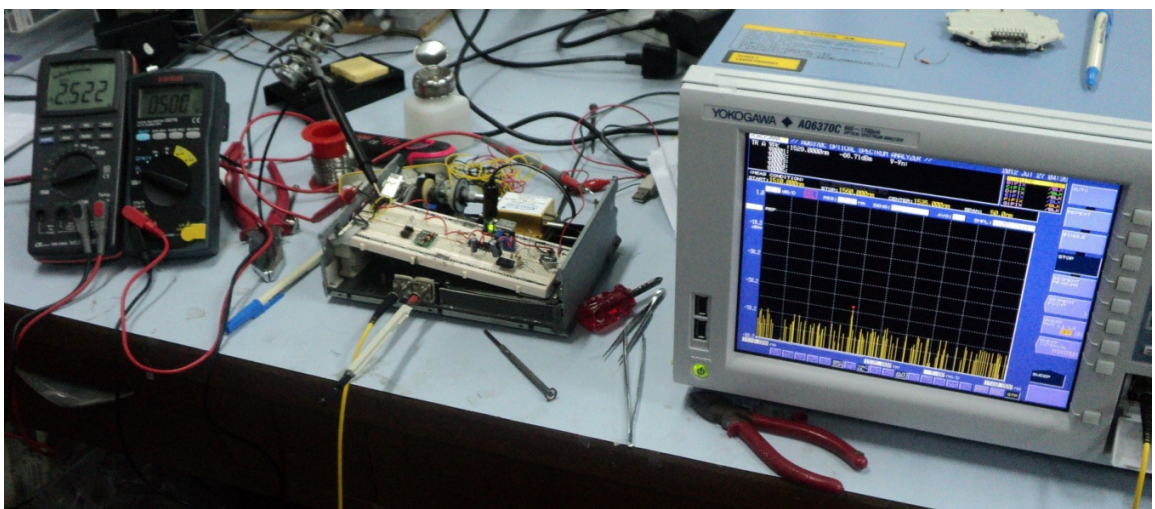


Figure 4.18: FBG Interrogation Setup Scene

Two digital multimeters (DMMs) are used. The one on the left is photodiode response voltage output, and on the right depicts the wavelength in terms of voltage. The TBF is tuned manually for demonstration purposes. 5% of the reflection spectrum is channeled to the OSA for monitoring purposes.

### 4.5.1: Null Test

An output profile of the photodiode response is shown by not inserting anything into the input channel of the interrogator. The objective is to test the interrogator's response without any FBG, and to determine whether there are any deformations along the bandwidth which may affect the flatness of the output. As shown in Fig. 4.19:

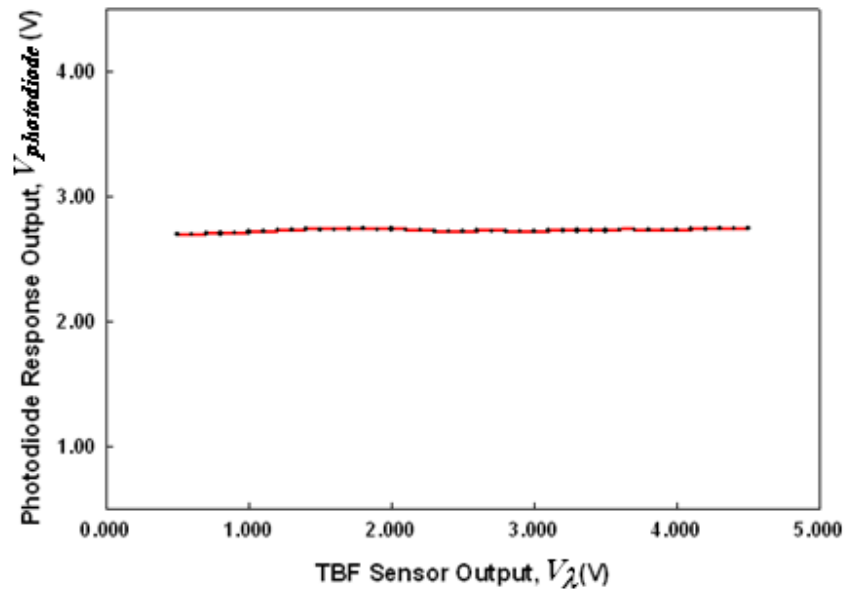


Figure 4.19: A typical null test.

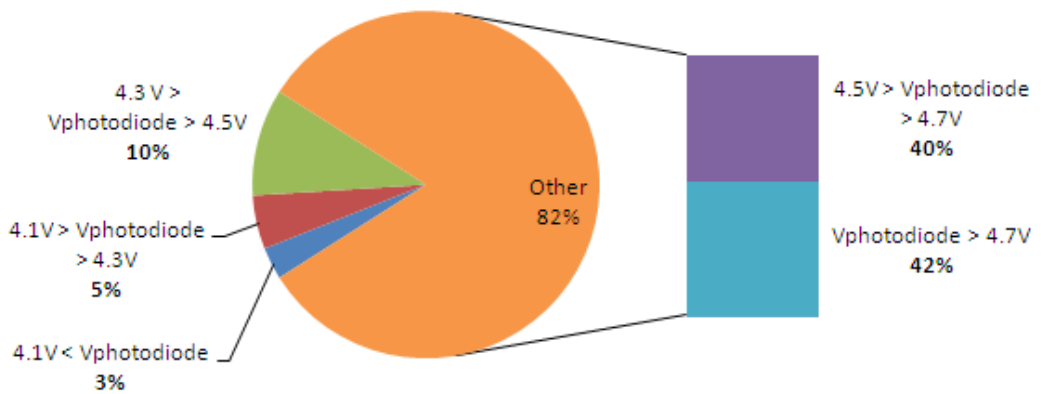


Figure 4.20: Pie chart shows the frequency of the appearance a base voltage makes.

Fig. 4.20 shows the photodiode's response with different base voltages, where this can be observed when the laser driver is turned off and on consecutively. The different base voltages gives rise to a different interrogation amplitude as will be discussed in Section 4.5.2. However, this will not affect the interrogation procedure, as the amplitude will still change when the reflected spectral profile is detected, which still returns a peak shape.

This occurrence is due to current-optical relation of the photodiode. A fluctuation between 0.3-0.6dB of the laser's peak can be observed via the OSA (as shown in Fig. 4.11) against time, which is true for consecutive switching of the laser as well. While this change is not significant in OSA, a photodiode responds differently, as shown by the current-optical power curve of the photodiode as shown below:

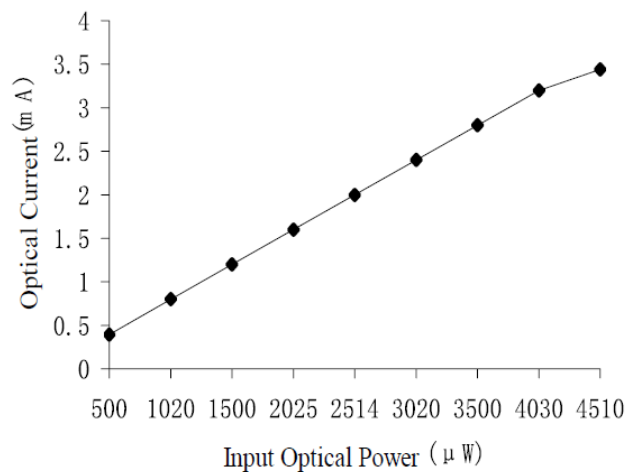


Figure 4.21: Current-optical power curve. (Photonics, n/a)

At -7dBm, the response is out of the region of the photodiode's exhibited response, although there will still be an output to be observed. A typical value of the laser's output power is  $\approx 200 \mu\text{W}$ , and the output current is  $\approx 0.1\text{mA}$ . The value of the resistor coupled to the photodiode is  $45\text{k}\Omega$ . By the relation  $V=IR$ , the output voltage is  $4.5\text{V}$ .

However, at -7.3dBm, or  $\approx 186 \mu\text{W}$ , the output current is less predictable, assuming that it is 0.08mA. Therefore the output voltage is 3.645V. Here, a shift of 0.855V can be observed for a change of 0.3dB in the system.

Fig. 4.20 shows the statistical chance of the appearance of each base voltage under consecutive switching of the laser. Ideally, a base of 4.3-4.5V (with a 10% chance of occurrence) is adequate for interrogation purposes. The rise of the photodiode's voltage response when it detects the reflection spectrum normally goes near to 4.7-4.8V, which is just below the 5V rail. The desired base voltage can be obtained by continually turning the laser on and off, and poll for the desired range of values. This is a trivial task of control for microcontrollers.

However, a practically flat output is observed when no FBG is connected to the interrogator, for all values of the base voltage. The maximum value of the voltage change is only 0.044V (refer Appendix), which is negligible since when the reflection spectrum coincides with the laser's central wavelength, the change will be significant enough to represent the peak of the spectral profile.

#### **4.5.2 Testing FBGs**

In this test, three sample FBGs are tested thoroughly using an Optical Spectrum Analyzer (OSA) within two conditions. One is a null test, where the FBG is not subjected to any external strain, and the other is a strain test, where external strain is applied, as shown in Fig. 4.22:

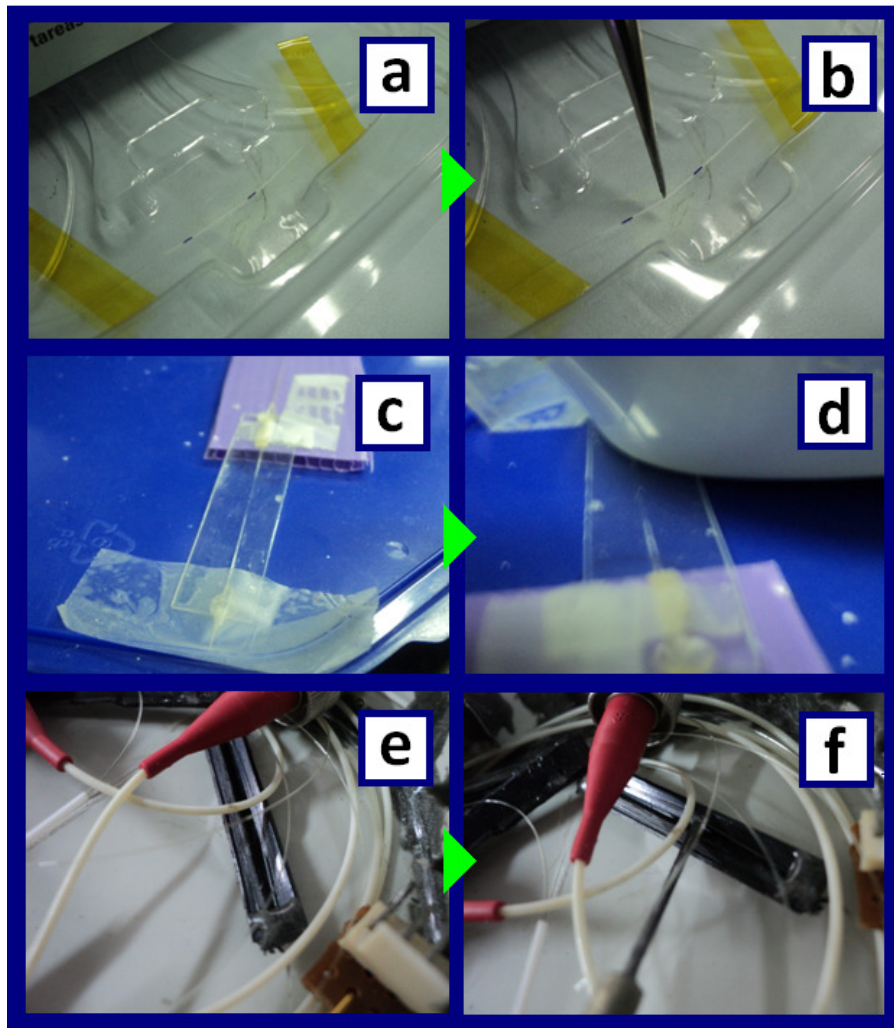


Figure 4.22: Testing FBGs for two different conditions; (a) and (b) is FBG1, (c) and (d) is FBG2, (e) and (f) is FBG3

In the following, the spectral response of the FBGs in both conditions as shown above will be presented. Consequently, the interrogation response also will be revealed, showing the correlation between conventional interrogation and this work's findings.

#### 4.5.2.1 FBG1 Tests

The following shows the reflection spectrum of FBG1 versus the interrogation profile:

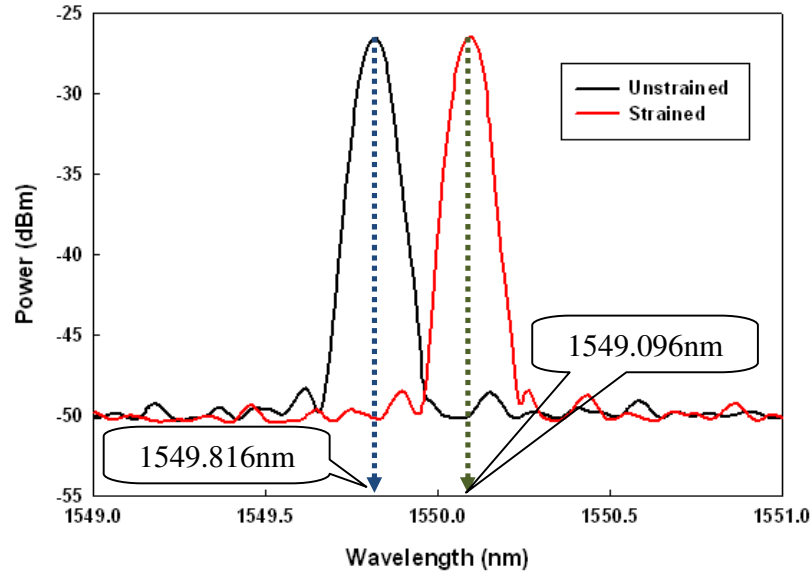


Figure 4.23: FBG1 reflection spectrum via OSA

Fig. 4.23 above conforms to the unstrained and strained condition as shown in Fig. 4.22 (a) and (b). The central wavelength of the reflection spectrum of the unstrained FBG1 is 1549.816nm (black line) and 1550.096nm for the strained one (red line). The shift of the wavelength is 0.484nm.

For our interrogation scheme, the average value of the photodiode's response output is plotted against the TBF sensor output. The following shows the photodiode response versus the TBF sensor output, as a product of this work's test interrogation:

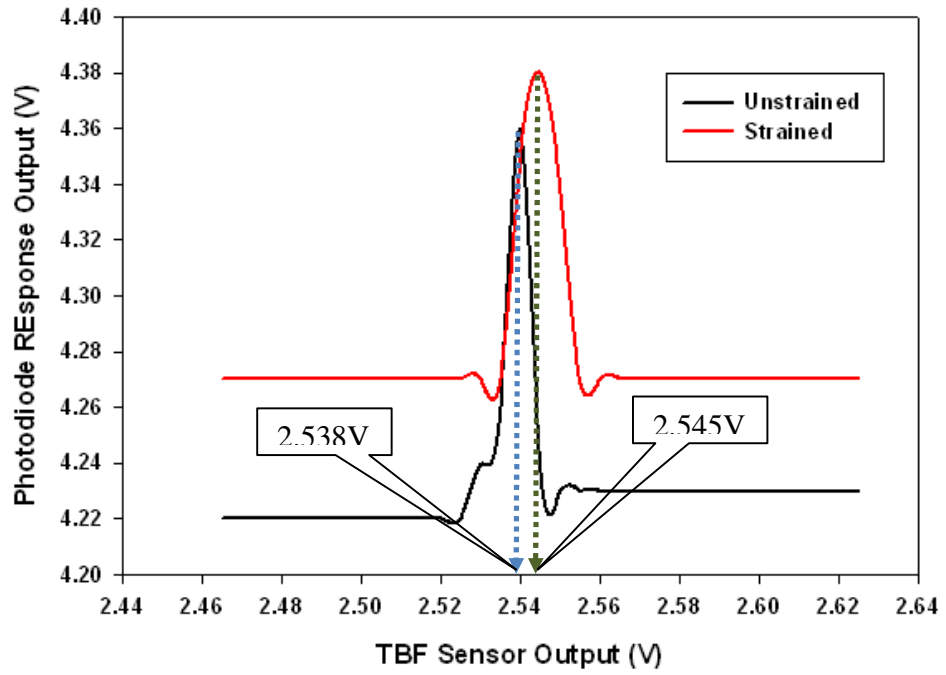


Figure 4.24: FBG1 interrogation spectrum in terms of Volts (V)

As shown in Fig. 4.24 above, the peak power exhibited by the unstrained spectrum is considerably lower due to changing base voltages (the value of the output when there is no reflected power) of each set of the interrogation itself. However, this does not affect the interrogation since the central wavelength is the main concern, which can be calculated from Eqn. 4.4:

$$\lambda_{laser} = \frac{1646.5526}{1 + e^{-\left(0.5263 \frac{V_{out}}{V_{ref}} + 2.505\right)}} \text{ nm}$$

The output voltage at the peak for the unstrained and strained FBG's response is 2.540V and 2.560V. Therefore:

$$\lambda_{FBG1(unstrained)} = \frac{1646.5526}{1 + e^{-\left(0.5263 \frac{2.540V}{5V} + 2.505\right)}} \text{ nm} = 1549.656 \text{ nm}$$

$$\lambda_{FBG1(\text{unstrained})} = \frac{1646.5526}{1 + e^{-\left(0.5263 \frac{2.56}{5V} + 2.505\right)}} \text{ nm} = 1549.723 \text{ nm}$$

The errors of the readings for unstrained and strained FBG1 are 0.160nm and 0.373nm respectively. The calculated shift is 0.067nm compared to 0.280nm as obtained from the values from OSA.

#### 4.5.2.1 FBG2 Test

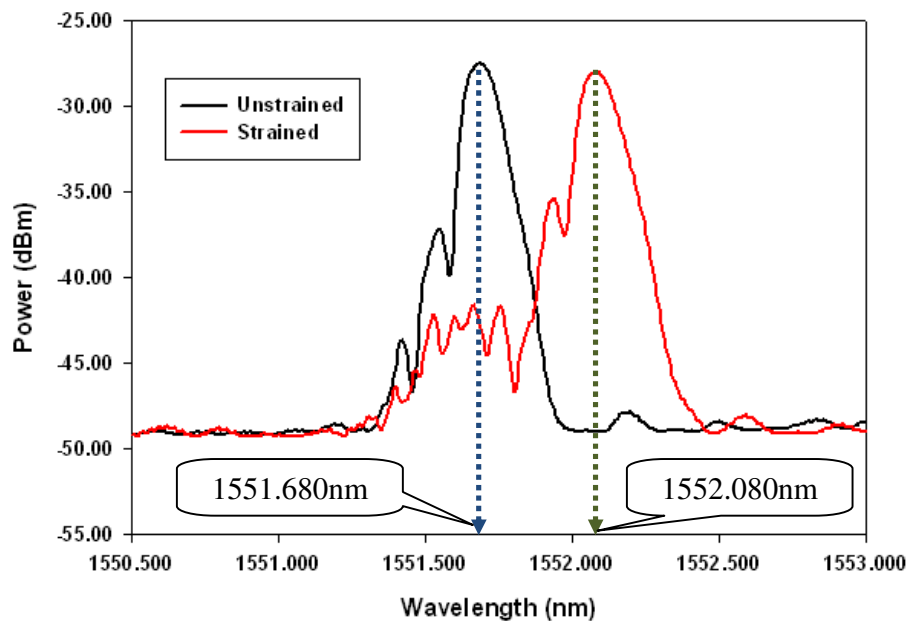


Figure 4.25: FBG2 reflection spectrum via OSA

Fig. 4.25 shows the profile of the unstrained FBG2 is much less uniform than a standard FBG reflection spectrum, which shows a Gaussian form. The unstrained and strained FBG reflection spectrum's central wavelength is 1551.680nm and 1552.080nm, as obtained from the OSA. The shift amounts to 0.400nm. The strained FBG2 shows a slightly different profile amid the wavelength shift. The interrogation profile of this FBG is shown as follows:

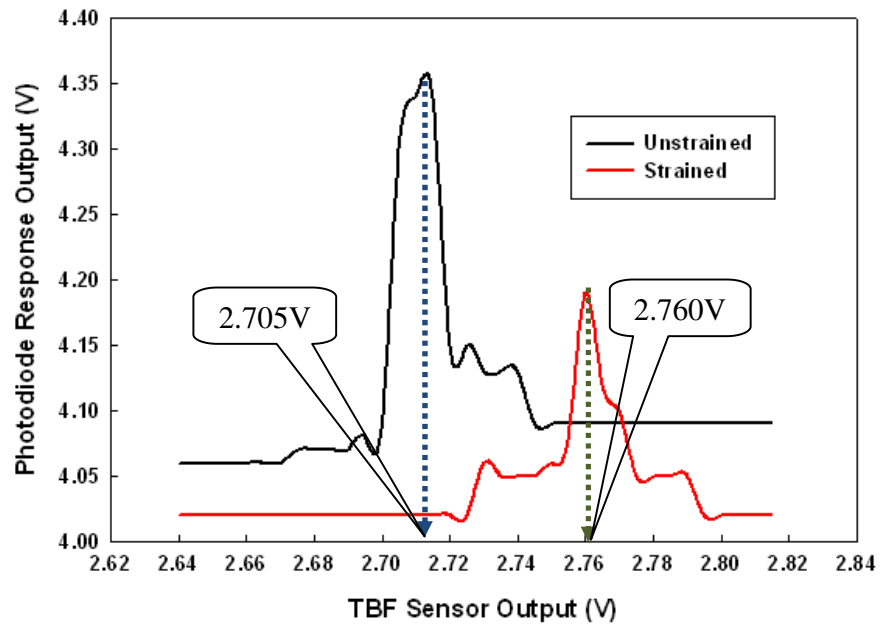


Figure 4.26: FBG2 interrogation spectrum in terms of Volts (V)

From Fig. 4.26 above, the shift profile is quite similar as obtained from the interrogation exercise. The peak of the profiles of unstrained and strained occurs at 2.705V and 2.760V respectively. We can calculate the central wavelength of the reflected spectrum as follows:

$$\lambda_{FBG2(unstrained)} = \frac{1646.5526}{1 + e^{-\left(0.5263 \frac{2.710}{5V} + 2.505\right)}} \text{ nm} = 1551.313 \text{ nm}$$

$$\lambda_{FBG2(strained)} = \frac{1646.5526}{1 + e^{-\left(0.5263 \frac{2.760}{5V} + 2.505\right)}} \text{ nm} = 1551.784 \text{ nm}$$

The error of  $\lambda_{FBG2(unstrained)}$  and  $\lambda_{FBG2(strained)}$  are 0.367nm and 0.296nm respectively. This interrogation gave a relatively high precision in our calculations. A shift of 0.471nm was obtained, which is close in value to the shift of 0.400nm as obtained previously.

#### 4.5.2.1 FBG3 Test

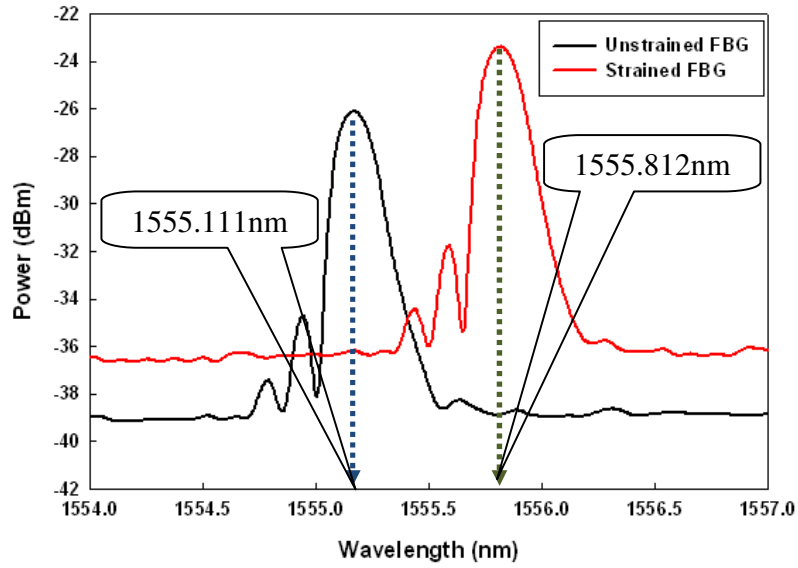


Figure 4.27: FBG3 reflection spectrum via OSA

Figure 4.27 shows the reflection spectrum of FBG3 with the central wavelength of 1555.11nm and 1555.812nm for the unstrained and strained FBG3 respectively, with 0.702nm shift. This profile is shadowed by the interrogation profile obtained as follows:

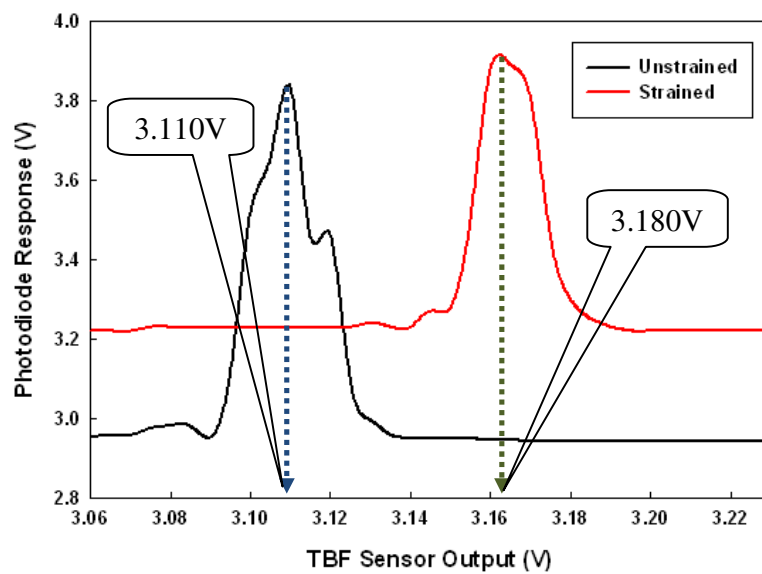


Figure 4.28: FBG3 interrogation spectrum in terms of Volts (V)

The peaks of the unstrained and strained FBG3 are valued at 3.110V and 3.180V respectively, giving the central wavelengths of the reflection spectrum as:

$$\lambda_{FBG3(unstrained)} = \frac{1646.5526}{1 + e^{-\left(0.5263 \frac{3.11}{5V} + 2.505\right)}} \text{ nm} = 1555.022 \text{ nm}$$

$$\lambda_{FBG3(strained)} = \frac{1646.5526}{1 + e^{-\left(0.5263 \frac{3.18}{5V} + 2.505\right)}} \text{ nm} = 1555.657 \text{ nm}$$

The error of  $\lambda_{FBG3(unstrained)}$  and  $\lambda_{FBG3(strained)}$  are 0.090nm and 0.155nm respectively, and the shift is 0.635 as opposed to the 0.702nm obtained previously.

#### 4.6 Chapter Summary

In this chapter, we have reported the success of construction of the ring laser cavity within a compact space, as per the setup in Fig. 4.1. This started off with demonstrating the drive circuit for the 980nm pump laser, where the functionality was proven. The tunability of the laser is 70nm, with 20m length of EDF for the laser cavity. The spectral profile of the laser formed in our setup was presented, where the power and wavelength drift of the laser is shown within an hour with 5-minute intervals. The setup further advances to establishing a wavelength-voltage relation via the construction of the TBF mount, where a model was derived for the mount as per Eq. 4.3. This enables us to identify and match the voltage of the output sensor of the positioning sensor for interrogation. Finally, interrogation was carried out for three test FBGs with reasonable accuracy. There were shortcomings due to limitations of the apparatus used for our setup, which can be addressed with more specific troubleshooting.

## CHAPTER 5

### CONCLUSIONS

This chapter summarizes the analyses of all results in the previous chapter, where we start with the laser's driver, the profile of the formation of the laser, the TBF mount, the photodiode's response, and finally the interrogation exercise itself.

#### 5.1: Laser Driver

As discussed in previous chapters, the design of the 980nm pump lasers driver circuit (Fig. 3.11) worked as intended, without the need to monitor the internal photodiode. The diagram for the laser driver can be summarized as shown in Fig. 5.1:

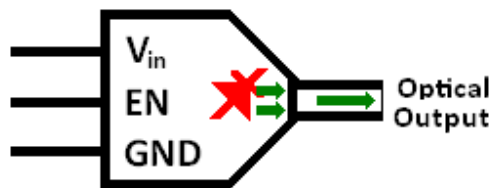


Figure 5.1: Laser driver symbol/diagram

As shown in the diagram,  $V_{in}$  stands for the input voltage, valued at 2-10V, where the input voltage and current will be regulated via Texas Instrument's LM317L. The **GND** is for the lower reference voltage, or Ground.

**EN** is the enable pin, which is necessary for power saving during the time in for cases when the controller is in sleep mode. Also, one of the main advantages of having the EN pin (base of a switching transistor) is we can poll the base output of the photodiode. As

discussed in the null test in Section 4.5.1, the base voltage varies with consecutive switching, with a 10% chance of attaining the desired value of less than 4.5V. This can be achieved by the EN pin, which can be turned on and off until the range is reached, which takes less than five seconds to configure for a centralized electronics control.

## **5.2: Tunable laser profile**

As elaborated in Section 4.3, a compact tunable laser was constructed. Combining this feature with the laser driver, we arrive at an EDFA tunable ring laser, of 20m length of EDF, with a tuning range between 1519-1589nm, which makes up to 70nm. The output power of the laser (5% from the cavity) ranges between -5 to -12dBm.

The stability of the laser was presented in two terms; its power and wavelength. A maximum change of 28pm in wavelength is observed within 1 hour, compared to the otherwise typically stable laser along the bandwidth, with stability of  $\pm 5$ pm. This imperfection will affect our interrogation only if the interrogation takes a longer time than is needed, where a single sweep along the bandwidth only takes less than 1 minute.

However, these instability values are negligible for our interrogation purposes since the maximum time for the interrogation sweep along the bandwidth takes less than 1 minute.

A maximum -2.2 dB shift at 1589.000nm change was observed, while the typical power stability shows  $\pm 0.5$ dB of fluctuation. Also, this fluctuation will not affect the interrogation for the same reasons stated above. Moreover, the null test shows a significantly flatter profile compared to an OSA, which shows the superiority of the interrogation method.

### 5.3: TBF Mounting Scheme

A method on mounting a TBF is conceived, as shown in the flow graphic in Fig. 5.2:

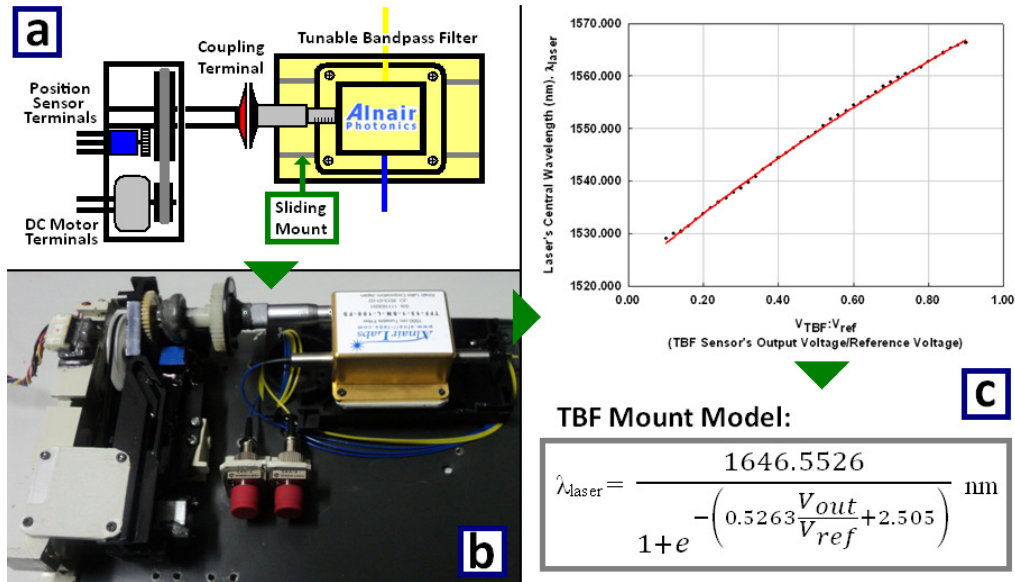


Figure 5.2: (a) TBF mount diagram, (b) constructed mount and (c) mathematical modeling of the mount

Fig. 5.2 summarizes the key issue in this work, where we establish a connection for the value of the central wavelength of the laser into voltage. The mount was modeled accordingly, where this makes the interrogation procedure possible. To our knowledge, this is a novel mounting method although not as accurate compared to conventional motorized TBFs, but this setup is much lower in cost for optoelectronics applications. The transfer function as per Eq. 4.4 can be implemented in microcontrollers (see Appendix C: Source Code)

### 5.4: FBG Interrogation

The interrogation starts with a null exercise, as demonstrated earlier. The result shows a uniform flatness when no FBG is inserted into the system. This is similar to the profile

obtained when no FBGs are connected to a direct analysis using an ASE broadband light source, an optical circulator and an OSA. A summary of the interrogation exercise is as shown in Table 5.1:

Table 5.1: Comparison of the spectral profile versus the interrogation profile

FBG no.	Reflection Spectrum from OSA (Power vs Wavelength)	Profile of Interrogation ( $V_{\text{photodiode}}$ vs $V_{\text{TBF}}$ )
FBG1		
FBG2		
FBG3		

From Table 5.1, we observe a reasonable similarity with regards to the spectral distance between both strained and unstrained conditions for all three FBGs with the interrogation exercise. This shows the consistency of the method employed for this procedure. Table 5.2 and 5.3 combines the analysis made regarding the central wavelengths of the FBG's reflection spectrum:

Table 5.2: Central wavelength of FBG's reflection spectrum analysis.

Unstrained FBGs				Strained FBGs		
FBG/ $\lambda$	$\lambda_{\text{actual}}$ (nm)	$\lambda_{\text{calculated}}$ (nm)	Error (nm)	$\lambda_{\text{actual}}$ (nm)	$\lambda_{\text{calculated}}$ (nm)	Error (nm)
FBG1	1549.816	1549.656	0.160	1550.096	1549.723	0.373
FBG2	1551.680	1551.313	0.367	1552.080	1551.784	0.296
FBG3	1555.110	1555.022	0.088	1555.812	1555.657	0.155

Table 5.3: Comparison of wavelength shift between OSA and proposed system.

FBG	$ \lambda_{\text{strained}} - \lambda_{\text{unstrained}} $ via OSA (nm)	$ \lambda_{\text{strained}} - \lambda_{\text{unstrained}} $ via proposed System (nm)	Error  (nm)
FBG1	0.280	0.067	0.213
FBG2	0.400	0.471	0.071
FBG3	0.702	0.635	0.067

Our calculations show that the range of error is between 0.09-0.4nm, which is relatively inaccurate for a general FBG profiling. However, the wavelength shift as estimated by the system bears less error, at a maximum error of 0.2nm. One of the main reasons for the error is the resolution of the voltage detection, which is a multimeter. A change of 0.001V would give us 0.009nm, or 9pm. However, increments of 0.005 are used, which increase this error by 0.045nm. Employing a higher resolution ADC will help in this matter.

Another issue faced was the tensile instability exerted on the FBGs. Tensile strain was induced by bending the FBG using a screwdriver (which remained stationary), which may be an unorthodox method of doing so. Observing the FBGs under strain using an OSA, one finds that the reflection spectrum gradually returns back to its original position. This gives rise to the inaccuracy in our calculations, when the fiber is alternated from the OSA to the

interrogator. However, the interrogation scheme in this work proves to be superior in terms of simplicity, ruggedness, and being low cost, while bearing at best a 0.09nm margin of error. The updated version of the interrogator, as of May 2013 is shown in Appendix D.

## 5.5 Chapter Summary and Future Work Suggestions

As shown by the test interrogations, we have achieved an interrogation setup which is able to scan any FBG within the C-band (1530-1560nm) with marginally small errors. The spectral shift of the FBGs can be detected quite easily from the results obtained above.

The errors of this setup may be due to the loss of sensitivity of manual tuning the TBF. The resolution of the multimeter/voltmeter is a major setback, where noise-free resolution of 0.001V is needed for a proper tuning. However, in a multimeter, this range is very susceptible to digital noise since the maximum resolution at a region of 2-5V is a maximum 0.001V. Table 5.4 summarizes the features of the interrogator versus available equipment:

Table 5.4: Comparison of features of FBG reading equipments

System Features	OSA (AQ6375)	FBGA-IRS (Bayspec)	Proposed System
Cost <sup>2</sup>	RM95-195k	≈RM20k	≈RM5k
Size	Very large & Bulky	Small	Small (20.5x14.5x7.5cm)
Weight	Very heavy	Light	Light
Light Source needed?	Yes	Yes	No
Speed/Scan rate	Moderate (1-3Hz) <sup>3</sup>	Very Fast (5kHz)	Slow (Scan Period ≥ 10 mins)
Battery operable?	No	Conditional <sup>4</sup>	Yes
Wavelength Range	1200-2400nm (1.2μm)	1530-1560nm (30nm)	1519-1589nm (70nm)
Resolution	±0.05nm	±2 pm	±2 pm <sup>5</sup>

<sup>2</sup> According to quotations from supplier

<sup>3</sup> As observed, since in OSAs real-time scanning is rarely a purpose.

<sup>4</sup> FBGA-IRS operates with an external DC power supply but it may be powered using a battery since it runs on 15V DC.

<sup>5</sup> This resolution is inherent to ADC resolution for the TBF sensing output; a 16-bit ADC garners this result.

## REFERENCES

- Alzahrani, K., Burton, D., Lilley, F., Gdeisat, M., Bezombes, F., & Qudeisat, M. (2012). Absolute distance measurement with micrometer accuracy using a Michelson interferometer and the iterative synthetic wavelength principle. *Opt. Express*, 20(5), 5658-5682.
- Antunes, P., Travanca, R., Varum, H., & André, P. (2012). Dynamic monitoring and numerical modelling of communication towers with FBG based accelerometers. *Journal of Constructional Steel Research*, 74(0), 58-62. doi: 10.1016/j.jcsr.2012.02.006
- Bellemare, A., Karbsek, M., Riviere, C., Babin, F., Gang, H., Roy, V., & Schinn, G. W. (2001). A broadly tunable erbium-doped fiber ring laser: experimentation and modeling. *Selected Topics in Quantum Electronics, IEEE Journal of*, 7(1), 22-29. doi: 10.1109/2944.924005
- Bi, L., & Li, H. (2012). *An Overview of Optical Voltage Sensor*. Paper presented at the 2012 International Conference on Computer Science and Electronics Engineering.
- Bravo, M., Pinto, A. M. R., Lopez-Amo, M., Kobelke, J., & Schuster, K. (2012). High precision micro-displacement fiber sensor through a suspended-core Sagnac interferometer. *Opt. Lett.*, 37(2), 202-204.

- Bremer, K., Lewis, E., Leen, G., Moss, B., Lochmann, S., & Mueller, I. A. R. (2012). Feedback Stabilized Interrogation Technique for EFPI/FBG Hybrid Fiber-Optic Pressure and Temperature Sensors. *Sensors Journal, IEEE*, 12(1), 133-138. doi: 10.1109/jsen.2011.2140104
- Dai, Y., Chen, X., Xia, L., Zhang, Y., & Xie, S. (2004). Sampled Bragg grating with desired response in one channel by use of a reconstruction algorithm and equivalent chirp. *Opt. Lett.*, 29(12), 1333-1335.
- Fibreoptics Inc., D. (2001). Motorized Tunable Bandpass Filter *n.a.* (pp. 45).
- Frankel, M. E., & Esman, R. D. (1995). Fiber-optic tunable microwave transversal filter. *Photonics Technology Letters, IEEE*, 7(2), 191-193. doi: 10.1109/68.345919
- Gao, L., Chen, X., Xiong, J., Liu, S., & Pu, T. (2012). Fabricating fiber Bragg gratings with two phase masks based on reconstruction-equivalent-chirp technique. *Opt. Express*, 20(3), 2240-2245.
- Heebner, J. E., Vincent, W., Schweinsberg, A., Boyd, R. W., & Jackson, D. J. (2004). Optical transmission characteristics of fiber ring resonators. *Quantum Electronics, IEEE Journal of*, 40(6), 726-730. doi: 10.1109/jqe.2004.828232
- Hill, K. O., Fujii, Y., Johnson, D. C., & Kawasaki, B. S. (1978). Photosensitivity in optical fiber waveguides: Application to reflection filter fabrication. *Applied Physics Letters*, 32(10), 647-649. doi: 10.1063/1.89881

- Ho, S. C. M., Razavi, M., Nazeri, A., & Song, G. (2012). FBG Sensor for Contact Level Monitoring and Prediction of Perforation in Cardiac Ablation. *Sensors*, *12*(1), 1002-1013.
- Holmes, C., Adikan, F. R. M., Webb, A. S., Gates, J. C., Gawith, C. B. E., Sahu, J. K., . . . Payne, D. N. (2008, 4-9 May 2008). *Evanescent field sensing in novel flat fiber*. Paper presented at the Lasers and Electro-Optics, 2008 and 2008 Conference on Quantum Electronics and Laser Science. CLEO/QELS 2008. Conference on.
- Ismail, M. A., Tamchek, N., Hassan, M. R. A., Dambul, K. D., Selvaraj, J., Rahim, N. A., . . . Adikan, F. R. M. (2011). A Fiber Bragg Grating—Bimetal Temperature Sensor for Solar Panel Inverters. *Sensors*, *11*(9), 8665-8673.
- Koo, K. P., & Kersey, A. D. (1995). Bragg grating-based laser sensors systems with interferometric interrogation and wavelength division multiplexing. *Lightwave Technology, Journal of*, *13*(7), 1243-1249. doi: 10.1109/50.400692
- Kumbhat, S., Sharma, K., Gehlot, R., Solanki, A., & Joshi, V. (2010). Surface plasmon resonance based immunosensor for serological diagnosis of dengue virus infection. *Journal of Pharmaceutical and Biomedical Analysis*, *52*(2), 255-259. doi: 10.1016/j.jpba.2010.01.001
- Labs Co., A. (n.a.). Data Sheet: APDOC-1001 (TFF-SM or TFF-PM) *Manual Tune Wavelength Selective Filter*. Alnair Labs. Corporation, Tokyo.

- Ma, G.-m., Li, C.-r., Luo, Y.-t., Mu, R.-d., & Wang, L. (2012). High sensitive and reliable fiber Bragg grating hydrogen sensor for fault detection of power transformer. *Sensors and Actuators B: Chemical*, 169(0), 195-198. doi: 10.1016/j.snb.2012.04.066
- Meltz, G., Morey, W. W., & Glenn, W. H. (1989). Formation of Bragg gratings in optical fibers by a transverse holographic method. *Opt. Lett.*, 14(15), 823-825.
- Ming Gang, X., Geiger, H., & Dakin, J. P. (1996). Modeling and performance analysis of a fiber Bragg grating interrogation system using an acousto-optic tunable filter. *Lightwave Technology, Journal of*, 14(3), 391-396. doi: 10.1109/50.485598
- Miniscalco, W. J. (1991). Erbium-doped glasses for fiber amplifiers at 1500 nm. *Lightwave Technology, Journal of*, 9(2), 234-250. doi: 10.1109/50.65882
- Passaro, V. M. N., Tsarev, A. V., & De Leonardis, F. (2012). Wavelength Interrogator for Optical Sensors Based on a Novel Thermo-Optic Tunable Filter in SOI. *Lightwave Technology, Journal of*, 30(13), 2143-2150. doi: 10.1109/jlt.2012.2192907
- Paterno, A. S., Haramoni, N., Silva, J. C. C., & Kalinowski, H. J. (2007). Highly reliable strain-tuning of an Erbium-doped fiber laser for the interrogation of multiplexed Bragg grating sensors. *Optics Communications*, 273(1), 187-192. doi: 10.1016/j.optcom.2006.12.004
- Photonics, A. (n/a). InGaAs Pin Photodiode (pp. 2).

- Prakash Dwivedi, R., & Lee, E. H. (2012). A compact plasmonic tunable filter using elasto-optic effects. *Optics and Laser Technology*, 44(7), 2130-2134.
- Shi, L., Zhu, T., Chen, F., Deng, M., & Huang, W. (2012). Tunable filter based on a pair of special long-period fiber gratings and its application in fiber ring laser. *Laser Physics*, 22(3), 575-578. doi: 10.1134/s1054660x1203019x
- Sola, I. J., Martín, J. C., & Álvarez, J. M. (2002). 980 and 1480 nm EDF characterisation by ring tunable laser dynamic study. *Optics Communications*, 203(3-6), 349-358. doi: 10.1016/s0030-4018(02)01188-4
- Song, Y. W., Havstad, S. A., Starodubov, D., Xie, Y., Willner, A. E., & Feinberg, J. (2001). 40-nm-wide tunable fiber ring laser with single-mode operation using a highly stretchable FBG. *Photonics Technology Letters, IEEE*, 13(11), 1167-1169. doi: 10.1109/68.959352
- Spirin, V. V., Shlyagin, M. G., Miridonov, S. V., Jiménez, F. J. M., & Gutiérrez, R. M. L. (1999). Fiber Bragg grating sensor for petroleum hydrocarbon leak detection. *Optics and Lasers in Engineering*, 32(5), 497-503. doi: 10.1016/s0143-8166(00)00021-x
- Sun, L., Sun, Q. Q., Ren, L., & Zhang, X. S. (2012). A new method for underground pipeline corrosion monitoring applied FBG. *Guangzi Xuebao/Acta Photonica Sinica*, 41(1), 6-10.

- Wada, A., Tanaka, S., & Takahashi, N. (2012). Optical Fiber Vibration Sensor Using FBG Fabry&#x2013;Perot Interferometer With Wavelength Scanning and Fourier Analysis. *Sensors Journal, IEEE*, 12(1), 225-229. doi: 10.1109/jsen.2011.2141984
- Wo, J., Wang, G., Cui, Y., Sun, Q., Liang, R., Shum, P. P., & Liu, D. (2012). Refractive index sensor using microfiber-based Mach-Zehnder interferometer. *Opt. Lett.*, 37(1), 67-69.
- Xu, Q., Zhang, L., & Liang, W. (2012). Acoustic detection technology for gas pipeline leakage. *Process Safety and Environmental Protection*(0). doi: 10.1016/j.psep.2012.05.012
- Yamashita, S. (2001). Widely tunable erbium-doped fiber ring laser covering both C-band and L-band. *Selected Topics in Quantum Electronics, IEEE Journal of*, 7(1), 41-43. doi: 10.1109/2944.924007
- Ye, X. W., Ni, Y. Q., Wong, K. Y., & Ko, J. M. (2012). Statistical analysis of stress spectra for fatigue life assessment of steel bridges with structural health monitoring data. *Engineering Structures*, 45(0), 166-176. doi: 10.1016/j.engstruct.2012.06.016
- Yue, L. N., Xiang, S. J., & Yang, Y. (2012). The Intelligent Bridge Health Monitoring System Based on Optical Fiber Sensing Technology. *Advanced Materials Research (Volumes 490 - 495), Mechatronics and Intelligent Materials II*, 3792-3796. doi: 10.4028/[www.scientific.net/AMR.490-495.3792](http://www.scientific.net/AMR.490-495.3792)

Zhang, L., Zhang, W., Bennion, I., Lee, B., & Jeong, Y. (2008). *Fiber Optic Sensors* (2nd ed.). 6000 Broken Sound Parkway NW, Suite 300 Boca Raton, FL 33487-2742: CRC Press (Taylor & Francis Group).

Zhang, Z., Yan, L., Pan, W., Luo, B., Wang, P., Guo, L., & Zhou, W. (2012). Sensitivity Enhancement of Strain Sensing Utilizing a Differential Pair of Fiber Bragg Gratings. *Sensors*, *12*(4), 3891-3900.

Zhu, Y., Zhang, C., & Zhao, B. (2012). Design and analysis of a novel noncollinear acousto-optic tunable filter. *Optics Communications*, *285*(9), 2332-2334.

## LIST OF PUBLICATIONS

Poh, A. H., F. R. M. Adikan, et al. (2012). A mounting method on configuring a wavelength-voltage relation of an optical tunable bandpass filter (TBF) for actuation & control. Photonics (ICP), 2012 IEEE 3rd International Conference on.

Poh, A. H., F. R. M. Adikan, et al. (2012). A Field Deployable FBG Interrogator. International Journal of Optomechatronics, 2012 (Submitted)

Patent: Poh, A. H., F. R. M. Adikan, et al. (2012). A Tunable Laser with fiber Bragg Grating Interrogation Mechanisms. Pintas IP, 2012 (Pending).

## Appendix A: An FBG's reflection response via EXFO's IQ-2600 Tunable Laser Source, and a photodiode

Table A.1: Central wavelength vs photodiode output voltage

Central Wavelength of Tunable Laser (nm)	Photodiode Output (V)
1553.50	0.3100
1553.60	0.3100
1553.70	0.3100
1553.80	0.3100
1553.90	0.3100
1554.00	0.3100
1554.10	0.3100
1554.20	0.3100
1554.30	0.3100
1554.40	0.3100
1554.50	0.3100
1554.60	0.3200
1554.70	0.3200
1554.80	0.3500
1554.90	0.3900
1554.94	0.4080
1554.97	0.4160
1555.02	0.4300
1555.05	0.4350
1555.09	0.4300
1555.12	0.4200
1555.22	0.3800
1555.30	0.3500
1555.40	0.3200
1555.50	0.3200
1555.60	0.3100
1555.70	0.3100
1555.80	0.3100
1555.90	0.3100
1556.00	0.3100
1556.10	0.3100
1556.20	0.3100
1556.30	0.3100
1556.40	0.3100
1556.50	0.3100
1556.60	0.3100
1556.70	0.3100

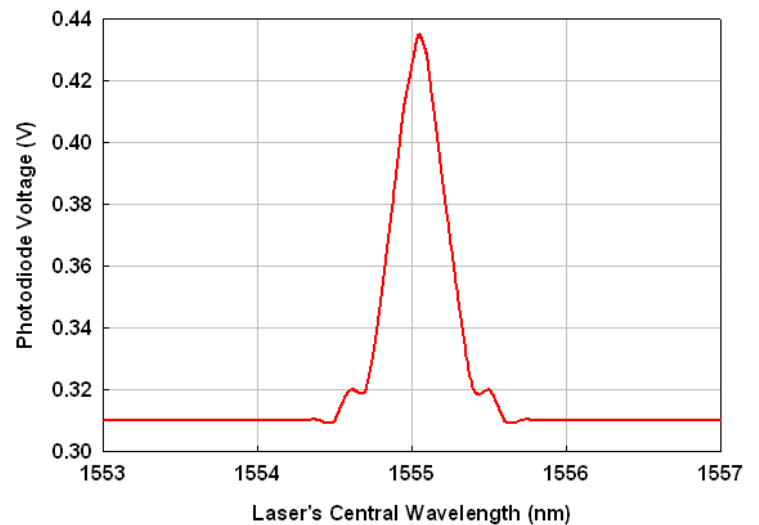


Figure A.1: Central wavelength vs photodiode output voltage

**Appendix B: TBF's positioning sensor output versus the central wavelength of the tunable laser formed, monitored using OSA**

Table B.1:  $V_{\text{sensor}}$  vs  $\lambda(\text{nm})$

$V_{\text{sensor}}$ (V)	$\lambda(\text{nm})$
0.50	1528.90
0.60	1529.70
0.70	1530.70
0.80	1531.60
0.90	1532.90
1.00	1534.00
1.10	1535.10
1.20	1536.10
1.30	1537.10
1.40	1537.90
1.50	1538.90
1.60	1539.80
1.70	1540.80
1.80	1542.00
1.90	1542.80
2.00	1544.20
2.10	1545.10
2.20	1546.10
2.30	1547.30
2.40	1548.70
2.50	1549.95
2.60	1550.80
2.70	1551.70
2.80	1552.70
2.90	1553.60
3.00	1554.15
3.10	1554.95
3.20	1555.65
3.30	1556.30
3.40	1557.60
3.50	1558.50
3.60	1559.40
3.70	1560.20
3.80	1560.25
3.90	1561.35
4.00	1561.90
4.10	1562.75
4.20	1563.60
4.30	1564.60

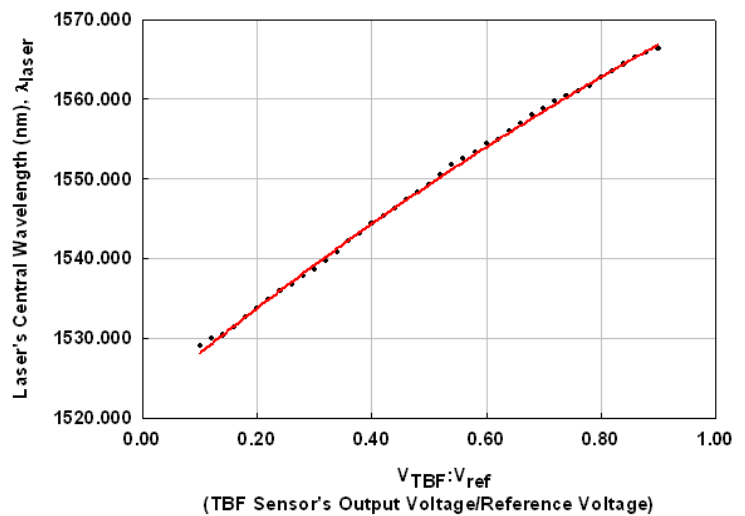


Figure B.1:  $V_{\text{sensor}}$  vs  $\lambda(\text{nm})$

## Appendix C: Source Code

This section is dedicated to the code compiled into a PIC microcontroller, a PIC18F4620. This system mainly addresses processing data from the hardware ADC and a 16-bit ADC chip (ADS1100 from Texas Instruments) via I<sup>2</sup>C interface, an alphanumeric 16x2 LCD display to continually update two parameters, namely the voltage generated from the optical output, and the central wavelength. The filter is driven via a push-pull driver (LD293). This system has two switches, both for the right and left laser sweep. The circuit for this system is shown in Appendix D. This code is written in C language via MikroC Pro v5.8.0.

---

```

extern sbit Soft_I2C_Scl_Direction;
extern sbit Soft_I2C_Scl;
extern sbit Soft_I2C_Sda;
extern sbit Soft_I2C_Sda_Direction;

sbit Soft_I2C_Scl at rb7_bit;
sbit Soft_I2C_Sda at rb6_bit;
sbit Soft_I2C_Scl_Direction at trisb7_bit;
sbit Soft_I2C_Sda_Direction at trisb6_bit;

void Soft_I2C_Init();
void Soft_I2C_Start(void);
void Soft_I2C_Stop(void);
unsigned short Soft_I2C_Read(unsigned int
ack);
unsigned short Soft_I2C_Write(unsigned
short data_);

unsigned int
a_,b_,c_,d_,e_,f_,g_,h_,i_,j_,highb,lowb,time
r=0;
unsigned long highbyte,lowbyte,x_=0;
float y_, z_=0;
void display(int j, int k);

// LCD module connections
sbit LCD_RS_Direction at TRISB2_bit;
sbit LCD_EN_Direction at TRISB0_bit;
sbit LCD_D4_Direction at TRISD3_bit;
sbit LCD_D5_Direction at TRISD2_bit;
sbit LCD_D6_Direction at TRISD1_bit;

sbit LCD_D7_Direction at TRISD0_bit;

sbit LCD_RS at RB2_bit;
sbit LCD_EN at RB0_bit;
sbit LCD_D4 at RD3_bit;
sbit LCD_D5 at RD2_bit;
sbit LCD_D6 at RD1_bit;
sbit LCD_D7 at RD0_bit;
// End LCD module connections

void interrupt (){

    if (adif_bit==1){
        adif_bit=0;
        go_bit=1;
    }
}

void display (int j, int k, int l){ // j: display
digit value
                                // k: row (1 or 2)
                                // l: position

    switch (j){
        case 0:
            Lcd_Out(k,l,"0");
            break;
        case 1:
            Lcd_Out(k,l,"1");
            break;
        case 2:
            Lcd_Out(k,l,"2");
            break;
    }
}

```

```

case 3:
    Lcd_Out(k,l,"3");
    break;
case 4:
    Lcd_Out(k,l,"4");
    break;
case 5:
    Lcd_Out(k,l,"5");
    break;
case 6:
    Lcd_Out(k,l,"6");
    break;
case 7:
    Lcd_Out(k,l,"7");
    break;
case 8:
    Lcd_Out(k,l,"8");
    break;
case 9:
    Lcd_Out(k,l,"9");
    break;
}
}

const char character1[] =
{8,20,4,6,10,18,17,0}; // Display lambda
const char character2[] = {0,0,0,0,6,8,8,6};
// Display small C
const char character3[] =
{0,0,0,0,21,21,21,10}; // Display small W
const char character4[] = {0,0,0,0,14,9,14,8};
// Display small P
const char character5[] =
{0,0,0,0,2,14,18,14}; // Display small D
const char character6[] =
{31,4,4,4,0,0,0,0}; // Display
superscript T
const char character7[] =
{17,27,21,17,0,0,0,0}; // Display
superscript M

void lambda(char pos_row, char pos_char) {
    char i;
    Lcd_Cmd(64);
    for (i = 0; i<=7; i++)
        Lcd_Chrcp(character1[i]);
    Lcd_Cmd(_LCD_RETURN_HOME);
    Lcd_Chrcp(pos_row, pos_char, 0);
}

void small_c(char pos_row, char pos_char) {
    char i;
    Lcd_Cmd(72);
    for (i = 0; i<=7; i++)
        Lcd_Chrcp(character2[i]);
    Lcd_Cmd(_LCD_RETURN_HOME);
    Lcd_Chrcp(pos_row, pos_char, 1);
}

void small_w(char pos_row, char pos_char) {
    char i;
    Lcd_Cmd(80);
    for (i = 0; i<=7; i++)
        Lcd_Chrcp(character3[i]);
    Lcd_Cmd(_LCD_RETURN_HOME);
    Lcd_Chrcp(pos_row, pos_char, 2);
}

void small_p(char pos_row, char pos_char) {
    char i;
    Lcd_Cmd(88);
    for (i = 0; i<=7; i++)
        Lcd_Chrcp(character4[i]);
    Lcd_Cmd(_LCD_RETURN_HOME);
    Lcd_Chrcp(pos_row, pos_char, 3);
}

void small_d(char pos_row, char pos_char) {
    char i;
    Lcd_Cmd(96);
    for (i = 0; i<=7; i++)
        Lcd_Chrcp(character5[i]);
    Lcd_Cmd(_LCD_RETURN_HOME);
    Lcd_Chrcp(pos_row, pos_char, 4);
}

void small_t(char pos_row, char pos_char) {
    char i;
    Lcd_Cmd(104);
    for (i = 0; i<=10; i++)
        Lcd_Chrcp(character6[i]);
    Lcd_Cmd(_LCD_RETURN_HOME);
    Lcd_Chrcp(pos_row, pos_char, 5);
}

void small_m(char pos_row, char pos_char) {
    char i;
    Lcd_Cmd(112);
    for (i = 0; i<=10; i++)
        Lcd_Chrcp(character7[i]);
    Lcd_Cmd(_LCD_RETURN_HOME);
    Lcd_Chrcp(pos_row, pos_char, 6);
}

void main(){
    ////////////////////////////////////////////////////
    // Motor Control Pins ///
    ////////////////////////////////////////////////////
    trisb5_bit=1; // SW1 //
    trisc0_bit=1; // SW2 //
}

```

```

//
trisa3_bit=0; // IN1 //
trisa4_bit=0; // IN2 //
rb3_bit=rb4_bit=0; //
////////////////////
/// Laser Control ///
////////////////////
trisa=0x01; //
porta=0; //
////////////////////
trisd=0;
portd=0;
portc=0;

trisa1_bit=0; // Software GND for 16x2 LCD
trisa1_bit=0; // "

Lcd_Init(); // Initialize LCD

Lcd_Cmd(_LCD_CLEAR); // Clear
display

Lcd_Cmd(_LCD_CURSOR_OFF); //
Cursor off

Lcd_Out(1,2,"Initializing...");
Delay_ms(1000);
Lcd_Cmd(_LCD_CLEAR);
Lcd_Out(1,4,"Welcome to");
Lcd_Out(2,3,"Photonics@UM");
Delay_ms(1000);
Lcd_Cmd(_LCD_CLEAR);
Lcd_Out(1,2,"**Presenting**");
Delay_ms(1000);
Lcd_Cmd(_LCD_CLEAR);
Lcd_Out(1,5,"Portable");
Lcd_Out(2,1,"FBG Interrogator");
Delay_ms(1000);
Lcd_Cmd(_LCD_CLEAR);
Lcd_Out(1,3,"BraggScann");
small_t(1,13);
small_m(1,14);
Delay_ms(1000);
Lcd_Cmd(_LCD_CLEAR);

////////////////////Hardware ADC
Initialization////////////////////
adie_bit=1; //
gie_bit=1; //
peie_bit=1; //
ipen_bit=1; //
//

adcon0=0x01; //ENABLE A/D

adcon1=0x8E; //AN0= INPUT
adcon2=0xAE; //left justified, Fosc/64, 12
TAD //
go_bit=1; //
////////////////////

////////////////////
Soft_I2C_Init(); //
Soft_I2C_Start(); //
Soft_I2C_Write(0x90); // I2C Definitions
Soft_I2C_Write(0x8c); //
Soft_I2C_Stop(); //
////////////////////
Lcd_Cmd(_LCD_CLEAR);

////////////////////
Lcd_Out(1,1,"V"); // Vpd= (takes Addr 1-4)
//
small_p(1,2); // //
small_d(1,3); // //
Lcd_Out(1,4,"="); //
Lcd_Out(1,7,"."); // a "." (decimal point,
Addr 6)
Lcd_Out(1,12,"V"); // Display V (Addr
10) dBm
lambda(2,1);
small_c(2,2);
small_w(2,3);
Lcd_Out(2,4,"=");
Lcd_Out(2,9,"."); // a "." (decimal
point, Addr 6)
Lcd_Out(2,13,"nm"); // Display V (Addr 12)

while(1){

////////////////////
//// Start displaying for Photodiode
Voltage////////////////////

////////////////////

highb = (unsigned int) adresh;
lowb = (unsigned int) adresl;

x_ = highb*256 + lowb;
x_ = x_*5000/1024; // In terms of volts

a_ = x_/1000;
b_ = (x_-a_*1000)/100;
c_ = (x_-a_*1000-b_*100)/10;
d_ = x_-a_*1000-b_*100-c_*10;

```

```

//////////Start Displaying the Analog
Value////////////////////////////////////

//Lcd_Out(1,1,"P"); // Vpd= (takes
Addr 1-4)
//small_p(1,2); //
//small_d(1,3); //
//Lcd_Out(1,4,"=-"); //
display(a_,1,6); // first digit (Addr
5)
//Lcd_Out(1,7,"."); // a "." (decimal
point, Addr 6)
display(b_,1,8); // 2nd digit (Addr
7)
display(c_,1,9); // 3rd digit (Addr 8)
display(d_,1,10); // 4th digit (Addr
9)
//Lcd_Out(1,12,"dBm"); // Display V
(Addr 10) dBm

////////////////////////////////////
//////
////////// Start with ADS1100 reading
////////////////////////////////////

Soft_I2C_Start();
Soft_I2C_Write(0x91);
highbyte=Soft_I2C_Read(1);
lowbyte=Soft_I2C_Read(0);
Soft_I2C_Stop();

x_=(highbyte<<8)+lowbyte;

y_=(1646.5526/(1+exp(-
((x_/32767.0)+4.7596)/1.8999)))+1.9; //TBF
model incorporation
x_=y_*1000;

//////////Start Displaying the absolute decimal
Value//////////

a_=x_/1000000; //1st digit
b_=(x_-a_*1000000)/100000; //2nd digit
c_=(x_-a_*1000000-b_*100000)/10000;
//3rd digit
d_=(x_-a_*1000000-b_*100000-
c_*10000)/1000; //4th digit
e_=(x_-a_*1000000-b_*100000-
c_*10000-d_*1000)/100;
f_=(x_-a_*1000000-b_*100000-
c_*10000-d_*1000-e_*100)/10;

g_=x_-a_*1000000-b_*100000-
c_*10000-d_*1000-e_*100-f_*10;

//lambda(2,1);
//small_c(2,2);
//small_w(2,3);
//Lcd_Out(2,4,"=");
display(a_,2,5); // 1st digit (Addr 4)
display(b_,2,6); // 2nd digit (Addr 5)
display(c_,2,7); // 3rd digit (Addr 6)
display(d_,2,8); // 4th digit (Addr 7)

//Lcd_Out(2,9,"."); // a "." (decimal
point, Addr 6)

display(e_,2,10); // 5th digit (Addr 9)
display(f_,2,11); // 6th digit (Addr 10)
display(g_,2,12); // 7th digit (Addr 11)

//Lcd_Out(2,13,"nm"); // Display V
(Addr 12) Volts

////////////////////////////////////
////////// Function end
////////////////////////////////////

////////////////////////////////////
//////Tunable Bandpass Filter Motor Control
//////
////////////////////////////////////

if (rc0_bit==1){
rb3_bit=0;
rb4_bit=1;
}

else if (rb5_bit==1){
rb4_bit=0;
rb3_bit=1;
}

else rb3_bit=rb4_bit=0;
}

////////////////////////////////////
//////////Code ends////////////////////////////////////

```

### Appendix D: Current advancements in project

This section is dedicated to the further developments as of May 2013. The current prototype has reached its technical maturity, providing a broader view on the aspects of the interrogator which may be improved in future.

The finalized interrogator circuitry is as shown in Fig. D1.

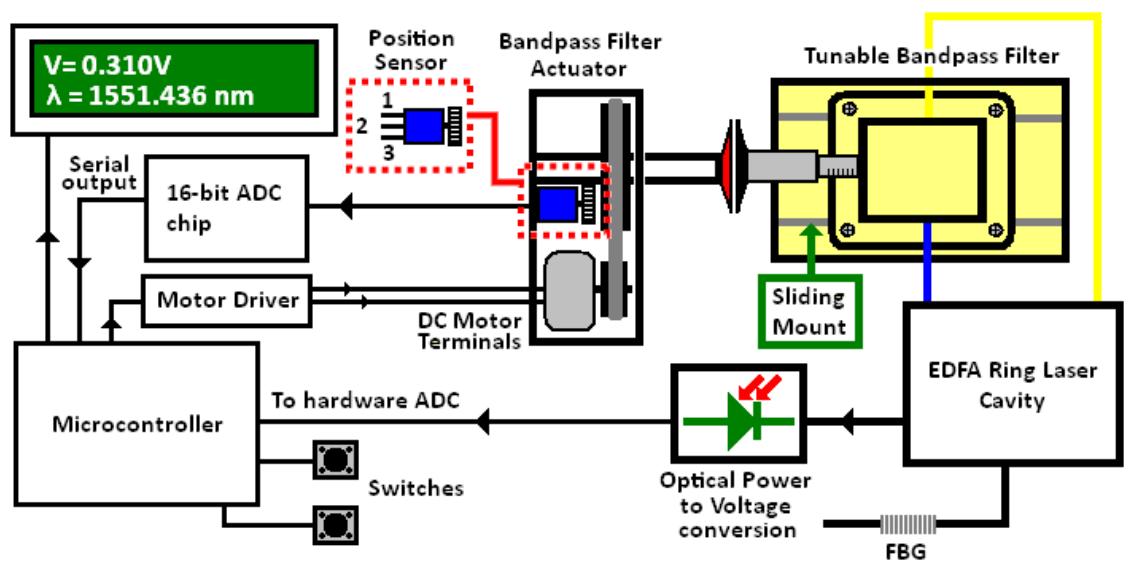


Figure D1: Complete overview of the FBG interrogator circuitry

Current developments are under way on understanding the tuning mechanism of this system, which includes the construction of another Erbium-doped fiber laser with an external cavity. The system is represented by Fig. D2.

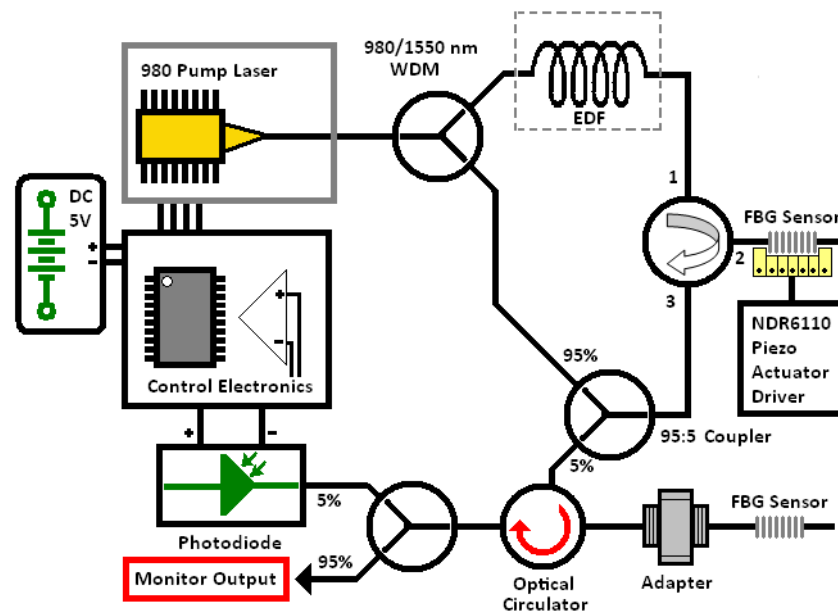


Figure D2: An EDFL with an external cavity setup

Fig. D2 shows that the filter mechanism has changed to a fully fiber-based setup, which paves way for more compact interrogation devices. Piezo stretchers are used to tune an FBG which is mounted using UV glue. Currently, the development is still at an early stage. Fig. D3 shows the setup which was constructed.

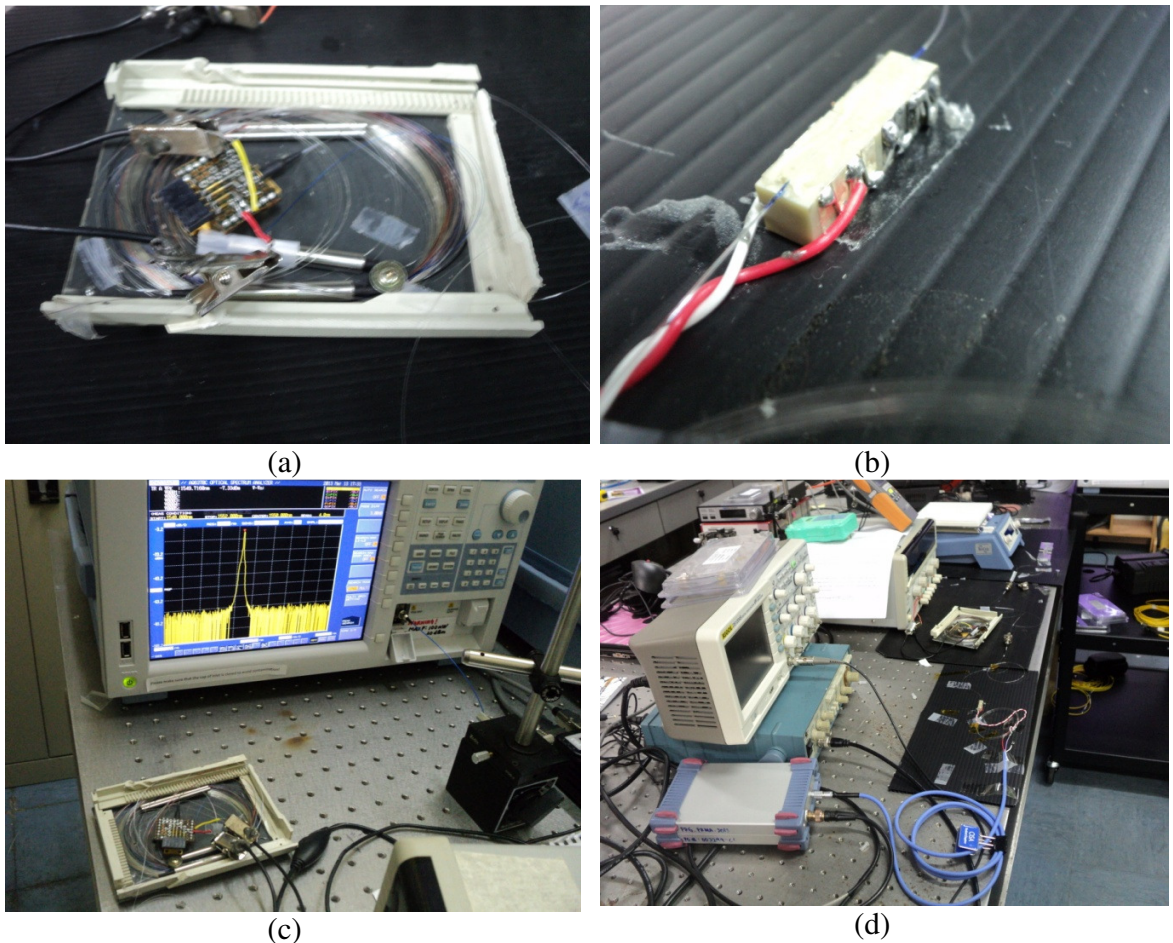


Figure D3 (a) A compiled optical circuitry for the EDFL without the tuning filter; (b) FBG mounted on stacked piezo actuators; (c) laser formation via the external cavity of the EDFL; (d) the whole setup for the current research

The setup for the piezo driver utilizes a signal generator to drive the piezo actuators from Noliac Inc. The system utilizes a signal generator to drive the stacked piezo actuators, via a piezo driver NDR6110, also from Noliac Inc. The external cavity which consists of an FBG, which is mounted on 10 stacked piezos, generated a maximum 0.1nm shift. Further advancements can be made with adding more stacked piezo actuators, and dedicating more research on building a specified piezo driver circuitry, which will make the system much more compact.